ISSN number 0971 - 9709

IGU
Promoting Earth System Sciences

The Journal of Indian Geophysical Union

AN OPEN ACCESS BIMONTHLY JOURNAL OF IGU

VOLUME 29, ISSUE 2, MARCH 2025

EDITORIAL OFFICE

Indian Geophysical Union, NGRI Campus, Uppal Road, Hyderabad- 500 007

Telephone: 91-4027012739, 27012332; Telefax:+91-04-27171564

Email: jigu1963@gmail.com, website: http://iguonline.in/journal/

The Journal with six issues in a year publishes articles covering

Solid Earth Geosciences; Marine Geosciences; and Atmospheric, Space and Planetary Sciences.

The Journal is Financially supported by MoES, Govt. of India.

Annual Subscription

Individual Rs -1000/- per issue and Institutional Rs- 5000/- for six issues

Payments should be sent by DD drawn in favour of "The Treasurer, Indian Geophysical Union", payable at Hyderabad,

Money Transfer/NEFT/RTGS (Inter-Bank Transfer), Treasurer, Indian Geophysical Union, State Bank of India, Habsiguda Branch,

Habsiguda, Uppal Road, Hyderabad- 500 007

A/C: 52191021424, IFSC Code: SBIN0020087, MICR Code: 500002318, SWIFT Code: SBININBBHO9.

For correspondence, please contact, Hon. Secretary, Indian Geophysical Union, NGRI Campus, Uppal Road,

Hyderabad - 500 007, India; Email: igu123@gmail.com; Ph: 040 27012332

ISSN: 0257-7968 (Clarivate Analytics)
ISSN: 0971-9709 (NISCAIR)
Approved as bimonthly ESCI journal by Clarivate Analytics
Cited in Indian Citation Index (ICI), New Delhi
Evaluated by NISCAIR, New Delhi
SCI & UGC Approved Journal

CONTENTS

Research Articles

J. Ind. Geophys. Union, 29(2) (2025), 68-80
https://doi.org/10.71122/JIGU.29(2)2025.008

Geochemical constraints on the origin of ophiolitic chert from Naga Hills Ophiolite, Northeast India

Anisha Verencar[1,2], Abhishek Saha[1*], M. Ram Mohan[3]
[1]CSIR-National Institute of Oceanography, Dona Paula, Goa-403 004, India
[2]School of Earth, Ocean and Atmospheric Sciences, Goa University, Taleigão Plateau, Goa-403 206, India
[3]CSIR-National Geophysical Research Institute, Uppal Road, Hyderabad-500 007, India
*Corresponding author: asaha.nio2015@gmail.com

ABSTRACT

The uppermost part of the Naga Hills ophiolite (NHO) sequence representing vestiges of the Neo-Tethyan ocean in the Indo-Myanmar ranges, consists of Late Jurassic to Late Cretaceous cherts that carapace the ophiolitic volcanics. This contribution presents petrographic and whole rock geochemical studies to comprehend their origin and paleo-depositional environment. The occurrences of abundant radiolarian microfossils in the studied cherts are observed. Geochemical signatures of these cherts indicate that they are generated at rifted arc basin by pronounced hydrothermal activity along with terrigenous material influx from active continental margin. Redox sensitive trace element proxies U/Th (0.12-0.74), Ni/Co (0.10-0.67) and V/(V+Ni) (0.22-0.47) record oxic paleo-redox conditions of formation. The cherts of NHO are envisaged to have formed in a transitional tectonic environment associated with magmatism and subsequent sedimentation in a rifted arc basin proximal to an active continental margin.

Keywords: Ophiolite, Radiolarian chert, Depositional environment, Paleo-redox conditions, Tethys Ocean.

INTRODUCTION

The north eastern extension of the Yarlung-Tsangpo suture zone, located along the Indo-Myanmar ranges (IMR), hosts a collage of dismembered ophiolitic suite and mélange of Neo-Tethyan origin. This ophiolitic suite comprising plutonic to volcanic lithologies of ultramafic-mafic composition, is overlain by deep sea silicious pelagic sediments with radiolarian fossils. The Naga Hills ophiolite (NHO), the northern most extension of the IMR, hosts a dismembered suite of ophiolitic rocks. Many workers have discussed different tectonic settings for the formation of NHO from mineral chemical and whole rock studies of one or more litho-units belonging to this ophiolitic suite and associated metamorphic complex. Early works suggest basalts to be originated in a back arc basin environment, while some suggest within plate tectonic regime for their origin (Sengupta et al., 1989; Rao et al., 2010). Recent studies suggest dual affinities for the NHO i.e. mid oceanic ridge and arc tectonic setting (Dey et al., 2018; Hussain and Dey, 2022). Singh et al. (2016) and Khogenkumar et al. (2021) suggest both non-subduction (viz. OIB and MORB) and subduction origin. Studies based on the metamorphic complex associated with the NHO, reveal that the basalts were metamorphosed to blueschist and eclogite facies in a subduction zone setting (Chatterjee and Ghose, 2010; Ao and Bhowmik, 2014; Bhowmik et. al, 2022; Bhowmik and Pradhan, 2024). Our previous works based on the spinel chemistry and whole rock Os isotopic studies for mafic-ultramafic plutonic assemblage of NHO, indicates the evolution of the NHO to a supra-subduction zone tectonic setting (Verencar et al., 2021; 2022; 2024a).

The chert beds are largely intercalated with the mafic volcanics of the NHO and these have been least studied as compared to their igneous counterparts in the ophiolitic sequence. The geochemical studies of these siliceous rocks containing radiolarians and sponge spicules, have become an important tool to infer the paleogeography and the tectonic setting of their depositional environment. Certain major oxides like TiO_2, Al_2O_3, Fe_2O_3 and MnO in addition to trace and rare earth elements, have been effectively used to evaluate the process involved in the genesis of cherts (Kato et al., 2002; Huang et al., 2013; Garbán et al., 2017). A few studies including paleontological studies by Agrawal (1985) and Baxter et al. (2011); and geochemical studies by Thong et al. (2022) have been carried out earlier on the cherts from NHO. Here, in this study, we evaluate the geochemical signatures of the cherts associated with ophiolitic volcanic rocks and further discuss their depositional environment in terms of paleo-redox conditions and constrain their tectonic affiliation based on the geochemical characteristics.

REGIONAL GEOLOGY

The Late Mesozoic to Early Cenozoic evolution of the Tethyan Ophiolite Belt is linked to the closure of the Tethyan Ocean and collision of the Indian and Eurasian Plates. These two tectonic events were marked by plate convergence, subduction of oceanic lithosphere, ophiolite obduction, high pressure-low temperature metamorphism and collision-accretion activities that altogether gave rise to Alpine-Himalayan and Burmese-Indonesian arc systems (Robertson, 2002; Acharyya, 2007; Aldanmaz et al., 2008; Saha et al., 2018;2019). In India, Cretaceous ophiolites have been recorded as parts of the Alpine-Himalayan and Indo-Burman orogenic belts. The NHO belt in the IMR represents a segment of Tethyan oceanic crust and upper mantle that was involved in an eastward convergence and collision of the Indian Plate with the Eurasian Plate at the Myanmar continental margin during the Late Cretaceous-Eocene (Ghose and Agarwal, 1989) (Figure 1a

inset). The Naga Hills with in the Ziphu Formation is a ~200 km long, ~5-10 km wide, westerly convex linear belt striking NE-SW (Table 1). It comprises of four major tectono-stratigraphic units, namely the Naga Metamorphic complex, the NHO suite, the Inner Fold belt and the belt of Schuppen (Ghose et al., 1987) (Table 1, Figure 1a). The Naga metamorphic complex, which is thrusted over the Upper Cretaceous–Eocene turbidite and NHO, marks the easternmost part of the belt. It is composed of the Saramati, Nimi, and Naga metamorphic. The Naga Metamorphic complex is made up of sheared granite, phyllite, limestone, marble, quartzo-feldspathic schist, and gneiss with minor serpentine (Table 1). The ophiolite belt of the Naga Hills, lies to the east of the Saramati Formation. It is composed of carbonaceous phyllites, quartz mica schist, and schistose quartzite. The clastic nature of the rocks, the graded bedding, and the cut-and-fill structures point to its sedimentary nature. The Naga ophiolitic complex strikes NNE-SSW for ~90 km and is tectonically sandwiched between the flyshoidal sediments of the Disang Formation to its western margin (Table 1) and overridden by the Nimi Formation of the Naga Metamorphic complex at its eastern margin (Kacker and Roy, 1980; Ghose et al., 2014) (Figure 1a). The Disang Formation consists of a folded sequence of slate, graphitic slate, phyllite, siltstone and fine-grained sandstone (Agrawal and Ghose 1986; Vidyadharan et al. 1989). The Nimi Formation, covering 18 × 12 km^2 area, is exposed at the eastern fringe of Nagaland. Non-crystalline limestone, quartzite, phyllite, carbonaceous phyllite, quartz sericite schist, and schistose granite are the main litho units of the Nimi Formation (Table 1).

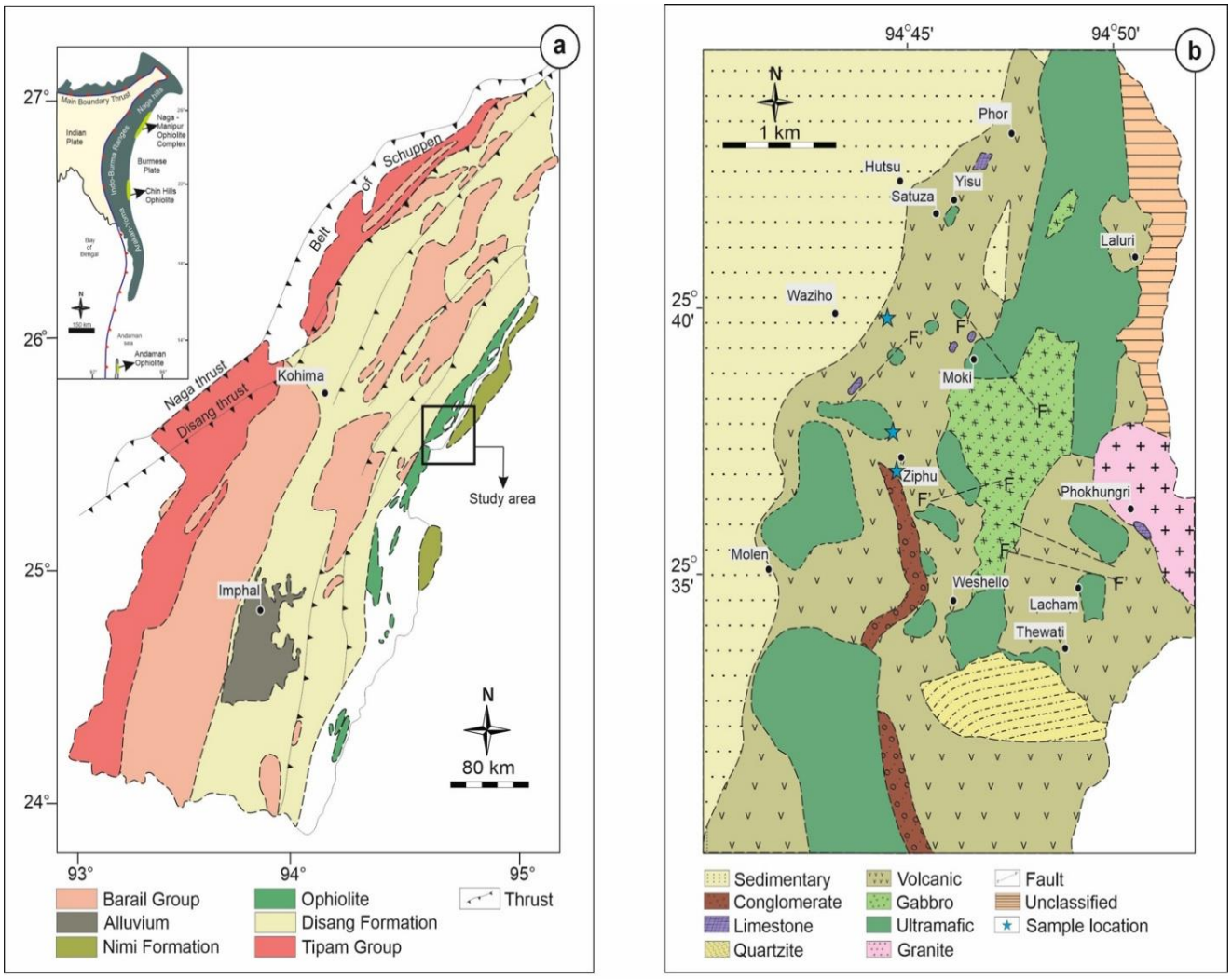

Figure 1. **(a)** Simplified geological and tectonic map of Nagaland and Manipur, India (modified after Geological Survey of India and Ningthoujam et al., 2012) inset: Simplified tectonic map of eastern margin of India depicting Naga-Manipur, Chin Hills and Andaman Ophiolitic complexes. **(b)** Geological map of Nagaland ophiolite with sample locations marked by star (modified after Agrawal and Ghose, 1986).

Table 1. Stratigraphy of Naga Hills, India (Modified after Mathur and Evans, 1964; DGM, 1978; Ghose et al., 2010, 2014)

Age	Group	Formation with lithology	
Oligocene	Barail	Jopi / Phokphur Formation Tuffaceous shale, sandstone, greywacke, gritand conglomerate. Minor limestone and carbonaceous matter	
Upper Cretaceous-Eocene	Disang	Upper	Flysch: Shale passing into slate alternating with sandstone. Presence of mega cross-bed, load cast, slumping structure and olistoliths. Evaporites.
		Lower	Flysch: Dominantly shale passing intoslate and phyllite (turbidite)
Middle Jurassic to Cretaceous	Ophiolite complex	Ziphu Formation Marine sediments (shale, phyllite, greywacke, iron-rich sediments, chert and limestone with radiolaria and coccoliths),volcanics (basalt, spilite,volcaniclastics), metabasics greenschist, glaucophane schist/glaucophane-bearing metachert, eclogite),layered cumulate sequence (peridotite, pyroxenite, gabbroids, plagiogranite), and peridotite tectonite and serpentinite associated with deposits of podiform chromite and nickeliferous magnetite, minor Cu-Mo sulphides associated with late felsic intrusions and some dolerite dykes	
		----Fault Thrust----	
Mesozoic (?)	Naga Metamorphic complex	Nimi Formation Weakly metamorphosed limestone, phyllite, quartzite and quartz-sericite schist	
		Naga Metamorphics Mica schist, granitoid gneiss and feldspathic metagreywacke with tectonic slices of ophiolite	

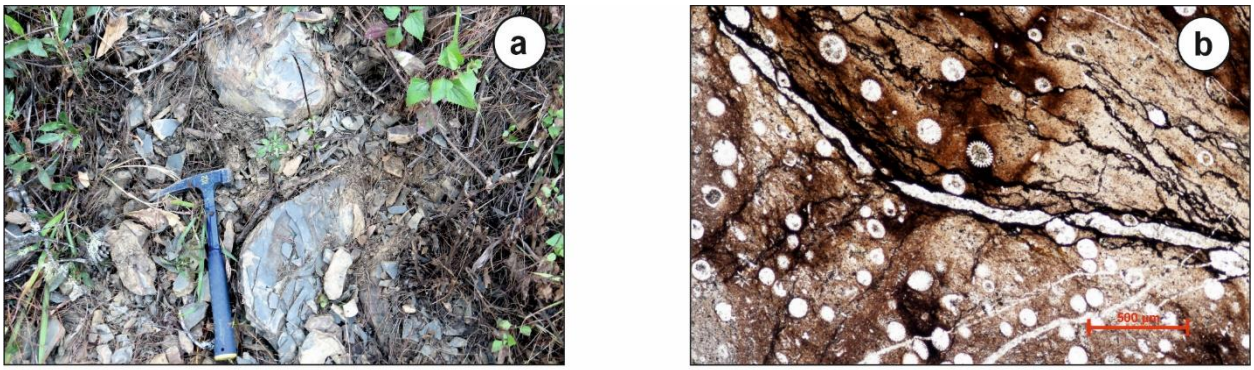

Figure 2. **(a)** Field photograph of an outcrop showing the occurrence of pelagic sediments. **(b)** Photomicrographs showing the presences of radiolarian microfossils in cherts from NHO.

FIELD GEOLOGICAL STUDIES

The NHO represents a thrusted assemblage dominated by mantle and crustal ultramafic-mafic lithologies (peridotites, dunites, pyroxenites, gabbros, olivine gabbros, norites, basalts) with minor felsic variants (plagiogranites) and pelagic sediments. The pelagic sediments include pelitic, calcareous and iron-rich sediments, and cherts. The pelitic sediments are represented by variegated shale, slate, phyllite and occasionally metamorphosed to schist. The sedimentary rocks include greywacke, arkose, subarkose and quartzite. The silica-rich cryptocrystalline cherts are extensively preserved among the marine sediments because of their resistance to weathering. They show a variety of colours including light grey, bluish grey, light green, dull to bright red and brown. They occur as thin beds and lenses interlayered with mafic volcanics.

In this study, fossiliferous red cherts occurring as beds and lenses intercalated with basalts were collected from in and around Waziho and Zipu area (Figure 1b and 2a). Previous study reported the presence of microfossils in cherts interlayered from the same areas. These include coccoliths, viz., *Zygolithus penticulus* and *Ahmullerella octoradiata*, and radiolarians, viz., *Cenozphaera* sp., *Spongodiscus* sp., etc., belonging to the Maastrichtian age (Agrawal, 1985); while radiolarian cherts from the northern sector of the NHO yielded a Late Jurassic age (Baxter et al., 2011) indicating sedimentation in the early Neotethys.

ANALYTICAL TECHNIQUES

A few selected samples from the study area were subjected to X-Ray diffraction analyses through XRD instrument Model: AXS D8 Advances (Make: Bruker Ltd Germany) at the CFC

(Common facility center)-SAIF (Sophisticated analytical instrumentation facility) Center; Shivaji University, Maharashtra. The slides were then analyzed in an X-ray diffractometer using Cu-Ka radiation source, acceleration voltage of 40 kV and tube current of 20 mA. The 2θ ranged from 5°–70°. The X-ray diffraction of the mineral were identified through respective D spacing values and intensity. The database used for mineral identification is webmineral.com.

Further, the seventeen samples were powdered a using tungsten carbide disc mill pulverizer at CSIR-National Institute of Oceanography, Goa. The powders were then analyzed for its major, trace and rare earth element concentrations along with geochemical reference materials for quality control. The concentration of major oxides was determined using X-ray fluorescence spectroscopy (XRF; PAN analytical™ Axios m AX4, microprocessor controlled, sequential XRF at CSIR-National Geophysical Research Institute, Hyderabad. In order to prepare the samples, ~ 2 gm of powdered samples were sprinkled onto a collapsible aluminum cup having a diameter of 4 cm initially filled with boric acid. Subsequently, these samples were compressed by applying a pressure of 25 tons using a hydraulic press (Hydraulic Press, Herzog, Germany). The analytical protocol used to carry out the procedures of pellet preparation was adopted from Krishna et al. (2007). Certified reference materials (CRMs) JA-1 (Japanese andesite, GSJ, Japan) and BHVO-1 (Hawaiian basalt, USGS, USA) were used as unknown samples to check the precision and reproducibility which were better than 5% RSD for all the major elements. The Loss on Ignition (LOI) was measured by taking 2 gm of sample in a quartz crucible and heating it in a muffle furnace upto ~900° C for 1 hour. The samples were then placed in a desiccator containing silica crystal. The reduction in weight measured after ignition was considered to be the loss of volatile content from the samples.

Trace elements, including rare earth elements (REE), were analyzed using a high-resolution inductively coupled mass spectrometer (HR-ICPMS). The preparation of the samples involved closed acid digestion of accurately measured 50 mg of each sample contained in Savillex® vials. This sample was treated by addition of a 7 mL mixture of supra pure HF and HNO_3 acids in 2:5 ratio into the Savillex® vials. The vials were placed on a hotplate and were heated for 72 hours at 110°C. After 72 hours, the caps were opened and the mixture was dried down and further treated with 1 mL of 2% HNO_3 until clear solution was obtained. The clear solution was once more evaporated and finally was diluted using 2% HNO_3 to prepare 50 mL stock solution for each sample along with procedural acid blank. The stock solution was further diluted 20,000 times for analyses in high resolution inductively coupled mass spectrometer (HR-ICP-MS) (Nu Instruments™ Attom, UK) at CSIR-National Institute of Oceanography, Goa. ^{103}Rh was used as an internal standard. CRMs namely, JA-1 and JB-2 (Geological Survey of Japan, Japan) were used as unknown quality standards to assess the accuracy and precision of the obtained data. For most of the elements, the accuracy and precision of the obtained data were within 10% RSD . (Please see Appendix 1)

RESULTS

Petrography and mineralogy

Seventeen samples of cherts were collected in the field. Representative samples were polished to prepare thin sections, which were studied under reflected and transmitted light using Nikon eclipse LV100 POL optical microscope at CSIR-National Institute of Oceanography (NIO), Goa, India. Petrographic studies of the cherts from NHO show the presence of dominantly quartz, with recrystallized secondary quartz veins along with minor amount of carbonate minerals. Uneven spongy (or honeycombed) interior fabrics are frequently seen in well-preserved silica mounds, with localized interconnecting channels and veins. There were several vesicles or cavities inside the mounds, but they were primarily blocked by radiating micro-quartz and fibrous recrystallized silica. Abundant microfossils of radiolarian tests are preserved within the chert (Figure 2b). X-Ray diffraction (XRD) study confirm the presence of silica as major constituent within the chert. XRD studies for most of the samples reveal prominent peaks of quartz (Figure. 3).

Whole rock geochemistry

The bulk chemical composition of NHO cherts is dominantly characterized by high SiO_2 content from 71.17 to 79.32 wt. %, moderate $Fe_2O_3^{(t)}$ and CaO ranging from 4.47 to 5.98 wt. % and 6.9 to 7.14 wt. % respectively; restricted Al_2O_3 and MgO concentrations ranging from 2.47 to 4.33 wt. and 2.25 to 2.72 wt.% respectively. The total alkali content ranges from 2.08-3.43 wt. %, MnO contents range from 0.30 to 0.90 wt. % and TiO_2 concentrations ranges from 0.12 to 0.27 wt. %. The Loss on Ignition (LOI) ranges from 1.19 to 2.85 wt. %. The major oxide analyses are provided in Table 2.

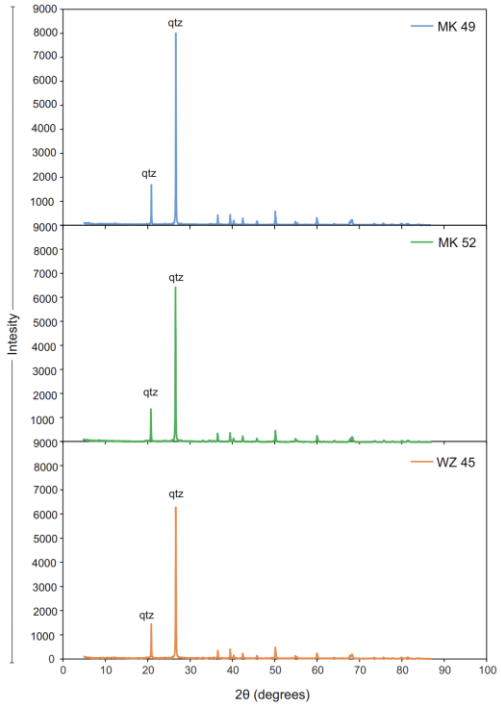

Figure 3. X-ray diffraction (XRD) patterns for the studied chert samples.

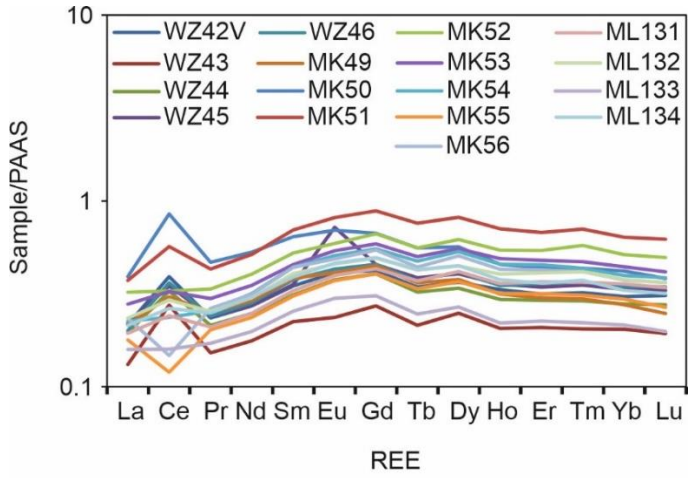

Figure 4. PAAS normalized REE patterns for the collected chert samples from NHO. Normalizing factors are from Taylor and McLennan (1985)

The studied cherts are marked by a wide variation and relatively higher concentration of transition metals like Co and Ni with Co ranging from 76.80 to 169.80 ppm (avg. 120.62 ppm; except ML134 Co: 1.25); and Ni spanning from 14.55 to 104.58 ppm (avg. 31.37ppm) as compared to Upper crust (UCC; Co: 10 ppm, Ni: 20 ppm; Taylor and McLennan, 1995) (Table 2). The average Cr concentration (15.61 ppm) is however lower as compared to UCC composition (35 ppm; Taylor and McLennan, 1995). The studied chert samples from NHO have ΣREE (32.82-117.72 ppm), lower than both the NASC (North American Shale Composite:172 ppm, and PAAS (Post Archean Australian shale:183 ppm, Taylor and Mclenan, 1985) (Table 2). The PAAS normalized REE profile depicts a convex upward pattern (Figure 4). This observation is further substantiated in the PAAS normalized REE ratios of $(La/Sm)_N$ ranging from 0.51 to 0.63 (avg.0.58), $(Gd/Yb)_N$ ranging from 1.21 to 1.62 (avg.1.40) and $(La/Yb)_N$ ranging from 0.54 to 0.93 (avg. 0.66) (Table 2). The PAAS normalized REE patterns also display a positive anomaly for Ce and negative anomalies for Eu and Tb (Figure 4). The Ce/Ce* ranges from 0.59 to 1.98 (avg. 1.34) and Eu/Eu* ranges from 0.33 to 0.80 (avg. 0.50) for the studied chert samples from NHO (Table 2)

Table 2. Major oxides and trace elements of chert samples collected from NHO

Sample ID	WZ42V	WZ43	WZ44	WZ45	WZ-46	MK49	MK50	MK51	MK52
(wt.%)									
SiO_2	77.91	76.67	75.92	76.83	76.57	76.54	75.56	71.17	75.97
Al_2O_3	2.62	3.96	3.84	2.76	2.80	2.82	3.21	4.33	2.89
$Fe_2O_3^{(t)}$	4.87	4.64	4.77	4.87	4.89	4.86	5.20	5.98	5.16
MnO	0.29	0.31	0.26	0.30	0.21	0.62	0.90	0.56	0.36
MgO	2.33	2.37	2.46	2.39	2.37	2.43	2.61	2.72	2.38
CaO	7.08	6.92	6.99	7.08	7.07	6.96	6.90	7.00	7.07
Na_2O	1.78	1.66	1.77	1.82	1.87	1.55	1.41	1.74	1.78
K_2O	0.86	0.60	0.87	0.89	1.07	0.79	0.79	1.68	1.17
TiO_2	0.16	0.13	0.16	0.17	0.17	0.14	0.15	0.27	0.18
P_2O_5	0.01	0.02	0.01	0.02	0.02	0.01	0.05	0.02	0.01
LOI	1.49	1.37	1.51	1.69	1.55	1.61	2.21	2.85	1.66
Sum	99.4	98.7	98.6	98.8	98.6	98.3	99.0	98.3	98.6

Sample ID	WZ42V	WZ43	WZ44	WZ45	WZ-46	MK49	MK50	MK51	MK52
(ppm)									
Cr	12.25	9.58	12.60	13.43	13.13	11.10	16.36	18.98	12.36
Co	170	145	120	152	97.60	99.46	169.2	76.80	87.40
Ni	16.66	20.21	14.55	16.80	24.96	39.55	104.58	51.73	35.83
Rb	16.73	11.83	17.67	18.26	20.80	13.41	16.57	41.89	24.16
Sr	23.30	19.07	24.93	60.44	26.44	18.17	25.28	29.88	23.24
Cs	0.62	0.40	0.70	0.66	0.84	0.31	0.41	1.62	0.76
Ba	167.5	121.9	522.6	5680	310.4	56.25	63.58	121.13	82.57
Sc	4.48	3.00	3.62	4.00	5.04	3.07	4.10	8.17	4.83
V	14.61	10.70	10.62	12.81	10.82	17.44	29.62	35.55	20.87
Ta	0.03	0.00	0.02	0.02	0.02	0.01	0.00	0.02	0.02
Nb	0.38	0.03	0.25	0.13	0.20	0.08	0.06	0.33	0.24
Zr	16.71	8.25	15.86	16.50	22.14	12.58	15.62	41.03	22.24
Hf	0.50	0.26	0.46	0.45	0.62	0.36	0.41	1.15	0.63
Th	1.79	0.88	1.81	1.74	2.64	1.03	1.24	3.03	1.59
U	0.82	0.68	0.29	0.30	0.33	0.37	0.35	0.44	0.26
Y	10.37	6.27	10.32	12.30	11.52	9.60	13.33	21.66	18.02
Li	15.42	16.06	16.80	17.49	19.03	11.09	16.65	9.77	11.18
La	8.19	5.00	7.42	8.33	7.61	8.20	14.88	14.18	12.27
Ce	31.35	22.00	26.11	27.94	28.99	24.38	68.09	45.53	26.18
Pr	2.09	1.35	1.91	2.13	2.14	2.24	4.15	3.83	2.99
Nd	8.71	5.66	7.92	8.75	9.07	9.35	16.94	16.48	12.94
Sm	1.95	1.26	1.75	1.99	2.11	2.15	3.59	3.91	2.94
Eu	0.45	0.26	0.41	0.79	0.47	0.45	0.77	0.89	0.65
Gd	1.98	1.28	1.90	2.14	2.14	2.10	3.15	4.16	3.13
Tb	0.27	0.17	0.25	0.30	0.29	0.28	0.43	0.58	0.43
Dy	1.61	1.09	1.49	1.79	1.82	1.66	2.49	3.59	2.72
Ho	0.33	0.21	0.30	0.36	0.35	0.32	0.46	0.71	0.54
Er	0.91	0.60	0.85	1.00	1.04	0.87	1.27	1.96	1.57
Tm	0.13	0.08	0.12	0.14	0.15	0.12	0.17	0.28	0.23
Yb	0.86	0.57	0.78	0.94	0.97	0.77	1.17	1.79	1.44
Lu	0.13	0.08	0.12	0.14	0.15	0.11	0.16	0.27	0.21
∑REE	124.1	85.7	111.4	122.5	129.7	108.6	199.1	219.3	148.1
Cu	27.22	35.69	20.01	33.14	37.52	103.2	101.1	31.97	33.09
Zn	0.00	0.00	0.00	0.00	0.00	0.00	5.54	0.00	-
Ga	16.08	12.20	43.09	484.32	28.19	7.33	8.75	15.47	9.84

Table 2 (Contd….)

Sample ID	MK53	MK54	MK55	MK56	ML131	ML132	ML133	ML134
(wt.%)								
SiO_2	75.59	77.46	76.93	75.50	76.46	77.56	78.41	79.32
Al_2O_3	2.94	2.66	2.75	2.96	2.92	2.66	2.60	2.47
$Fe_2O_3^{(t)}$	5.23	4.97	4.67	4.95	5.78	5.01	4.47	4.81
MnO	0.36	0.27	0.03	0.05	0.25	0.30	0.58	0.49
MgO	2.38	2.33	2.45	2.58	2.32	2.30	2.38	2.25
CaO	6.96	6.99	7.04	7.08	7.12	7.14	6.92	6.96
Na_2O	1.67	1.70	2.11	2.24	1.90	2.06	1.71	1.71
K_2O	1.40	1.12	0.80	1.07	0.79	1.05	0.37	0.64
TiO_2	0.19	0.16	0.15	0.18	0.15	0.17	0.12	0.15
P_2O_5	0.03	0.02	0.03	0.03	0.01	0.03	0.02	0.03
LOI	1.79	1.76	1.51	2.04	1.19	1.42	1.35	1.69
Sum	98.5	99.4	98.5	98.7	98.9	99.7	98.9	100.5

Sample ID	MK53	MK54	MK55	MK56	ML131	ML132	ML133	ML134
(ppm)								
Cr	12.52	12.86	35.93	48.83	13.06	14.56	7.32	0.51
Co	100	139	146	138	135	124	149	1.25
Ni	37.82	29.99	26.78	35.11	23.02	26.83	28.38	0.49
Rb	27.82	22.73	15.97	21.93	16.56	20.23	7.50	13.17
Sr	20.34	18.97	23.73	28.64	23.33	24.94	22.04	27.01
Cs	0.83	0.65	1.21	1.64	0.57	0.67	0.30	0.54
Ba	129	96.09	133.2	156.5	35.49	40.43	52.35	69.32
Sc	5.18	3.97	4.38	5.89	4.14	4.83	2.63	3.82
V	25.01	19.28	22.65	28.39	14.99	16.00	8.76	0.20
Ta	0.02	0.01	-0.01	0.00	0.02	0.01	0.00	0.00
Nb	0.16	0.17	0.03	0.08	0.26	0.20	0.05	0.11
Zr	22.22	14.75	13.82	22.89	13.59	19.57	8.92	14.71
Hf	0.64	0.40	0.43	0.64	0.36	0.54	0.25	0.43
Th	1.76	1.17	0.84	1.21	1.17	1.60	0.58	1.07
U	0.29	0.22	0.62	0.45	0.20	0.23	0.90	0.79
Y	16.08	15.22	11.82	15.25	12.65	13.66	6.96	11.77
Li	9.74	8.87	9.20	10.53	9.92	9.85	31.98	21.32
La	10.57	8.57	6.79	8.86	7.37	8.88	6.03	8.12
Ce	26.04	18.86	9.58	11.78	19.29	23.47	12.76	21.09
Pr	2.66	2.29	1.80	2.35	1.86	2.26	1.53	2.22
Nd	11.22	10.17	7.55	10.04	7.95	9.65	6.34	9.71
Sm	2.55	2.46	1.72	2.45	1.84	2.27	1.43	2.18
Eu	0.59	0.56	0.41	0.54	0.44	0.50	0.33	0.51
Gd	2.76	2.60	1.90	2.56	2.03	2.31	1.45	2.33
Tb	0.39	0.36	0.26	0.34	0.29	0.33	0.19	0.33
Dy	2.43	2.35	1.62	2.23	1.83	1.96	1.18	1.97
Ho	0.49	0.46	0.32	0.43	0.36	0.40	0.22	0.38
Er	1.39	1.31	0.92	1.24	1.07	1.19	0.65	1.05
Tm	0.19	0.17	0.12	0.17	0.15	0.17	0.09	0.15
Yb	1.24	1.11	0.83	1.05	1.00	1.06	0.60	0.92
Lu	0.18	0.17	0.11	0.16	0.15	0.16	0.09	0.14
∑REE	143.8	115.5	97.73	129.51	102.9	121.1	93.9	105.3
Cu	26.19	23.87	38.69	40.08	81.18	88.77	31.19	0.01
Zn	-	-	-	-	-	-	-	0.50
Ga	13.80	10.10	13.41	16.41	5.20	6.10	6.14	7.63

DISCUSSION

Depositional environments

Input from major elements

The primary source for silica is either terrigenous, biogenic i.e. from the siliceous tests and spicules of radiolarians and sponges or chemically precipitated from hydrothermal solutions (Adachi et al., 1986). Fe_2O_3 is relatively enriched in sediments near mid-oceanic ridges and accordingly, has been employed as an indicator of hydrothermal activities. The low TiO_2/Al_2O_3 values ranging from 0.03 to 0.06 (avg.0.06) and higher Fe_2O_3/Al_2O_3 ranging from 1.17 to 1.98 (avg. 1.70), in conjunction with low Cr concentration (avg. 15.61 ppm) in comparison to PAAS (Cr: 110 ppm), negates detrital origin of these cherts and lowers the potential of its source from continental margin environments (Thong et al., 2022). Majority of the samples also exhibit high MnO/TiO_2 values (>1, avg. 2.28) indicative of metalliferous input (Adachi et al., 1986). The studies of Bostrom and Peterson (1969) suggested that the proportion of Al/(AI+Fe+Mn) in marine sediments, serves as an indicator of the hydrothermal influence on sediment composition. In this study, the Al/(AI+Fe+Mn) ratio ranges from 0.26 to 0.38 (avg. 0.30), which is comparably intermediate between the values of hydrothermal cherts (0.01) and biogenic hemiplegic cherts (0.60) from East Pacific rise. However, in the Al-Fe-Mn ternary diagram, the samples of NHO cherts plot within the hydrothermal field (Figure 5a). The $Al_2O_3/(Al_2O_3+Fe_2O_3)$ ratio for most of the studied cherts, varies from 0.34-0.46, which is lower than those of cherts from pelagic basins (<0.4) and continental margins (0.5-0.9) but almost in the range of cherts proximal to mid oceanic ridge (0.4-0.7).

Input from trace elements

In terms of trace elements, U and Th are considered noteworthy elements in distinguishing the hydrothermal and non-hydrothermal origin of sediments (Owen et al., 1999). Normal seawater is generally considered to be enriched in Th, contrastingly hydrothermal water is enriched in U. Therefore, in a non-hydrothermal environment the value of U/Th is less than 1. The U/Th ratio of NHO cherts is less than 1 (0.12–0.78, expect sample ML133 U/Th: 1.57), which is indicative of a normal biogenic sediment with little hydrothermal influence. The PAAS normalized REE patterns however reflect positive Ce anomaly and relatively enriched HREEs which are akin to hydrothermal cherts (Murray, 1994) (Figure 4). Apart from this, The Y/Ho ratio noted for the studied chert samples from NHO to be slightly fractionated ranging from 29.17 to 37.30 similar to chondritic values (28.75; Sun and McDonough, 1989) rather than supra chondritic values resulting from higher residence time of Y as compared to Ho in seawater (Girty et al., 1996; Nozaki et al.,1997) common to hydrothermal waters. The abundance of radiolarian tests seen in petrographic thin sections (Figure. 2b) likely suggests the origin of these cherts to be biogenic as well hydrothermal in origin, which are akin to hydrothermal cherts as observed in previous studies of Adachi et al., (1986).

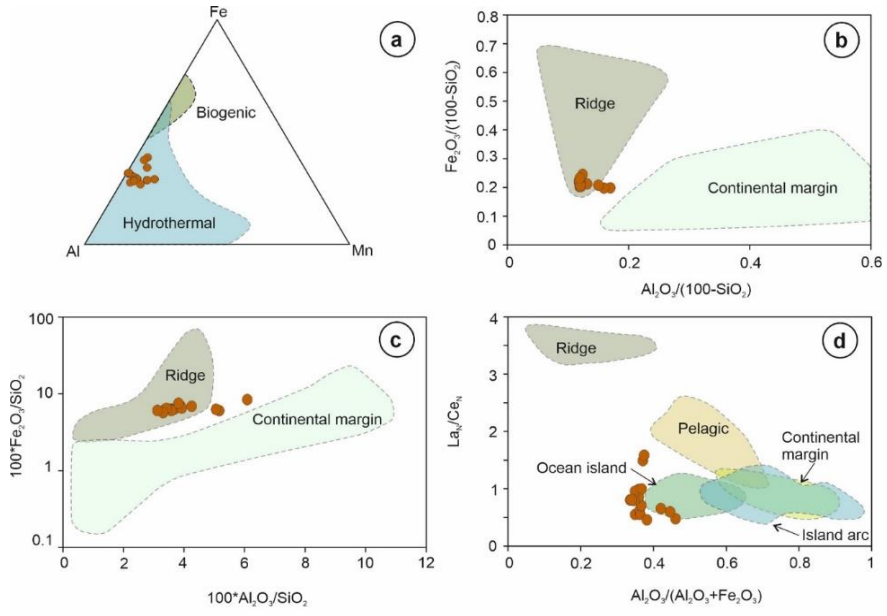

Figure 5. **(a)** Ternary plots of Al-Fe-Mn exhibiting hydrothermal source for the NHO chert (after Bostrom and Peterson, 1969; Yamamoto, 1983; Adachi et al., 1986). Plots showing **(b)** $Al_2O_3/(100-SiO_2)$ vs. $Fe_2O_3/(100-SiO_2)$ after Murray, (1994), **(c)** $100*(Al_2O_3/SiO_2)$ vs. $100*(Fe_2O_3/SiO_2)$ after Murray (1994), and **(d)** $(La/Ce)_N$ vs. $Al_2O_3/(Al_2O_3+SiO_2)$ after Girty et al. (1996) and Murray (1994)tectonic discrimination for the studied cherts.

The REE chemistry is an important indicator to delineate the connection between distinct components in marine system due to their higher susceptibility during post-burial diagenesis (Murray et al., 1990). The REE content in cherts is influenced by terrigenous input, metalliferous materials in hydrothermal fluids from mid-ocean ridges, and the rate of REE absorption. The total REE concentration (ΣREE) trend increases from minimum values of around 10.9 ppm in a mid-oceanic ridge environment to up to 400-500 ppm ^{6} passing away from the ridge in an ocean basin setting, with values being highly scattered, but declining for a continental margin setting (4-110 $\times 10^{-6}$; Murray et al., 1990). The studied chert samples from NHO have ΣREE (32.82-117.72 ppm) lower than PAAS. Studies of Murray et al. (1990) and Murray (1994) are suggestive that cherts formed in close vicinity of ocean ridge environment have La_N/Ce_N ratio greater than 3.5 while a ratio of approximately 1 is indicative of proximity to continental margins. Cherts from the NHO have a positive correlation with Al_2O_3 and TiO_2 and the La_n/Ce_n and Ce/Ce* ratios have a negative correlation, indicating that REE is primarily determined by the influence of terrigenous source. The Ce anomalies are extremely low at the mid-oceanic ridge (Ce/Ce*~0.29), slightly higher in ocean basins (Ce/Ce*~0.55) and increases at continental margins (Ce/Ce*~0.90 to 1.30). The Ce/Ce* is greater than 1 for majority of the studied samples underpinning the influence of the terrigenous source. Rb and Th in the cherts are mainly sourced from continental provenances and are difficult to dissolve in sea water. The positive correlation of Rb, and Th contents with TiO_2, reflects the influx of terrigenous sources. Additionally the diagram showing $(La/Ce)_N$ vs $Al_2O_3/(AL_2O_3+Fe_2O_3)$ indicate they were deposited in pelagic to ocean island environment (Murray, 1994; Girty et al., 1996) (Figure 5d).

The U/Th, Ni/Co and V/(V+Ni) record paleo-redox conditions in the environment of deposition. The U/Th values of <0.75, 0.75-1.25 and >1.25 represent oxic, dysoxix and anoxic redox conditions respectively (Kiliç et al., 2018). The Ni/Co value of <5 are suggestive of oxic depositional states, 5< Ni/Co< 7 values represent dysoxic states and >7 are suggestive of anoxic depositional states (Jonnes and Manning, 1994). In the case of V/V(V+Ni), oxic, dysoxic and anoxic environments are characterized by values ranging <0.46, 0.40-0.60 and 0.54-0.82 respectively (Hatch and Levanthal, 1992). The studied cherts from NHO are corroborating oxic paleo-redox environments as collectively reflected from the values of U/Th ranging from 0.12-0.74 (except for 2 samples); Ni/Co ranging from 0.10-0.67 and V/V(V+Ni) ranging from 0.22-0.47. Additionally, Deng et al. (2017) stated that exceptionally low U are indicative of an oxic deposition. The studied cherts have very low U concentrations 0.20-0.90 ppm which is in accordance with this study.

Geodynamic setting

Field observations and geochemical attributes ubiquitously contribute to comprehend the geodynamic conditions that facilitated the deposition of NHO cherts. These cherts with radiolarian assemblage are oceanic sediments overlying the ultramafic-mafic sequence of NHO and are found interlayered with the ophiolitic basalts. This indicates that the deposition of these cherts post-dated the formation of NHO ultramafic-mafic crust-mantle assemblage and is contemporaneous with basalt volcanism. Thong et al. (2022) suggested that the cherts were deposited in an open ocean basin distal from ridge axes, followed by non-hydrothermal sedimentation under oxic conditions. Micropaleontological and geochemical studies infer that the red cherts of NHO were formed in Upper Jurassic in an active continental margin settings (Ayyamperumal et al., 2021; Aitchison et al., 2019; Baxter et al., 2011). Verencar et al. (2022; 2024a,b) envisaged a SSZ setting marked by subduction initiation, fore-arc extension, subsequent mantle wedge metasomatism and melting for the generation of the ultramafic mafic plutonic lithologies comprising the crust and restitic mantle section of NHO. Previous workers have deduced diverse tectonic environments for the formation of the volcanic sequence of NHO. The basalts of NHO have been classified as Low Ti and High Ti basalts by Sengupta et al. (1989) and Rao et al. (2010). The low Ti rocks were attributed to have overlapping geochemical signatures of MORB and island arc, where as, high Ti basalts have been associated with ocean island volcanism. The distinct hydrothermal and terrigenous signatures for the NHO cherts, as reflected by their geochemical features, conspicuously invoke an expansive depositional realm between a ridge proximal set up and active continental margin aligning with the duality in signature observed for most basalts of the NHO. The geochemical characteristics of the cherts from NHO, clearly indicate spatial variability in their formation from near mid-oceanic ridge to close to continents. Al_2O_3, TiO_2, ΣREE, Ce/Ce*, $(La/Ce)_N$ and other geochemical proxies along with the radiolarian assemblages altogether, suggest a hydrothermally controlled deposition near the mid oceanic ridge with the influence of terrigenous input. Further, the presence of silica cements in voids and channels were not a consequence of silica replenishment; rather, they were a byproduct of interactions between sea water and hydrothermal fluids that caused the silica-rich fluid to rapidly cool. The growth of this silica is influenced by fluid pH levels (Heaney, 1993; Wang et al., 2012). This is preferred in acidic siliceous solutions that cool quickly because silica polymer cross-branching is widely suppressed (Hopkinson et al., 1999; Wang et al., 2012). Recent studies by Imtisunep et al. (2022) suggests a duality in geochemical characters of basalts i.e. N-MORB and E-MORB (enriched-MORB) character. It has been indicated that in general, underlying pillow lavas are showing depleted N-MORB type characters with almost flat LREE patterns

although some amount of E-MORB with enriched REE patterns and depleted HFSE concentrations are also reported from the studied area.

The MORB, IAT and OIB signatures for the basalts associated with the cherts, could be inferred to be linked with waning stage of subduction involving (i) metasomatism and partial melting of mantle wedge generating arc basalts and (ii) arc-rifting in response to slab-pull and subduction retreat thereby stimulating MORB and OIB melt generation though decompression melting of upwelling asthenosphere. Normal faults generated during arc rifting serve as pathways for extensive hydrothermal activity further aided by magma upwelling providing the heat source for seawater circulation. The hydrothermal components for NHO cherts are thus interpreted to be sourced from arc-rifting during subduction termination and ocean basin closure, while the terrigenous input could be derived from the continental margin. Thus, the NHO cherts were deposited in a rifted arc basin, generated by pronounced hydrothermal activity and terrigenous contributed from active continental margin. The major oxide of the studied chert samples are also indicative of a ridge proximal source (Figure 5b, c).

Ocean basins associated with diverse tectonic realms including abyssal ocean basin, back-arc basin, island arc, continental rift basin are envisaged as favorable environments for deposition of cherts. This distinct tectonic affiliation is imprinted on the lithological features and geochemical attributes of the deposited cherts. Major and trace element geochemistry of Middle Jurassic radiolarian cherts, associated with Dajiweng ophiolite of SW Tibet, conform to a transitional environment between an ocean basin and active continental margin (Cui et al., 2021). Likewise, the geochemical features of ophiolitic cherts from Qinling orogenic belt suggest their deposition in an extensional ocean basin closely associated with an active continental margin (Zhang et al., 2004). REE signatures of Arenig cherts from Ballantrae ophiolite, southern Scotland, propound their formation in a rifted arc basin close to an active continental margin. (Armstrong et al,1999).

The Tethyan ophiolites viz. Pindos ophiolite (Greece), Kizildag ophiolites (Turkey), Troodos ophiolites (Cyprus) and Semail ophiolites (Oman), hosts Fe-Cu ore deposits, metalliferous sedimentary rocks, red and Mn-rich cherts evidencing hydrothermal activity (Gills and Banerjee, 2000). Though the studies of Thong et al. (2022) support that the silica of these Late Jurassic-Early Cretaceous NHO cherts are, pre-dominantly biogenic and are derived from radiolarians and other siliceous microfossils in an open ocean basin, distal from oceanic ridge axes, however; few samples also show identical ocean island characteristics and minor signatures of influence of hydrothermal solutions. The bio stratigraphic correlations indicate a wide geological time from Neo-Tethyan basin opening to nearing closure i.e. Late Jurassic to Late Cretaceous (Agrawal, 1985; Baxter et al., 2011). The bimodal contribution of terrigenous and hydrothermal components towards the deposition of NHO cherts corroborates a rifted arc basin, in close association with active continental margin set up. This transitional tectonic regime complies with magmatism and subsequent sedimentation in a rifted arc basin proximal to an active continental margin tectonically concomitant to slab tearing and subduction termination, ocean basin closure and consequent accretion-collisional processes.

CONCLUSION

This study demonstrates the origin and depositional environment of cherts from NHO in terms of its geochemical characteristics. Following main conclusions are drawn from this study:

(i) Geochemical data suggest a hydrothermal origin for the studied cherts along with input from the terrigenous source.

(ii) Occurrence of radiolarian tests are indicative of presence of biogenic silica.

(iii) The paleo-redox conditions demonstrated by U/Th, V/(V+Ni), Ni/Co values for the studied chert samples, corroborate an oxic environment for their deposition.

(iv) This study infers a transitional tectonic realm associated with magmatism and subsequent sedimentation in a rifted arc basin proximal to an active continental margin.

Acknowledgements:

AV and AS are grateful to the Director, CSIR-National Institute of Oceanography for his encouragement, support and permission to publish this work. AS acknowledges the funding received from the Science and Engineering Research Board (SERB), Govt. of India under ECR/2018/000309. The authors sincerely acknowledge Mr. Robin John, Central Analytical Facility, CSIR-NIO for his kind help during HR-ICPMS data generation. The authors sincerely acknowledge the facilities received from the CFC (Common facility center)-SAIF (Sophisticated analytical instrumentation facility) Center; Shivaji University Shivaji University for XRD analyses. AV acknowledges Council of Scientific and Industrial Research (CSIR) for Senior Research Fellowship (Grant no. RF85094) and Goa State Research Foundation (GSRF) for necessary funding. We also thank two anonymous reviewers and Editor-in-chief for their constructive comment and suggestions. This is part of Ph.D. thesis of AV. This is NIO's contribution no.7388.

Author Credit Statement

AV: Investigation, visualization and writing-original draft, AS: Conceptualization; visualization data curation; funding

acquisition; methodology; project administration, supervision, writing-review and editing, RM: Formal analysis, writing-review and editing.

Data Availability

Data can be made available on reasonable request to the corresponding author

Compliance with Ethical Standards

The authors declare that they have no conflict of interest and adhere to copyright norms.

References

Acharyya, S. K., 2007. Collisional emplacement history of the Naga-Andaman ophiolites and the position of the eastern Indian suture. J. Asian Earth Sci., 29, 229-242.

Adachi, M., Yamamoto, K. and Sugisaki, R., 1986. Hydrothermal chert and associated siliceous rocks from the northern Pacific their geological significance as indication of ocean ridge activity. Sediment. Geol., 47, 125-148.

Agrawal, O. P. and Ghose, N. C., 1986. Geology and stratigraphy of the Naga Hills ophiolite between Melluri and Awankhoo, Pheek District, Nagaland, India. In Indian chapter IGCP Projects 195 and 197. Meeting (pp. 163-195).

Agrawal, O. P., 1985. Geology and geochemistry of the mafic-ultramafic complex of Indo-Burman ranges between Meluri and Awankhoo, Phek district, Nagaland, India. Unpublished Ph. D. thesis, Patna University, Patna.

Aitchison, J. C., Ao, A., Bhowmik, S., Clarke, G. L., Ireland, T. R., Kachovich, S., Lokho, K., Stojanovic, D., Roedae, T., Truscott, N., Zhen Y. and Zhou, R., 2019. Tectonic evolution of the western margin of the Burma microplate based on new fossil and radiometric age constraints. Tectonics, 38, 1718-1741.

Aldanmaz, E., Yaliniz, M. K., Guectekin, A. Y. K. U. T. and Göncüoğlu, M. C., 2008. Geochemical characteristics of mafic lavas from the Neotethyan ophiolites in western Turkey: implications for heterogeneous source contribution during variable stages of ocean crust generation. Geol. Magazine, 145, 37-54.

Ao, A., and Bhowmik S. K., 2014. Cold subduction of the Neotethys: the metamorphic record from finely banded lawsonite and epidote blueschists and associated metabasalts of the Nagaland Ophiolite Complex, India. J. Metamorphic Geol., 32, 829-860.

Armstrong, H. A., Owen, A. W. and Floyd, J. D., 1999. Rare earth geochemistry of Arenig cherts from the Ballantrae Ophiolite and Leadhills Imbricate Zone, southern Scotland: implications for origin and significance to the Caledonian Orogeny. J. of the Geol. Soc., 156, 549-560.

Ayyamperumal, R., Sooriamuthu, R., Gopalakrishnan, G., Biswa, G., Perumal, R., Gahlaut, P., Nuzrat, N. and Antony, J. K., 2021. Micropalaeontological and Geochemical Evidence of the Late Jurassic Radiolarians Cherts of Naga Ophiolite Hill, Nagaland, Northeast-India. Open J. Geology, 11, 356-372.

Baxter, A. T., Aitchison, J. C., Zyabrev, S. V. and Ali, J. R., 2011. Upper Jurassic radiolarians from the Naga ophiolite, Nagaland, northeast India. Gond. Res., 20, 638-644.

Bhowmik, S. K., and Pradhan, B., 2024. Mesozoic tectonics of the Indo-Burmese wedge: a record from the high-pressure metamorphic rocks of the Nagaland-Manipur Ophiolite Belt, NE India. Proc. Indian National Science Academy, 1-13.

Bhowmik, S. K., Ao, A., and Rajkakati, M., 2022. Tectonic framework of the high-pressure metamorphic rocks of the Nagaland Ophiolite Complex, North-east India, and its geodynamic significance: A review. Geol. J., 57, 727-748.

Bostrom, K. and Peterson, M. N. A., 1969. The origin of aluminum poor ferromanganoan sediments in areas of high heat flow on the East Pacific Rise. Marine Geol., 7, 427–447.

Chatterjee, N., and Ghose, N. C., 2010. Metamorphic evolution of the Naga Hills eclogite and blueschist, Northeast India: implications for early subduction of the Indian plate under the Burma microplate. J. Metamorphic Geol., 28, 209-225.

Cui, X., Luo, H., Aitchison, J. C. and Li, X., 2021. Middle Jurassic radiolarians and chert geochemistry, Dajiweng ophiolite, SW Tibet: Implications for Neotethyan Ocean evolution. J. Asian Earth Sci., 221, 104947

Deng, Y., Ren, J., Guo, Q., Cao, J., Wang, H. and Liu, C., 2017. Rare earth element geochemistry characteristics of seawater and porewater from deep sea in western Pacific. Scientific Reports, 7, 16539.

Dey, A., Hussain, M. F. and Barman, M. N., 2018. Geochemical characteristics of mafic and ultramafic rocks from the Naga Hills Ophiolite, India: implications for petrogenesis. Geosci. Frontiers, 9, 517-529.

DGM, 1978. Directorate of Geology and Mining, Nagaland, Misc. Publ. No. 1,1978.

Garbán, G., Martínez, M., Márquez, G., Rey, O., Escobar, M., and Esquinas, N., 2017. Geochemical signatures of bedded cherts of the upper La Luna Formation in Táchira State, western Venezuela: Assessing material provenance and paleodepositional setting. Sediment. Geol., 347,130–147

Ghose, N. C. and Agrawal, O. P., 1989. Geological framework of the central part of Naga Hills. Phanerozoic ophiolites of India and associated mineral resources. Sumna Publications, Patna, 165-188.

Ghose, N. C., Agrawal, O. P. and Srivastava, S. C., 1987. Metamorphism of the ophiolite belt of Nagaland, NE India. In: Proc. National Seminar Tertiary Orogeny, pp. 189-213.

Ghose, N. C., Agrawal, O. P., and Chatterjee, N., 2010. Geological and mineralogical study of eclogite and glaucophane schists in the Naga Hills Ophiolite, Northeast India. Island Arc, 19, 336-356.

Ghose, N. C., Chatterjee, N. and Fareeduddin, A., 2014. A petrographic atlas of ophiolite: an example from the Eastern India-Asia collision zone (p. 216). Springer India.

Gillis, K. M. and Banerjee, N. R., 2000. Hydrothermal alteration patterns in supra-subduction zone ophiolites. Special Papers-Geological Society of America, 283-298.

Girty, G. H., Ridge, D. L., Knaack, C., Johnson, D. and Al-Riyami, R. K., 1996. Provenance and depositional setting of Paleozoic chert and argillite, Sierra Nevada, California. J. Sediment. Res., 66, 107–118.

Hatch, J. R., and Leventhal, J. S., 1992. Relationship between inferred redox potential of the depositional environment and geochemistry of the Upper Pennsylvanian (Missourian) Stark Shale Member of the Dennis Limestone, Wabaunsee County, Kansas, USA. Chem. Geol., 99, 65-82.

Heaney, P. J., 1993. A proposed mechanism for the growth of chalcedony. Contr. Mineralogy and Petrology, 115, 66-74.

Hopkinson, L., Roberts, S., Herrington, R. and Wilkinson, J., 1999. The nature of crystalline silica from the TAG submarine hydrothermal mound, 26 N Mid Atlantic Ridge. Contr. Mineralogy and Petrology 137, 342-350.

Huang, H., Du, Y. S., Yang, J., Huang, H., Tao, P., Huang, Z. et al., 2013. Geochemistry of the Late Paleozoic cherts in the

Youjiang Basin: Implications for the basin evolution. J. Palaeogeog., 2, 402–421.

Hussain, M. F. and Dey, A., 2022. Geochemical characteristics of mafic intrusive rocks from the Naga Hills Ophiolite, north-east India: Constraints on petrogenesis and tectonic setting. Geol. J., 57, 5222-5238.

Imtisunep, S., Singh, A. K., Bikramaditya, R., Khogenkumar, S., Chaubey, M. and Kumar, N., 2022. Evidence of intraplate magmatism and subduction magmatism during the formation of Nagaland–Manipur Ophiolites, Indo–Myanmar Orogenic Belt, north-east India. Geol. J., 57, 782-800.

Jochum, K. P., Weis, U., Schwager, B., Stoll, B., Wilson, S. A., Haug, G. H., Andreae, M.O, and Enzweiler, J., 2016. Reference values following ISO guidelines for frequently requested rock reference materials. Geostandards and Geoanalytical Res.40, 333-350.

Jones, B. and Manning, D. A., 1994. Comparison of geochemical indices used for the interpretation of palaeoredox conditions in ancient mudstones. Chem. geol., 111, 111-129.

Kacker, R. and Roy, R., 1980. Geology and mineral resources of naga hills orogenic belt in a tethyan domain along eastern peri-indian suture. A preliminary geological synthesis.

Kato, Y., Nakao, K. and Isozaki, Y., 2002. Geochemistry of Late Permian to Early Triassic pelagic cherts from southwest Japan: Implications for an oceanic redox change. Chem. Geol., 182, 15–34

Khogenkumar, S., Singh, A. K., Kumar, S., Lakhan, N., Chaubey, M., Imtisunep, S., Dutt A. and Oinam, G., 2021. Subduction versus non-subduction origin of the Nagaland-Manipur Ophiolites along the Indo-Myanmar Orogenic Belt, northeast India: Fact and fallacy. Geol. J., 56, 1773-1794.

Kiliç, G., Selman Aydoğan, M. and Kumral, M., 2018. Preliminary results of the radiolarian-chert hosted manganese deposit within the Vezirler ophiolitic mélange (Kula-Manisa, western Turkey): constraints on the origin, paleo-redox conditions, and depositional environments. Arab. J. Geosc., 11, 1-22.

Krishna, A. K., Murthy, N. N. and Govil, P. K., 2007. Multielement analysis of soils by wavelength-dispersive X-ray fluorescence spectrometry. Atomic Spectroscopy-Norwalk Connecticut, 28, 202.

Mathur, L. P., and Evans, P., 1964. Oil in India. Int. Geol. Cong. 22nd Session, New Delhi.

Murray, R. W., 1994. Chemical criteria to identify the depositional environment of chert: General principles and applications. Sed. Geol., 90, 213–232.

Murray, R. W., Buchholtz Ten Brink, M. R., Jones, D. L., Gerlach, D. C. and Russ, G. P., 1990. Rare earth elements as indicators of different marine depositional environments in chert and shale. Geol., 18, 268–271.

Ningthoujam, P. S., Dubey, C. S., Guillot, S., Fagion, A. S. and Shukla, D. P., 2012. Origin and serpentinization of ultramafic rocks of Manipur Ophiolite Complex in the Indo-Myanmar subduction zone, Northeast India. J. Asian Earth Sci., 50, 128-140.

Nozaki, Y., Zhang, J. and Amakawa, H., 1997. The fractionation between Y and Ho in the marine environment. Earth Planet. Sci. Lett.,148, 329–340

Owen, A. W., Armstrong, H. A. and Floyd, J. D., 1999. Rare earth element geochemistry of upper Ordovician cherts from the Southern Uplands of Scotland. J. Geol. Soc., 156, 191-204.

Rao, B. V., Ezung, C. and Nayak, R., 2010. Geology, genesis and tectonic setting of volcanic rocks from Naga Ophiolite belt. Geol. Soc. India. Mem., 75, 317–327.

Robertson, A. H., 2002. Overview of the genesis and emplacement of Mesozoic ophiolites in the Eastern Mediterranean Tethyan region. Lithos, 65, 1-67.

Saha, A., Santosh, M., Ganguly, S., Manikyamba, C., Ray, J. and Dutta, J., 2018. Geochemical cycling during subduction initiation: Evidence from serpentinized mantle wedge peridotite in the south Andaman ophiolite suite. Geoscience Frontiers, 9, 1755-1775.

Saha, A., Mudholkar, A. V., Kamesh Raju, K. A., Doley, B. and Sensarma, S., 2019. Geochemical characteristics of basalts from Andaman subduction zone: Implications on magma genesis at intraoceanic back-arc spreading centres. Geol. J., 54, 3489-3508

Sengupta, S., Acharyya, S. K., Van Den Hul, H. J. and Chattopadhyay, B., 1989. Geochemistry of volcanic rocks from the Naga Hills ophiolites, northeast India and their inferred tectonic setting. J. Geol. Soc., 146, 491-498.

Singh, A. K., Khogenkumar, S., Singh, L. R., Bikramaditya, R. K., Khuman, C. M. and Thakur, S. S., 2016. Evidence of Mid-ocean ridge and shallow subduction forearc magmatism in the Nagaland-Manipur ophiolites, northeast India: constraints from mineralogy and geochemistry of gabbros and associated mafic dykes. Geochemistry, 76, 605-620.

Sun, S. S. and McDonough, W. F., 1989. Chemical and isotopic systematics of oceanic basalts: implications for mantle composition and processes. Geol. Soc., London, Special Publications, 42, 313-345.

Taylor, S. R. and McLennan, S. M., 1985. The continental crust: Its composition and evolution. Oxford: Blackwell Scientific

Taylor, S. R. and McLennan, S. M., 1995. The geochemical evolution of the continental crust. Rev. geophys., 33, 241-265.

Thong, G. T., Imchen, W., and Walling, T., 2022. Geochemical evidences on the origin and paleo-oceanic depositional setting of the Naga Hills Ophiolite cherts, North East India. Geol. J., 57, 3114-3134.

Verencar, A., Saha, A., Ganguly, S. and Manikyamba, C., 2021. Tectono-magmatic evolution of Tethyan oceanic lithosphere in supra subduction zone fore arc regime: Geochemical fingerprints from crust-mantle sections of Naga Hills Ophiolite. Geosci. Frontier, 12, 101096.

Verencar, A., Saha, A., Ganguly, S., Satyanarayanan, M., Doley, B., and Mohan, M. R., 2022. Multistage melt impregnation in Tethyan oceanic mantle: Petrochemical constraints from channelized melt flow in the Naga Hills Ophiolite. Geochem., 82(1), 125821.

Verencar, A., Saha, A., Ganguly, S., Satyanarayanan, M. and Mohan, M. R., 2024a. Geochemical dichotomy of Tethyan oceanic mantle and the supercontinent connection: Insights from Os isotopic signatures of mantle peridotites from Naga Hills ophiolite. Gond. Res., 128, 424-438.

Verencar, A., Saha, A., Sorcar, N., Ganguly, S., Kumar, P. and Singh, A. K., 2024b. Hydro-uvarovite from Mantle Peridotites of Naga Hills Ophiolite: A Mineral Tracer for Neo-Tethyan

Mantle Wedge Metasomatism. Acta Geologica Sinica-English Edition, 98, 867-877.

Vidyadharan, K. T., Joshi, A., Ghose, S., Gaur, M. P., Sukla, R. and Ghose, N. C., 1989. Manipur ophiolites: its geology, tectonic setting and metallogeny. Phanerozoic Ophiolites of India, Suman Publ, 197-212.

Wang, J., Chen, D., Wang, D. A. N., Yan, D., Zhou, X. and Wang, Q., 2012. Petrology and geochemistry of chert on the marginal zone of Yangtze Platform, western Hunan, South China, during the Ediacaran–Cambrian transition. Sedimentology, 59(3), 809-829.

Yamamoto, K.,1983. Geochemical study of Triassic bedded cherts from Kamiaso, Gifu Prefecture. J. Geol. Soc. Jap., 89, 143–162.

Zhang, C., Gao, S., Zhang, G., Guo, A., Yuan, H., Liu, X. and Wang, J., 2004. Geochemistry of ophiolite cherts from the Qinling orogenic belt and implications for their tectonic settings. Science in China Series D: Earth Sci., 47, 329-337.

Appendix 1. Trace and REE analyses of Certified Reference Material

Sample	JB2			JA 1		
(ppm)	Observed values (n=3)	RSD	Reported values	Observed values (n=3)	RSD	Reported values
Cr	27.0	0.35	26.7	5.38	16.9	7.50
Co	36.9	0.78	37.6	10.7	1.93	11.5
Ni	14.7	1.15	14.8	3.16	9.06	2.20
Rb	5.94	0.28	6.40	9.54	1.67	11.0
Sr	179	1.16	178	254	2.17	259
Cs	0.70	1.48	0.80	0.56	1.22	0.63
Ba	218	0.52	218	305	1.38	304
Sc	53.6	1.04	54.1	26.5	0.48	27.9
V	574	9.86	572	83.5	2.47	106
Ta	0.03	6.40	0.04	0.09	0.73	0.10
Nb	0.46	4.44	0.57	1.21	1.23	1.33
Zr	47.2	2.28	48.3	83.3	0.53	83.7
Hf	1.48	1.12	1.49	2.58	0.43	2.51
Th	0.23	4.62	0.26	0.73	2.39	0.76
U	0.14	2.88	0.15	0.32	2.53	0.34
Y	22.4	2.03	23.6	26.9	0.31	28.0
Li	8.08	2.34	8.08	10.5	0.81	10.4
La	2.10	1.92	2.28	4.63	1.57	4.88
Ce	5.85	0.94	6.55	12.1	0.86	13.2
Pr	1.03	2.79	1.13	1.89	1.02	2.08
Nd	5.83	1.73	6.39	9.98	0.73	10.7
Sm	2.15	1.88	2.27	3.25	0.17	3.40
Eu	0.77	1.67	0.84	1.00	1.18	1.11
Gd	3.04	1.97	3.12	3.96	0.89	4.15
Tb	0.51	1.58	0.59	0.63	1.06	0.73
Dy	3.57	0.36	3.87	4.29	1.97	4.75
Ho	0.77	2.27	0.86	0.90	2.19	1.03
Er	2.34	2.24	2.54	2.68	1.52	2.96
Tm	0.35	3.28	0.39	0.39	0.42	0.45
Yb	2.33	2.02	2.53	2.65	1.54	2.95
Lu	0.36	4.02	0.39	0.41	1.27	0.45
Cu	212	1.00	222	42.60	2.47	42.5
Pb	7876	2.31	5.25	8296	2.99	5.86
Zn	94.3	2.50	110	65.58	8.27	88.3
Ga	30.5	1.33	16.6	36.43	2.38	16.7

Reported values from Jochum et al. (2016)

Received on: 02-12-2024; Revised on: 18-02-2025; Accepted on: 28-02-2025

J. Ind. Geophys. Union, 29(2) (2025), 81-85
https://doi.org/10.71122/JIGU.29(2)2025.009

Examining the salinity changes at different depths in the Indian Ocean prior to summer monsoon season and its connection to monsoon arrival in India: A case study

Dinesh K Yadav[1], Archana Maurya[1], R. Bhatla[1,2] and B. Mandal*[1]

[1]*Department of Geophysics, Institute of Science, Banaras Hindu University, Varanasi-221005, India.*

[2]*DST-Mahamana Centre of Excellence in Climate Change Research, Institute of Environment and Sustainable Development, Banaras Hindu University, Varanasi-221005, India.*

*****Corresponding author**:** barunavamandal@gmail.com

ABSTRACT

The Indian Ocean interacts intricately with the atmosphere, and its features, such as sea surface temperature and salinity. The Indian Ocean can influence the monsoon's onset, intensity, and duration. This study examines the fluctuation of the salinity in the Indian Ocean throughout the onset phase over the Indian Peninsula, with a focus on the Kerala coast. The study makes use of daily averaged reanalysis data from 1992 to 2017 from the Ocean Reanalysis System 5 (ORAS) of the European Centre for Medium-Range Weather Forecasts (ECMWF). Considerable variations in salinity have been seen in the Indian Ocean prior to the onset of the monsoon. Higher salinity levels are found in the top subsurface layers of the western Indian Ocean, namely the Arabian Sea, whereas lower salinity concentrations are found in the equivalent layers of the eastern Indian Ocean, which include the Bay of Bengal. The salinity gradient between the Arabian Sea and Bay of Bengal decreases with depth due to the inflow of freshwater into Bay of Bengal through river discharge. The peak salinity is localized in a specific region, adjacent to the Somalia and Kenya coastlines, within depths ranging from 20 to 80 meters from March to the first week of May. Subsequently, this region of heightened salinity, extends to depths ranging from 50 to 90 meters. During the pre-monsoon months of the early onset year, intense evaporation leads to immense moisture in the atmosphere. Conversely, moisture is low during normal onset and late onset years, with wind-driven moisture transport towards the Kerala coast.

Keywords: Indian Ocean, Summer Monsoon, Sea Surface Temperature, Salinity, Kerala Coast

INTRODUCTION

The Indian Summer Monsoon is a crucial meteorological phenomenon that profoundly shapes India's climate and agricultural productivity (Gadgil and Rupa Kumar, 2006). It describes the precipitation that falls across the Indian subcontinent as a result of the seasonal reversal of winds, which usually occurs from June to September (Goswami et al., 1999; Krishnan et al., 2013). According to the Indian meteorological calendar, the onset of the Indian Summer Monsoon over southern India, also known as Monsoon Onset over Kerala, signifies the beginning of the rainy season (Ananthakrishnan and Soman, 1988). The onset of the Indian monsoon is accompanied by significant transformations in atmospheric circulation patterns. This dramatic shift includes major changes in wind patterns, pressure systems, and overall atmospheric flow across the region (Ananthakrishnan et al., 1983). The Southwest Monsoon Current, which flows generally eastward in the northern Indian Ocean throughout the summer, circles around Sri Lanka and enters the Bay of Bengal after traveling eastward south of India (Vinayachandran et al., 1999). The onset dates of the monsoon over Kerala, show a strong positive correlation with how often the zonal index at 500 hPa level occurs in the region between 160°E-45°W and 35°N-70°S (Bhatla and Chattopadhyay, 2003). Small changes in the commencement date, can have a significant impact on particularly sensitive areas even if the monsoon season's total average rainfall is normal (Raju et al., 2007). Bhatla et al. (2016a) examined changes in surface meteorological fields and approximated surface heat fluxes associated with the onset of the summer monsoon seasons based on 50-year data collected over India from 1957 to 2006. There are some impact of Madden Julian Oscillation on onset of Indian Summer Monsoon studied by Bhatla et al. (2017). The annual fluctuation of sea surface salinity anomalies moves earlier than that of sea surface temperature anomalies in similar places because of changes in wind stress and freshwater flow (Yuan et al., 2018). Some studies have also been carried out by modelling to simulate the onset of monsoon over India (Bhatla et el., 2015, 2016b, 2019). Fasullo and Webster (2003) utilized vertically integrated moisture transport, while Taniguchi et al. (2010) observed a strong link between rapid wind speed increases and the sudden start of the rainy season. Wang et al. (2009) suggested a straightforward definition based solely on the 850 hPa wind field. The factors affecting salinity changes with depth in the Indian Ocean during monsoon season, are complex and vary across different oceanic regions (Skliris et al., 2014). To create an extended time series of Indian Summer Monsoon onset dates, using a consistent and objective method, researchers have investigated defining the onset through algorithms using pre-satellite era variables such as precipitation, moisture transport, and wind (Ordoñez et al., 2016).

Our study focuses on analyzing the year-to-year changes in salinity throughout various depths of the Indian Ocean, exploring both the patterns and underlying reasons for these variations. We also examined how these salinity changes influence the timing of the monsoon's arrival in India. Understanding these salinity fluctuations prior to the monsoon

season is crucial, as it provides valuable insights for scientists and policymakers in their decision-making processes related to water usage and resource management strategies.

DATA AND METHODOLOGY

The Monsoon Onset over Kerala dates, were obtained from Roman-Stork et al. (2020). Years 2000, 2001 and 2003 (1st June, 26th May, and 13th June respectively) have been selected for this study due to large departure from normal onset within four years. Our salinity analysis relies on data from the Estimating the Circulation and Climate of the Ocean (ECCO) project, specifically Version 4 Release 4 (V4r4). This dataset provides daily mean ocean salinity estimates interpolated to a regular 0.5-degree grid. The ECCO project reconstructs three-dimensional, time-varying Ocean, sea-ice, and surface atmospheric conditions. Initial and boundary conditions are derived from the European Centre for Medium-Range Weather Forecasts (ECMWF) ORAS5 Interim reanalysis. This data is provided daily (every 24 hours) with a 1° x 1° latitude/longitude horizontal grid and 50 vertical levels. We've used the daily salinity data to calculate monthly salinity averages at various depth levels (5, 25, 55, and 75 meters).

Raju et al. (2005) have categorized onset in India into three parts (early onset, normal onset, and late onset). This study examines the spatial patterns of monthly salinity changes across the Indian Ocean, encompassing the area from 30°E to 110°E and 30°S to 25°N. Within this broad region, we find large variation in salinity near Somalia's coast and its adjoining eastern part of the Indian Ocean. The southwest monsoonal wind cross this broad region before entering in India. There are some issues in analyzing this due to the broad region, therefore, we divided this broader region into two sub-regions R1 (40°E-60°E, 9°S-9°N) and R2 (60°E-80°E, 9°S-9°N), and focus on these smaller sub-regions, each measuring 20° by 18°. For these two sub-regions, we conducted a more detailed analysis of daily salinity variations from the surface down to 400 meters depth, below 400 meters depth salinity variation was found similar in every years. We designated Early onset years, Late onset years and Normal onset years are those when onset falls within ±2 days of its mean date (June 1st) (Table 1).

RESULTS AND DISCUSSION

The spatial distribution of salinity at different depths in the Indian Ocean during March, April and May (MAM) of three different years (2001, 2000 and 2003) is depicted in (Figures1) and 2) for the pre-onset, onset and post-onset of monsoon over India. The distribution of salinity for 5 and 25 meters depths, shows a very distinct pattern with minimum salinity in the northern Bay of Bengal, while maximum salinity in the north Arabian Sea and southern Tropical Indian Ocean. Salinity decreased gradually southward from the head of the Arabian Sea. In contrast, from the head of the Bay of Bengal, it increased gradually towards the equator. While having the same latitude band, Arabian Sea and Bay of Bengal, show contrasting salinity characteristics on opposite features due addition of fresh water in the Bay of Bengal (Rao and Shivakumar, 2003; Rao, 2015). During MAM in 2001, salter water was observed near the northern coast of Somalia which becomes less salter towards the south. A large area of high salinity (35.6 PSU) has been observed near the east of Kenya, elongated in an east-west direction which gently decreased towards east at the uppermost sub surface (Figure 1a). At 25 meters depth during MAM, more or less same distribution of salinity has been observed as 5 meters depth, the salinity decreased more gradually toward the east at 25 meters depth as compared to 5 meters depth (Figure 1d).

Near the Kerala coast, high salinity was observed during MAM in 2001 at 55 meters depth, which decreases rapidly towards south while moderately decreasing westward (Figure 2a). At the lower subsurface (75 m), high salinity is observed near the Kerala coast during MAM 2001. Contrast between Arabian Sea and Bay of Bengal become lessen and also salter water has been observed near Indonesia as compared to the upper subsurface (Figure 2d). During MAM 2000 at 5 meters depth, small area of high salinity (35.6 PSU) elongated in east-west direction, has been observed east of Kenya coast and east of north Somalia coast. Low salinity has been observed near the Kerala coast (Figure 1b). At 25 meters depth during MAM 2000 more or less same distribution of salinity has been observed as 5 meters depth with smaller area of high salinity over east of Kenya coast. (Figure 2b**)** shows high salinity near the Kerala coast which decreased gradually southward and salter water has transported towards Indonesia at 55 meters depth during MAM 2000. Salinity near Kerala coast has been increased at the lower sub surface (75 meters), which has gradually decreased towards south west direction while rapidly towards southward, and the amount of salt water in Bay of Bengal and near Indonesia has been increased (Figure 2e).

Table 1. Categorization of onset years of summer monsoon over India.

Category	Years
Early onset	1994,1999,2001,2004,2006,2007 and 2009
Normal onset	1993,1998,2000,2008,2010,2011 and 2013
Late onset	1992,1995,1996,1997,2002,2003,2004,2005,2012,2014,2015 and 2016

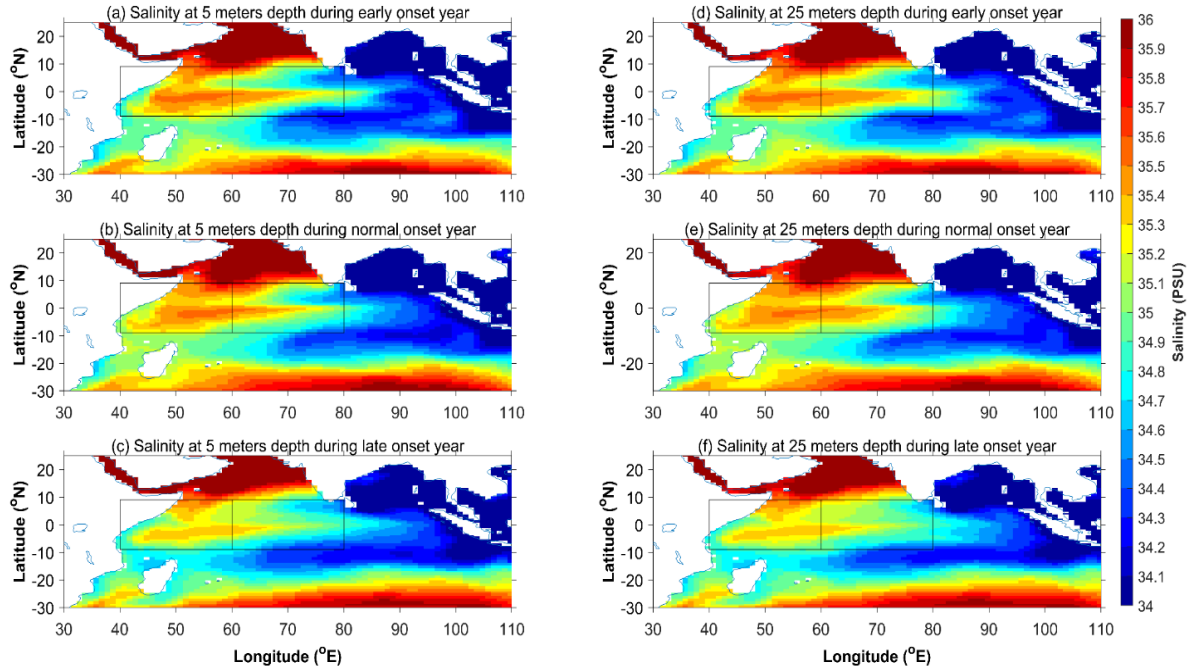

Figure 1. The salinity distribution in Indian Ocean during pre-monsoon season (2001, 2000 and 2003) at 5 and 25 meters depth levels.

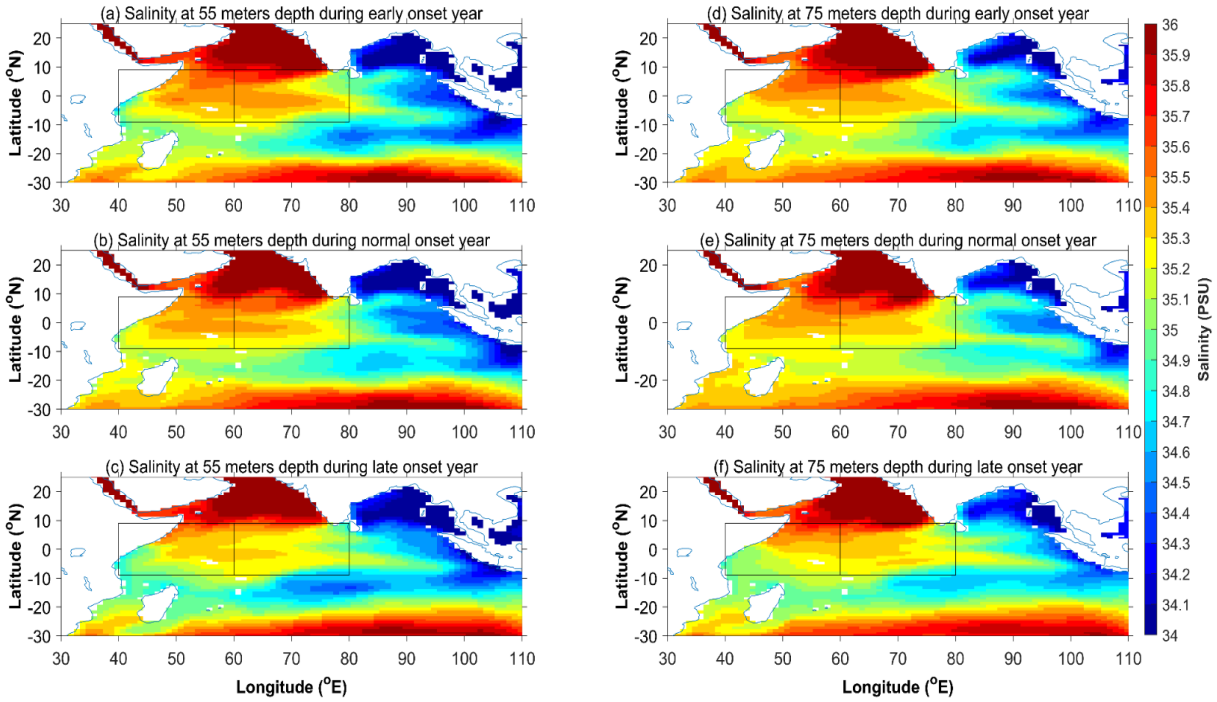

Figure 2. The salinity distribution in Indian Ocean during pre-monsoon season (2001, 2000 and 2003) at 55 and 75 meters depth levels.

During MAM 2003, high salinity (35.5 PSU) has been observed near the northeast coast of Somalia and east of Kenya coast which has elongated in E-W direction below the equator. Near the Kerala coast, low salinity (34.5 PSU) has been observed (Figure 1c). At 25 meters depth, distribution of salinity has been observed almost same as 5 meters depth with eastward transported of salt water.

Near Somalia and Kenya coast, high salinity has been observed which has decreased gently southward and eastward towards Indonesia at 55 meters depth (Figure 2c). The salinity near the Kerala coast and Indonesia has increased at 75 meters depth during MAM 2003 and the contrast between Arabian Sea and BoB has been decreased (Figure 2f).

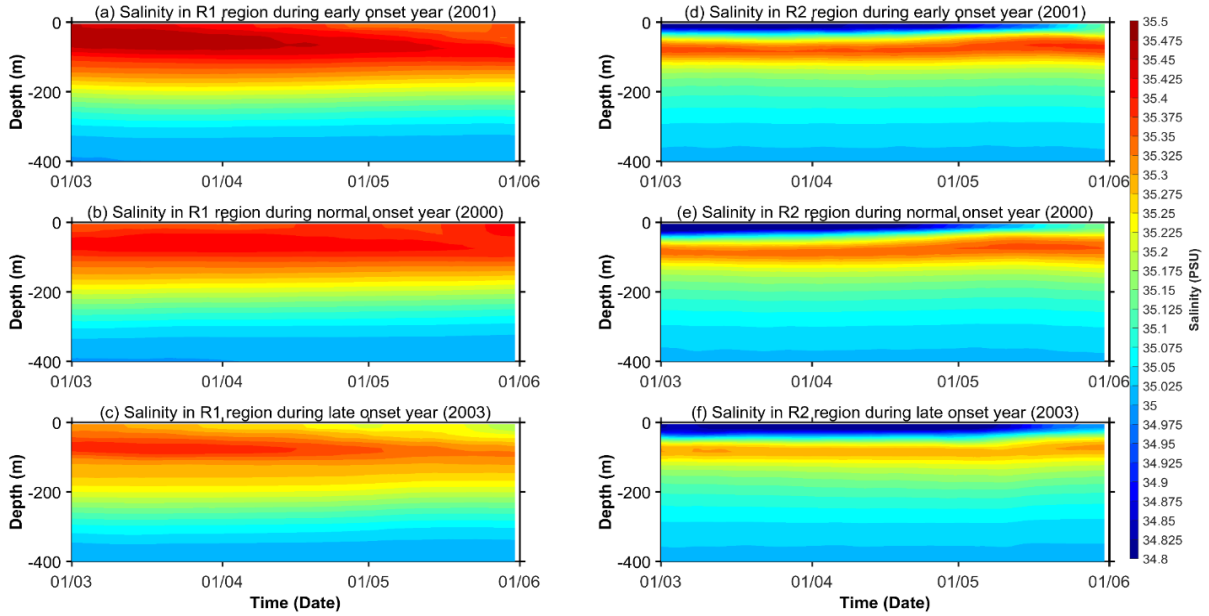

Figure 3. The distribution of salinity with depth in two different sub regions, R1 and R2, during March, April and May (2001, 2000 and 2003).

Figure 3 shows the distribution of salinity with depth in two sub regions R1 (Figure 3 a-c) and R2 (Figure 3 d-f) during MAM in 2000, 2001, and 2003, salinity varies rapidly with depth while gently with time. A high salinity (35.5 PSU) has been observed between 20 to 80 meters depth from the beginning of March to mid-April due to immense evaporation after that salinity diminished gradually till May at the same depth in R1. In the beginning of March high salinity was observed in the uppermost sub-surface, which decreased gently till the last week of May. Below 100 meters depth, salinity lessens gradually (Figure 3a). In 2000, during MAM, high salinity was observed in the upper sub-surface (up to 100 meters depth) and after that decreased rapidly with depth (Figure 3b). During MAM 2003, high salinity (35.425 PSU) was observed from 50 to 80 meter depth till mid-April due to low evaporation, further lessen gently with time and in the upper sub surfaces, salinity has decreased continuously from the beginning of March to the end of May (Figure 3c).

During MAM 2001 in R2, low salinity has been observed within the upper sub surfaces throughout the period with a gently increase in the last week of May while the high salinity (35.375 PSU) has been observed throughout March and April between 70 to 90 meter depth after that moderately increased from mid-May to end between 50 to 90 meter depth, and below 90 meter depth, salinity decreased with depth (Figure 3d). Distribution of salinity with depth during MAM 2000 in R2 (Figure 3e) has been observed more or less same as 2001 for same period with slightly lessen amount (35.350 PSU). Low salinity has been observed within upper sub surfaces of R2 during MAM and below 50 meter depth, salinity increased with depth and high salinity (35.300 PSU) has been observed between 70 to 100 meter depth in last week of May below that, salinity decreased gently with depth (Figure 3f).

CONCLUSIONS

The current research effectively illustrates the substantial modifications observed in salinity during pre-monsoon season in western Indian Ocean and eastern Indian Ocean. The highest salinity has been observed in the upper sub-surfaces of the top of the western Indian Ocean (Arabian Sea). In contrast, the lowest salinity has been observed in the upper sub-surfaces of the top of the eastern Indian Ocean (Bay of Bengal) due to the addition of fresh water in Bay of Bengal by river discharge (Rao and Shivakumar, 2003; Rao, 2015) and the contrast in salinity between Arabian Sea and Bay of Bengal decreased with depth. In the early onset year, the highest salinity was observed in R1 (near Somalia and Kenya coast) between 20 to 80 meter depth level due to a high degree of evaporation during March and mid-April, while during May, salinity decreased gradually and sifted eastward due to wind stress. During normal-onset (late onset), average (below average) salinity between 50 to 80 meter (60 to 80m) has been observed in R1 due to less evaporation and is sifted eastward also. In R2, the highest salinity has been observed between 70 to 90 meters in depth from the beginning of March to the first week of May, and then after, the region of highest salinity has been increased

to 50 to 90 meter depth. Intense evaporation during pre-monsoon season causes large amount of moisture in the atmosphere and large amount of moisture may lead the early onset over India, while in normal onset and late onset years, moisture in the atmosphere was low and wind stress transported the moist air toward the Kerala coast.

Acknowledgement

The authors acknowledge ECMWF for providing data sets for the research and the authors also acknowledge IMD for providing monsoon reports. The authors are thankful to reviewers for their valuable suggestions to improve the manuscript. The authors would like to express their gratitude towards Banaras Hindu University for providing facilities to carry research work in the form of IoE Grant (Scheme No. 6031).

Author Credit Statement

All authors contributed to the study conception and design. Data collection was performed by Dinesh K Yadav. The data analysis and plotting were done by Dinesh K Yadav and Archana Maurya. B. Mandal and Dinesh K Yadav wrote the first draft. R Bhatla supervised the work and all authors commented on previous versions of the manuscript. All authors read and approved the final manuscript.

Data Availability

The daily salinity data is available on the given link.
https://podaac.jpl.nasa.gov/dataset/ECCO_L4_TEMP_SALINITY_05DEG_DAILY_V4R4

Compliance with Ethical Standards

The authors declare that they have no conflict of interest and adhere to copy right norms.

References.

Ananthakrishnan, R. and Soman, M. K., 1988. The onset of the southwest monsoon over Kerala: 1901–1980. J. Climatol., 8(3), 283-296.

Ananthakrishnan, R., Pathan, J. M. and Aralikatti, S. S., 1983. The onset phase of the southwest monsoon. Curr. Sci., 52(16), 755-764.

Bhatla, R. and Chattopadhyay, J., 2003. Association between mid-latitude circulation and onset of Indian summer monsoon over Kerala. Mausam, 54(3), 623-630.

Bhatla, R., Ghosh, S. and Mandal, B., 2015. Performance of RegCM4.3 in **s**imulating summer monsoon onset over India using different **c**onvection schemes. Vayumandal**,** 41(1-2), 1-10.

Bhatla, R., Raju, P. V. S., Mall, R. K. and Bist, S., 2016a. Study of surface fluxes during onset of summer monsoon over India. Int. J. Climatology, 36(4), 1821-1832.

Bhatla, R., Ghosh, S., Mandal, B., Mall, R. K and Sharma, K.D., 2016b. Simulation of Indian summer monsoon onset with different parameterization convection schemes of RegCM-4.3. Atmosph. Res., 176-177, 10-18.

Bhatla, R., Singh, M. and Pattanaik, D. R., 2017. Impact of Madden-Julian oscillation on onset of summer monsoon over India. Theoretical and Appl. Climatology, 128, 381-391.

Bhatla, R., Mandal, B., Verma, S., Ghosh, S. and Mall, R. K., 2019. Performance of regional climate model in simulating monsoon onset over Indian subcontinent. Pure Appl. Geophys., 176(1), 409-420.

Fasullo, J. and Webster, P. J., 2003. A hydrological definition of Indian monsoon onset and withdrawal. J. Climate, 16(19), 3200-3211.

Gadgil, S. and Rupa Kumar, K., 2006. The Asian monsoon—agriculture and economy. The Asian Monsoon, (Edited: Wang, B.), Springer, pp. 651-683.

Goswami, B. N., Krishnamurthy, V. and Annmalai, H., 1999. A broad-scale circulation index for the interannual variability of the Indian summer monsoon. Quart. J. Royal Meteorol. Soc., 125(554), 611-633.

Krishnan, R., Sabin, T. P., Ayantika, D. C., Kitoh, A., Sugi, M., Murakami, H. et al., 2013. Will the South Asian monsoon overturning circulation stabilize any further? Climate Dynamics, 40(1-2), 187-211.

Ordoñez, P., Gallego, D., Ribera, P., Peña-Ortiz, C. and García-Herrera, R., 2016. Tracking the Indian summer monsoon onset back to the preinstrument period. J. Climate, 29(22), 8115-8127.

Raju, P.V. S., Mohanty, U. C and Bhatla, R., 2005. Onset characteristics of the southwest monsoon over India. Int. J. Climatol., 25(2), 167-182.

Raju, P. V. S., Mohanty, U. C. and Bhatla, R., 2007. Interannual variability of onset of the summer monsoon over India and its prediction. Natural Hazards, 42(2), 287-300.

Rao, R. R., 2015. Observed variability of near-surface salinity field on seasonal and interannual time scales and its impact on the evolution of sea surface temperature of the tropical Indian Ocean. Int. J. Ocean and Climate Syst., 6(2), 87-111.

Rao, R. R. and Sivakumar, R., 2003. Seasonal variability of sea surface salinity and salt budget of the mixed layer of the north Indian Ocean. J. Geophys. Res., Oceans, 108(C1), 9-1.

Roman-Stork, H. L., Subrahmanyam, B. and Murty, V. S. N., 2020. The role of salinity in the southeastern Arabian Sea in determining monsoon onset and strength. J. Geophys. Res.: Oceans, 125(1), e2019JC015592.

Skliris, N., Marsh, R., Josey, S. A., Good, S. A., Liu, C. and Allan, R. P., 2014. Salinity changes in the World Ocean since 1950 in relation to changing surface freshwater fluxes. Climate Dynamics, 43(3-4), 709-736.

Taniguchi, K., Rajan, D. and Koike, T., 2010. Effect of the variation in the lower tropospheric temperature on the wind onset of the Indian summer monsoon. Meteorol. Atmosph. Phys., 106(1-2), 75-94.

Vinayachandran, P. N., Masumoto, Y., Mikawa, T. and Yamagata, T., 1999. Intrusion of the southwest monsoon current into the Bay of Bengal. J. Geophys. Res.: Oceans, 104(C5), 11077-11085.

Wang, B., Ding, Q. and Joseph, P. V., 2009. Objective definition of the Indian summer monsoon onset. J. Climate, 22(12), 3303-3316.

Yuan, X., Salama, M. S. and Su, Z., 2018. An observational perspective of sea surface salinity in the Southwestern Indian Ocean and its role in the South Asia Summer Monsoon. Remote sensing, 10(12), 1930.

Received on: 08-08-2024; Revised on: 11-02-2025 ; Accepted on: 11-02-2025

J. Ind. Geophys. Union, 29(2) (2025), 86-100
https://doi.org/10.71122/JIGU.29(2)2025.0010

An earthquake precursor- Outgoing Longwave Radiation (OLR) observed over the Indian and Indonesian regions during high-magnitude earthquakes (M≥ 6.0)

Pooja Sharma[1], Ananna Bardhan[1*], Raj kumari[2], and D. K. Sharma[1]
[1] Department of Sciences, Manav Rachna University, Faridabad-121004, Haryana, India
[2] Department of Physics, DAV Centenary College, Faridabad-121001, Haryana, India
[*]Corresponding author: ananna@mru.edu.in

ABSTRACT

The Earth prepares itself before an earthquake and during this time, several precursory signs have been seen across the ocean, land, and atmosphere. Earthquakes inflict significant harm to both human lives and property. Therefore, monitoring and understanding the strange behaviour of various geophysical parameters as precursors, have become extremely important. The Outgoing Longwave Radiations (OLR), emitted by the surface during the recent ten high-magnitude (M ≥6.0) earthquake (EQs) events, have been examined in the present work using the Data on OLR from the NCEP website. To analyse the OLR as precursory signatures of earthquakes, the climatological analysis for the seismic precursor identification (CAPRI) methodology was carried out. An apparent change in the OLR during 2 months before the earthquake events was observed. The maximum and minimum anomalies in OLR before all ten events were analysed. The maximum and minimum anomalous increase in OLR varied from 1.16 to 1.25 and 0.71 to 1.11 times greater during the earthquake years compared to historical time series respectively, during all the ten EQ events. The study indicates a strange shift in Outgoing Longwave Radiation during periods, influenced by the seismic activity. The extent of anomalies in OLR during earthquake events is maximum over the ocean than on the land. This is because the accumulation of water vapour traps the outgoing radiation, causing an elevation in temperature over the epicentre and Earthquake Preparation Zone (EPZ)

Keywords: - Earthquake precursor, Outgoing Longwave Radiation (OLR) anomaly, Earthquake Preparation Zone (EPZ), High magnitude earthquakes, Epicentre. India and Indonesia

INTRODUCTION

Earthquakes are highly destructive natural disasters that occur without warning, making prediction crucial for impact mitigation. Despite efforts, precise prediction remains challenging due to the complexity of seismic events. The various ground, atmospheric, and ionospheric precursors have been studied over the past few decades, offering insights into potential early warning signs. These precursors range from ground deformation (Pulinets and Boyarchuk, 2004), mechanical deformation (Niu, 2008), gas emissions (Pulinets et al., 2003), electromagnetic precursors (Uyeda et al., 2009), changes in ionospheric parameters (Liu et al., 2004), and thermal anomaly (Pulinets et al., 2006; Zhang et al., 2013; Bardhan et al., 2022; Ghosh et al., 2024; Sharma et al., 2024; Qasim et al., 2024).

This work examines thermal precursors, which are temperature anomalies in the Earth's crust or near-surface environment that occur before seismic activities. Thermal anomalies have been detected in areas of earthquake preparation zones, several days prior to the seismic events (Tronin et al., 2002; Tramutoli et al., 2005) and are often attributed to thermal flux emanating from the Earth's crust in seismically active regions (Ouzounov and Freund, 2004). Several investigations about the occurrence of pre-earthquake thermal anomalies in locations like India, Japan, China, Sumatra, Italy, Iran, and Haiti, have been studied by several researchers (Tronin et al., 2002; Ouzounov and Freund, 2004; Tramutoli et al., 2005; Choudhury et al., 2006).

Schulz et al. (1997) observed latent heat anomalies associated with earthquakes, using remote sensing satellite data. In various regions of the world, efforts have been initiated to utilise thermally associated satellite observations to identify anomalous indicators connected to earthquakes, which include infrared/microwave brightness temperature (Jing et al., 2018), surface temperature (Tronin et al., 2002), air temperature (Weiyu et al., 2018), OLR (Ouzounov et al., 2007), and Surface Latent Heat Flux (SLHF) (Bardhan et al., 2022; Sharma et al., 2024). In the epicentral zones and along the faults, these anomalous thermal signals were observed for two months before significant earthquakes (Pulinets et al., 2006).

A key parameter used to describe Earth's radiation environment is the measurement of Outgoing Longwave Radiation (OLR) (Liebmann and Smith, 1996). The Earth's surface absorbs solar energy in the form of shortwave (SW) radiation. Due to the surface's low thermal conductivity, the absorbed heat doesn't penetrate deeply. Instead, it is mostly re-emitted at night as long wavelength radiation (LWR) energy. OLR which is associated with the top of the atmosphere, integrates emissions from the ground, lower atmosphere, and clouds and is primarily used for studying Earth's radiative budget and climate dynamics (Gruber and Krueger, 1984).

Several research studies have been performed related to OLR (Ouzounov et al., 2007; Rawat et al., 2011; Fu et al., 2020). Studies have revealed that abnormal thermal patterns, identified through OLR or thermal infrared radiation (TIR), frequently emerge prior to or during the earthquake preparation phase (Tramutoli et al., 2005; Pulinets et al., 2006). Rawat et al. (2011) studied earthquakes in the Indian and Italy regions and found 30-45 Wm^{-2} more energy than the normal period at the Earth's surface. Shah et al. (2019) reported significant OLR anomalies up to 21 days before major earthquakes in Pakistan

and Iran, with flux variations exceeding +2σ occurring 3 to 30 days prior. Daily OLR data have also been used to examine the variability within earthquake-prone zones (Ouzounov et al., 2007). Fu et al. (2020) identified OLR anomaly as a potential earthquake precursor, with thermal releases near the epicentre observed 2–15 days before significant events. Hameed et al. (2024) identified several atmospheric precursors potentially linked to seismic events, including variations in latent heat flux, and OLR, occurring 5–10 days before the earthquake. Tronin (2006) detected anomalies 4–20 days before a major earthquake, while Hafeez et al. (2022) identified them within a 5–10 day window. Similarly, Qasim et al. (2024) also analyzed the March 31, 2020, Mw 6.5 Idaho earthquake using high-resolution satellite data over a 45-day period. Numerous studies, including Akhoondzadeh (2024), who have reported abnormal physical and chemical precursors 1–30 days before significant seismic events. In the present work, the precursory analysis of the thermal parameter - Outgoing Longwave Radiation (OLR), is attempted on ten high-magnitude earthquakes (M≥6.0) over the Indian and Indonesian regions.

DATA AND METHODOLOGY

The Outgoing Longwave Radiation (OLR) data during the ten recent earthquakes were collected from the National Centre for Environmental Prediction/National Centre for Atmospheric Research (NCEP-NCAR) site. The data collected spanned over the Earthquake Preparation Zone (EPZ), including the epicentres of the considered earthquake events. The daily OLR data has been taken from the link: https://iridl.ldeo.columbia.edu/SOURCES/.NOAA/.NCEP/.CPC/.CBO_V1/.r0p25/.MON/.NRT/.anom. These data sets are built by integrating data from satellites with measured values from various sites throughout the world. A worldwide dataset of various climatological and surface variables is maintained by NCEP. The fluxes considered in functional meteorological forecasting techniques contain in-situ data. The NCEP-NCAR (National Centers for Environmental Prediction/National Center for Atmospheric Research) integrates the data from remote sensing, aircraft, pibal, rawinsonde, ship, ground instruments etc, thus, provides assimilated global reanalysis data with an accuracy limit of 10-30 W/m^2 (Zhang et al., 2013). The daily OLR values have a spatial resolution of 1.87×1.90 degrees across the globe from 1 Jan 1948 to the current time respectively. The earthquake details presented in Table 1 are sourced from the United States Geological Survey (USGS) (http://earthquake.usgs.gov/activity/world.html) website. This table includes information on event locations, dates, times, epicentre coordinates, and focal depths for earthquakes in Pariaman, Biak, Papua, Gorontalo, Assam, Port Blair, Ternate, Bengkulu and Luwuk.

DATA SELECTION AND ANALYSIS FOR OUTGOING LONGWAVE RADIATION

To investigate the anomalies observed in OLR before all ten earthquakes, the statistical method - Climatological Analysis for Seismic Precursor Identification (CAPRI) are applied. This section provides a concise overview of the mathematical algorithm employed by the CAPRI method. For a more comprehensive understanding, readers can refer to the detailed discussions in Piscini et al. (2017, 2019). Dobrovolsky et al. (1979) proposed an observable association between the expected circular area of mechanical, thermal, and electromagnetic activity prior to them and the estimated magnitude of the upcoming earthquake. Since seismic precursors typically form across vast regions surrounding impending faults, $r = 10^{0.43M}$. where M is the anticipated earthquake's magnitude and r is the “strain radius,” which is the affected area's radius in kilometres. The earthquake preparation zone (EPZ) is determined using $r = 10^{0.43M}$. Over the EPZ, outgoing longwave radiation anomalies have been investigated.

The Climatological Analysis for Seismic Precursor Identification (CAPRI) method is employed to identify anomalies in climatological variable time series through statistical analysis. In this study, the focus is on the OLR parameter. Before analysis, the data is spatially averaged over the epicentral region. OLR(d)y denotes the average OLR value for a specific day 'd' (equivalent to 2 months or 60 days) in a given year ‘y’ (spanning a dataset of 38 years). The CAPRI methodology is designed to remove long-term trends that may exist in the day-to-day dataset. Its methodology is primarily proposed to minimize probable "global warming".

To effectively eliminate these trends, as detailed in studies by Piscini et al. (2017, 2019), a 38-year dataset is analyzed by considering individual time sequences corresponding to the same day. For each day of the year across the entire time span, a linear regression analysis is performed on the variables under examination. The slope of this fit, denoted as m (d) that representing the OLR variation on the same day ‘d’ for each year, is then utilized to remove the long-term variations in the variable. A linear fit is a good trend given the short time span analysed (about 40 years) in relation to climate change (Brohan et al., 2006).

In this process, the initial year in the time-series data, denoted as y_o, serves as a "reference point." The growth or change in the variable is determined by multiplying the slope obtained from the linear fit by the number of successive years following the first year. This correction is applied to eliminate the long-term trends for the subsequent years in the dataset.

$$OLR'(d)_y = OLR(d)_y - m(d) \times (y - y_o) \quad \text{----} \quad (1)$$

This method is carried out for each of the days being considered. The advantage of performing a new fit for each day lies in its ability to account for the potential influence of localized seasonal variations over time, as discussed in Piscini et al. (2017, 2019). For each year under examination, the resulting data consists of daily spatially averaged Outgoing Longwave Radiation (OLR) values, organized day by day. It's important to note that, irrespective of the fact that the year did not conform to the estimates of the consistent pattern, any detected pattern was also removed from that specific year. Subsequently, the variables from the time-series data are aggregated across all years, focusing on each day 'd'. This aggregation provides the historical mean, denoted as $OLR_h(d)$ (where 'h' signifies the historical time series), spanning the previous 37 years, as the year of the earthquake series is excluded from this calculation:

$$OLR_h(d) = \frac{1}{N_y} \sum_{y=\alpha}^{\beta} OLR'(d)_y \quad \text{----} \quad (2)$$

Here, N_y represents the total number of years that have been aggregated, where α is the initial year and β is the 37th year. In this context, the program also calculates the standard deviation (σ) for each day. The behaviour factor of the subsequent year, denoted as 'ỹ,' is subsequently compared to the historical series as described in Eq. (1). To facilitate this comparison, we set the overall average in the studied period to correspond with the average of the historical time series to make this comparison possible:

$$OLR(d)_{\tilde{y}} = OLR'(d)_{\tilde{y}} - [(OLR'_{\tilde{y}})_d - (OLR_h)_d] \quad \text{----} \quad (3)$$

In the current study, it's important to account for the possibility of a single year deviating significantly from the historical average, which could potentially introduce false results. Therefore, the equation mentioned above is employed to effectively filter out these short-term anomalies. Specifically, in this study, anomalous days are identified as those where the variable's values deviate by at least 2σ above or below the historical average.

RESULTS

In this study, we have examined ten recent high-magnitude (M ≥ 6.0) earthquakes that occurred between years 2015 and 2022. In all these events, the behaviour of OLR as a precursor of earthquakes has been analysed. The details of all the earthquake events are taken from the website of the National Earthquake Information Centre (NEIC), and United States Geological Survey (USGS), which includes location, date and time, epicentre, magnitude, and focal depth (Table 1).

Variation of OLR during the earthquake events

1. Pariaman (Indonesia)

This earthquake occurred in Pariaman, Indonesia (Epicentre: 1.14° S and 98.65° E) on September 10, 2022, and had a magnitude of 6.0 and a focal depth of 20.0 km. The variation in OLR has been analysed for the purpose of identifying precursory signatures during the earthquake event. (Figure 1) shows a comparison of the time series year 2022 (earthquake year) with the historical time series years 1985-2021 of OLR. In (Figure 1),the black curve with a cross and the red curve with a triangle denotes the earthquake year and a historical time series of 37 years, respectively. The coloured curve represents 2.0 (blue) standard deviations from the mean historical time series, respectively. In analysis, we examined OLR values for 59 days leading up to an earthquake event, with the 60th day representing the day of the earthquake (purple line). We have considered the variation of OLR as an anomaly only when its value is above 2 standard deviations from the historical time series. (Figure 1**)** reveals numerous instances where the OLR exceeds the values found in the historical time series.

Table1. Details of the studied earthquakes and their magnitude and focal depth

Sr. No.	Location	Date and time (UTC)	Epicentre (Geog. Lat., Geog. Long.)	Magnitude	Focal depth (km)
1	Pariaman, Indonesia	10.09.2022 (23:10:43)	1.14° S, 98.65° E	6.0	20
2	Biak, Indonesia	10.09.2022 (00:05:12)	2.23° S, 138.17° E	6.2	21
3	Papua, Indonesia	09.09.2022 (23:31:47)	2.24° S, 138.19° E	6.2	18
4	Pariaman, Indonesia	13.03.2022 (21:09:22)	0.62° S, 98.62° E	6.7	28
5	Gorontalo, Indonesia	06.11.2021 (14:37:36)	0.04° S, 124.28° E	6.0	34
6	Dhekiajuli, Assam, India	28.04.2021 (02:21:26)	26.78° N, 92.45° E	6.0	34
7	Port Blair, India	17.07.2020 (14:03:40)	11.84° N, 94.93° E	6.1	10
8	Ternate, Indonesia	14.11.2019 (21:12:54)	1.53° N,126.41° E	6.0	23
9	Bengkulu, Indonesia	13.08.2017 (03:08:10)	3.76° S, 101.62° E	6.4	31
10	Luwuk, Indonesia	15.03.2015 (23:17:16)	0.54° S, 122.30° E	6.1	31

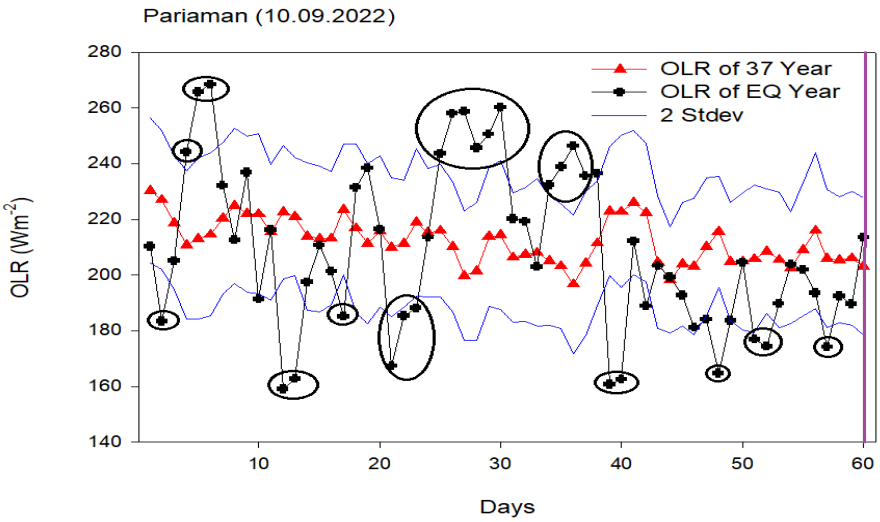

Figure 1. Daily variation of outgoing longwave radiation during the earthquake year (black cross) - 2022 vs. mean historical time series 1985-2021 (red triangle) during the earthquake events that occurred in Pariaman, Indonesia (10.09.2022) having epicentre (1.14° S, 98.65° E). The blue coloured curve indicates 2.0 standard deviation from the mean - historical time series. The purple line shows earthquake day.

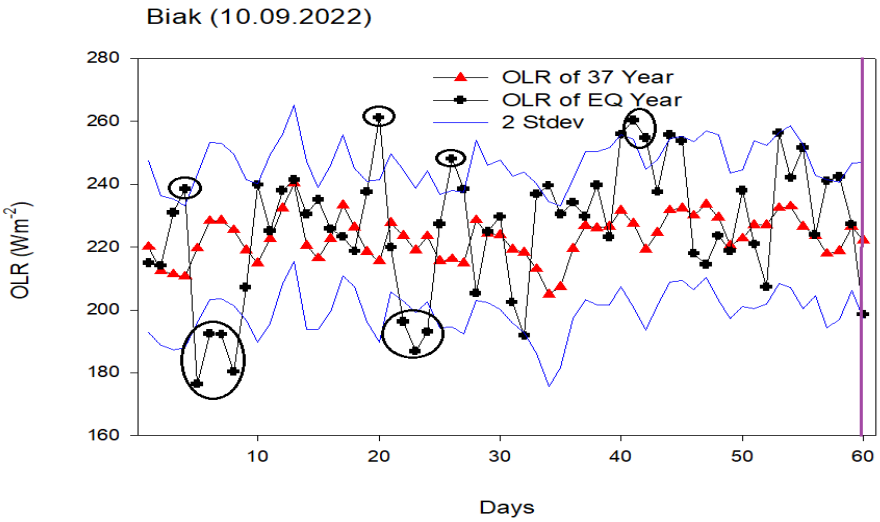

Figure 2. Daily variation of outgoing longwave radiation during the earthquake year (black cross) - 2022 vs. mean historical time series 1985-2021 (red triangle) during the earthquake events that occurred in Biak, Indonesia (10.09.2022) having epicentre (2.23° S, 138.17° E). The blue coloured curve indicates a 2.0 standard deviation from the mean - historical time series. The purple line shows earthquake day.

During the earthquake year, there is an increase in the OLR on the 2nd, 12th -13th, 17th, 39th -40th, 48th, 51st -52nd and 57th, days with the values 183.37 Wm^{-2}, 160.91 Wm^{-2}, 185.12 Wm^{-2}, 161.65 Wm^{-2}, 164.69 Wm^{-2}, 175.64 Wm^{-2}, and 174.14 Wm^{-2}, respectively, greater than 2σ from the mean historical time series. Again, it was observed that OLR values exhibited an increase during several periods: from the 4th to the 6th days, the 21st to the 23rd day, the 25th to the 30th days, and from the 34th to the 37th days with the average OLR values during the earthquake year and historical time series were ∽259.40 Wm^{-2}, ∽180.26 Wm^{-2}, ∽252.76 Wm^{-2}, ∽238.23 Wm^{-2}, and ∽212.77 Wm^{-2}, ∽213.33 Wm^{-2}, ∽210.73 Wm^{-2}, ∽202.29 Wm^{-2}, respectively. The analysis distinctly shows that the maximum OLR anomalies, serving as precursory signatures, occur in the period leading up to the earthquake day.

2. Biak (Indonesia)

The earthquake that occurred on September 10, 2022, had a magnitude of 6.2 and a focal depth of 21.0 km (epicentre 2.23° S and 138.17° E) in Biak, Indonesia. (Figure 2**)** shows a comparison of the time series year 2022 (earthquake year) with the historical time series years 1985–2021 of OLR. The 37-year historical time series and the earthquake year are indicated in (Figure 2) by the red curve with a triangle and the black curve with a cross, respectively. (Figure 2) shows many instances in which the OLR exceeds the historical time series. There is an

increase in the OLR on the 4th, 20th, 26th, 41st – 42nd, and 44th days with a value ~238.45 Wm^{-2}, ~261.17 Wm^{-2}, ~248.03 Wm^{-2}, ~257.91 Wm^{-2}, and ~255.67 Wm^{-2}, respectively, of greater than 2σ from the mean historical time series. Again, it was found that the OLR values increased from the 5th to 8th days, and from the 22nd to 24th days, with the average OLR values during the earthquake year and historical time series being ~185.33 Wm^{-2}, ~192.03 Wm^{-2} and ~225.42 Wm^{-2}, ~222.02 Wm^{-2} respectively. Several days show the anomalous behaviour of OLR during the pre-earthquake period. It is clear that from (Figure 2**)** before the earthquake day, the highest numbers of anomalies in OLR as precursory signatures are observed.

3. Papua (Indonesia)

The next earthquake event occurred on September 09, 2022, with a magnitude of 6.2 (epicentre: 2.24° S, 138.19° E) and a focal depth of 18.0 km in Papua, Indonesia. (Figure 3) shows a comparison of the time series year 2022 (earthquake year) with the historical time series years 1985–2021 of OLR. (Figure 3) shows many instances in which the OLR exceeds the 2σ from the mean historical time series. On several days, the increase in the OLR values on the 5th, 21st, 27th, 35th, 42nd - 43rd and 45th days with values ~238.45 Wm^{-2}, ~261.17 Wm^{-2}, ~248.03 Wm^{-2}, ~239.58 Wm^{-2}, ~257.55 Wm^{-2} and ~255.67 Wm^{-2}, respectively, greater than 2σ from the mean historical time series. Again, it was found that the OLR values rise from the 6th to 9th days, and from the 23rd to 25th days, with the average OLR values during the earthquake year and historical time series being ~185.33 Wm^{-2}, ~192.03 Wm^{-2} and ~225.44 Wm^{-2}, ~222.02 Wm^{-2} respectively. Several days show the anomalous behaviour of OLR during the pre-earthquake period. It is clearly observed that the maximum anomalies in OLR as precursory signatures are mostly observed before the earthquake day.

4. Pariaman (Indonesia)

The earthquake that occurred on March 13, 2022, had a magnitude of 6.7 and a focal depth of 28.0 km (epicentre: 0.62° S and 98.62° E) in Pariaman, Indonesia. (Figure 4) shows a comparison of the time series year 2022 (earthquake year) with the historical time series years 1985–2021 of OLR. The 37-year historical time series and the earthquake year are indicated in (Figure 4) by the red line with a triangle and the black line with a cross, respectively. (Figure 4) shows many instances in which the OLR exceeds the historical time series. There is an increase in the OLR on the 14th, 16th, 28th to 29th, 52nd to 53rd and 56th days with values ~231.66 Wm^{-2}, ~245.65 Wm^{-2}, ~167.31 Wm^{-2}, ~190.51 Wm^{-2}, and ~197.21 Wm^{-2}, respectively, greater than 2σ from the mean historical time series. Again, it was found that the OLR values rise from the 1st to 4th days, 8th to 10th days, and from the 23rd to 25th days, with the average OLR values during the earthquake year and historical time series being ~240.07 Wm^{-2}, ~233.46 Wm^{-2}, ~179.13 Wm^{-2}, and ~205.54 Wm^{-2}, ~195.6 Wm^{-2}, ~222.11 Wm^{-2} respectively. It is clear that from (Figure 4) several days before the earthquake day, the highest numbers of anomalies in OLR as precursory signatures are observed.

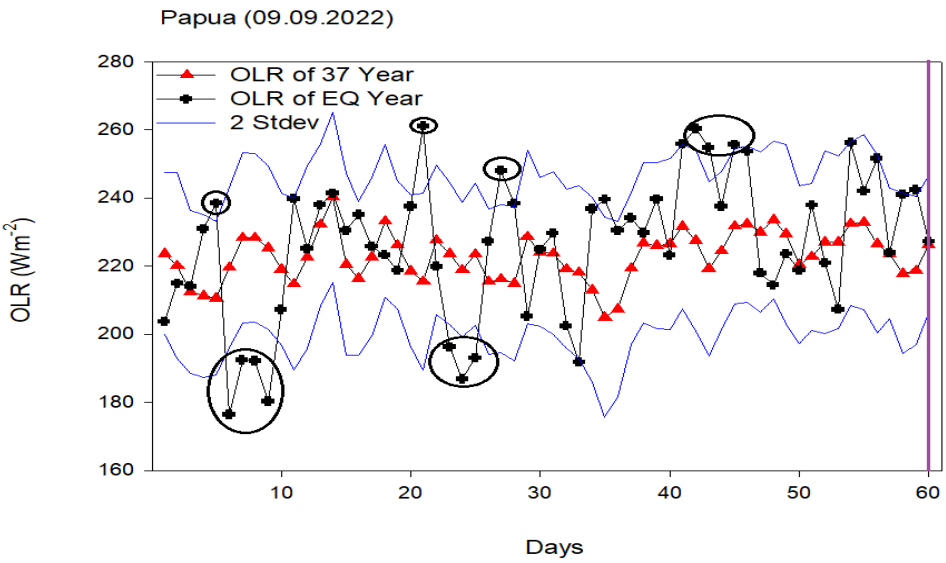

Figure 3. Daily variation of outgoing longwave radiation during the earthquake year (black cross) - 2022 vs. mean historical time series 1985-2021 (red triangle) during the earthquake events that occurred in Papua, Indonesia (09.09.2022) having epicentre (2.24° S, 138.19° E). Blue coloured curve indicates 2.0 standard deviation from the mean - historical time series. The purple line shows earthquake day.

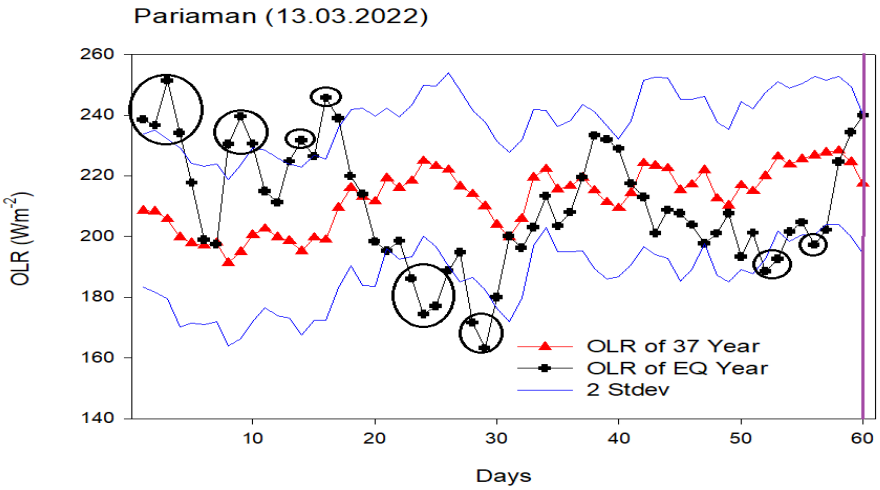

Figure 4. Daily variation of outgoing longwave radiation during the earthquake year (black cross) - 2022 vs. mean historical time series 1985-2021 (red triangle) during the earthquake events that occurred in Pariaman, Indonesia (13.03.2022) having epicentre (0.62° S, 98.62° E). Blue coloured curve indicates 2.0 standard deviation from the mean - historical time series. The purple line shows earthquake day.

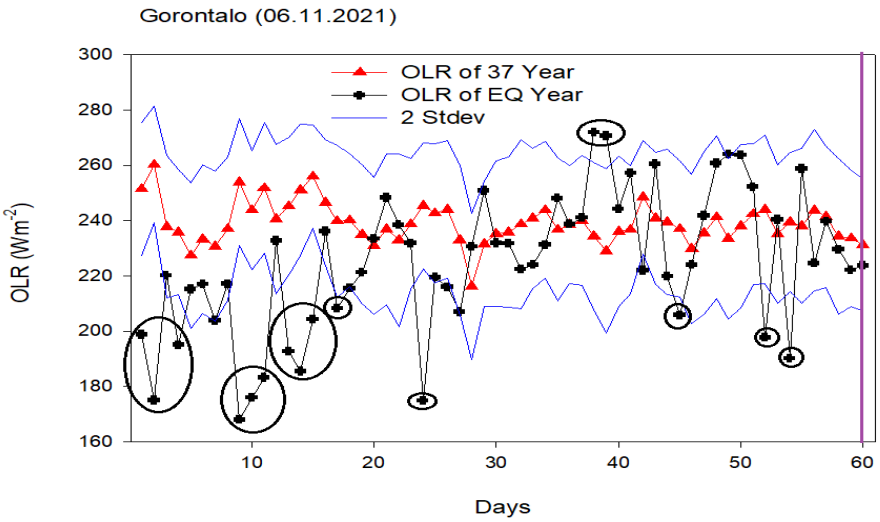

Figure 5. Daily variation of outgoing longwave radiation during the earthquake year (black cross) - 2021 vs. mean historical time series 1984-2020 (red triangle) during the earthquake events that occurred in Gorontalo, Indonesia (06.11.2021) having epicentre (0.04° S, 124.28° E). Blue coloured curve indicates 2.0 standard deviation from the mean - historical time series. The purple line shows earthquake day.

5. Gorontalo (Indonesia)

The next earthquake event occurred on Nov 6, 2021, with a magnitude of 6.0 (epicentre 0.04° S, 124.28° E) and a focal depth of 34.0 km in Gorontalo, Indonesia. (Figure 5) shows a comparison of the time series 2021 (earthquake year) with the historical time series 1984–2020 of OLR. (Figure 5 shows many instances in which the OLR exceeds the 2σ from the mean historical time series. From (Figure 5), one can observe many instances where the OLR is higher than the historical time series. There is an increase in the OLR on the 1st- 2nd, 4th, 17th, 24th, 38th -39th, 45th, 52nd and 54th, days with values ~186.93 Wm^{-2}, ~195.02 Wm^{-2}, ~208.26 Wm^{-2}, ~174.87 Wm^{-2}, ~271.31 Wm^{-2} , ~205.81 Wm^{-2}, ~197.75 Wm^{-2} and ~190.17 Wm^{-2}, respectively, of greater than 2σ from the mean historical time series. It was found that the OLR values rise from the 9th to 11th days, and from the 13th to 15th days, with the average OLR values during the earthquake year and historical time series being ~175.74 Wm^{-2}, ~194.16 Wm^{-2}, and ~249.83 Wm^{-2}, ~250.80 Wm^{-2} respectively. It is clearly observed that the maximum number of anomalies in OLR as precursory signatures are present before the earthquake day.

6. Dhekiajuli (Assam)

The next earthquake considered was Dhekiajuli, Assam (India), that occurred on April 28, 2021, with a magnitude of 6.0 having epicentre: 26.78° N, 92.45° E and focal depth, 34.0 km. (Figure 6) shows a comparison of the time series 2021 (earthquake year) with the historical time series years 1984–2020 of OLR. From this figure, one can observe many

instances where the OLR is higher than the historical time series. The variation in the OLR on 38th-39th,42nd, 44th, 46th, 48th, and 52nd days with values ~259.95 Wm^{-2}, ~250.22 Wm^{-2}, ~256.29 Wm^{-2}, ~258.49 Wm^{-2}, ~212.28 Wm^{-2}, and ~260.25 Wm^{-2}, respectively, greater than 2σ from the mean historical time series. Again, it was found that the OLR values rise from the 1st to 4th, 10th to 14th, 16th to 19th, 23rd to 28th, 33rd to 35th, and 55th to 60th days, with the average OLR values during the earthquake year and historical time series being ~257.64 Wm^{-2}, ~254.84 Wm^{-2}, ~262.72 Wm^{-2}, ~261.35 Wm^{-2}, ~254.71 Wm^{-2}, ~258.22 Wm^{-2} and ~237.09 Wm^{-2}, ~230.11 Wm^{-2}, ~240.92 Wm^{-2}, ~225.98 Wm^{-2}, ~233.82 Wm^{-2}, ~218.35 Wm^{-2}, respectively.

7. Port Blair (India)

The earthquake occurred on July 17, 2020, having magnitude 6.1, epicentre 11.84° N, 94.93° E and focal depth 10.0 km in Port Blair, India. (Figure 7) shows a comparison of the time series 2020 (earthquake year) with the historical time series years 1983–2019 of OLR. In Figure 7, the black curve with a cross and the red curve with a triangle denote the earthquake year and a historical time series of 37 years, respectively. Initially, OLR is greater than 2σ on the 24th, 37th, 55th-56th, and 60th days with values ~215.03 Wm^{-2}, ~242.89 Wm^{-2}, ~145.09 Wm^{-2}, and ~222.04 Wm^{-2}, respectively, from the mean historical time series. Several times during the two months preceding the earthquake, the OLR was greater than two standard deviations. However, the frequency of the aforementioned events is greatest on 14th-16th, and 28th to 30th day, with the average OLR values during the earthquake year and historical time series of ~220.86 Wm^{-2}, ~166.89 Wm^{-2} and ~191.83 Wm^{-2}, ~203.63 Wm^{-2}, respectively. It is clear to see that days from the earthquake day, the highest numbers of anomalies in OLR as observed precursory signatures

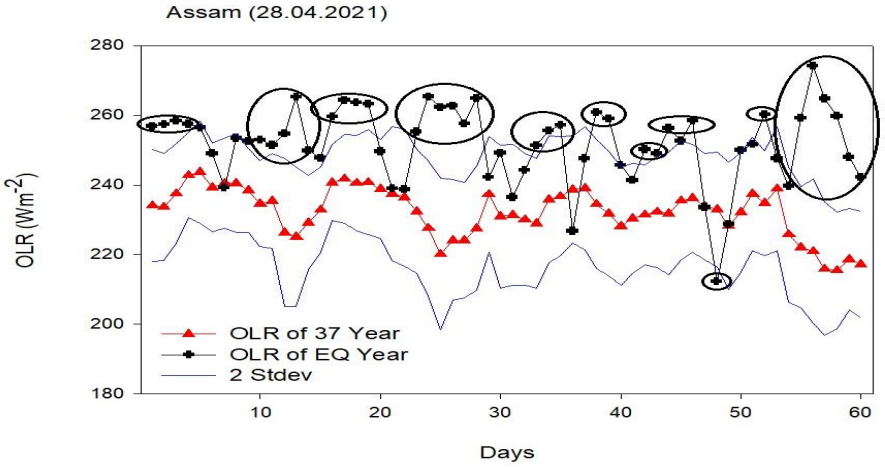

Figure 6. Daily variation of outgoing longwave radiation during the earthquake year (black cross) - 2021 vs. mean historical time series 1984-2020 (red triangle) during the earthquake events that occurred in Dhekiajuli, Assam, India (28.04.2021) having epicentre (26.78° N, 92.45° E). Blue coloured curve indicates 2.0 (blue) standard deviation from the mean - historical time series. The purple line shows earthquake day.

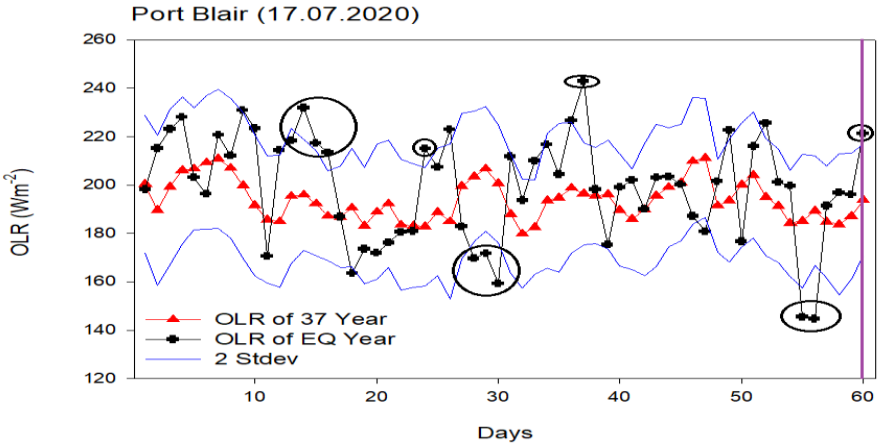

Figure 7. Daily variation of outgoing longwave radiation during the earthquake year (black cross) - 2020 vs. mean historical time series 1983-2019 (red triangle) during the earthquake events that occurred in Port Blair, India (17.07.2020), having epicentre 11.84° N, 94.93° E. Blue coloured curve indicates 2.0 standard deviation from the mean - historical time series. The purple line shows earthquake day.

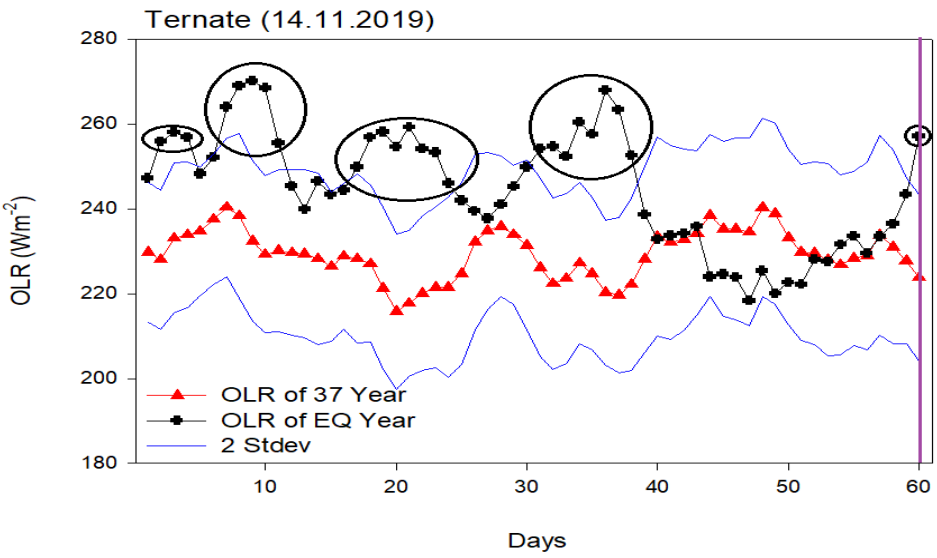

Figure 8. Daily variation of outgoing longwave radiation during the earthquake year (black cross) - 2019 vs. mean historical time series 1982-2018 (red triangle) during the earthquake events that occurred in Ternate, Indonesia on 14.11.2019 having epicentre 1.53° N, 126.41° E. Blue coloured curve indicates 2.0 standard deviation from the mean - historical time series. The purple line shows earthquake day.

8. Ternate (Indonesia)

On November 14, 2019, a magnitude 6.0 (epicentre 1.53° N, 126.41° E) earthquake occurred in Ternate, Indonesia, at a focal depth of 23 km. (Figure 8) shows the comparison between the time series 2019 (earthquake year) with the historical years 1982-2018 time series. The black line with a cross and the red line with a triangle denote the earthquake year and a historical time series of 37 years, respectively. The figure shows that OLR is greater than 2σ on the 2nd to 4th, 7th to 11th, 17th to 24th, 31st to 38th, and 60th day, with the average OLR values during the earthquake year and historical time series being ~256.87 Wm^{-2}, ~265.36 Wm^{-2}, ~254.59 Wm^{-2}, ~257.83 Wm^{-2}, ~257.22 Wm^{-2}, and ~231.66 Wm^{-2}, ~234.07 Wm^{-2}, ~221.62 Wm^{-2}, ~223.25 Wm^{-2}, ~223.94 Wm^{-2} respectively.

9. Bengkulu (Indonesia)

The earthquake that occurred on August 13, 2017, had a magnitude of 6.4 and a focal depth of 31.0 km (epicentre 3.76° S and 101.62° E) in Bengkulu, Indonesia. The variation in OLR has been analysed for the purpose of identifying precursory signatures during the earthquake event. (Figure 9) shows a comparison of the time series year 2017 (earthquake year) with the historical time series years 1980–2016 of OLR. From this figure, one can observe many instances where the OLR is higher than the historical time series. There is an increase in the OLR on the 4th, 9th to 10th, 12th to 13th, 15th and 23rd, days with values ~204.82 Wm^{-2}, ~209.66 Wm^{-2}, ~200.23 Wm^{-2}, ~212.82 Wm^{-2}, and ~212.97 Wm^{-2}, respectively, of greater than 2σ from the mean historical time series. Again, it was found that the OLR values rise from the 28th to 31st days, 38th to 42nd days, and from the 48th to 50th days, with the average OLR values during the earthquake year and historical time series being ~210.04 Wm^{-2}, ~263.61 Wm^{-2}, ~264.99 Wm^{-2}, and ~243.68 Wm^{-2}, ~230.92 Wm^{-2}, ~228.38 Wm^{-2}, respectively. It is clearly observed that the maximum number of anomalies in OLR as precursory signatures are present before the earthquake day.

10. Luwuk (Indonesia)

The next earthquake event occurred on March 15, 2015, with a magnitude of 6.1 (epicentre 0.54° S, 122.30° E) and a focal depth of 31.0 km in Luwuk, Indonesia. (Figure 10) shows a comparison of the time series 2015 (earthquake year) with the historical time series 1978–2014 of OLR. (Figure 10) shows many instances in which the OLR exceeds the 2σ from the mean historical time series. From (Figure 10), one can observe many instances where the OLR is higher than the historical time series. There is an increase in the OLR on the 13th and 53rd, days with values ~232.46 Wm^{-2} and ~247.73 Wm^{-2}, respectively, of greater than 2σ from the mean historical time series. Again, it was found that the OLR values rise from the 36th to 38th days, and from the 47th to 50th days, with the average OLR values during the earthquake year and historical time series being ~171.19 Wm^{-2}, ~182.25 Wm^{-2} and ~217.10 Wm^{-2}, ~228.40 Wm^{-2} respectively. It is observed that the maximum number of anomalies in OLR as precursory signatures are present before the earthquake day.

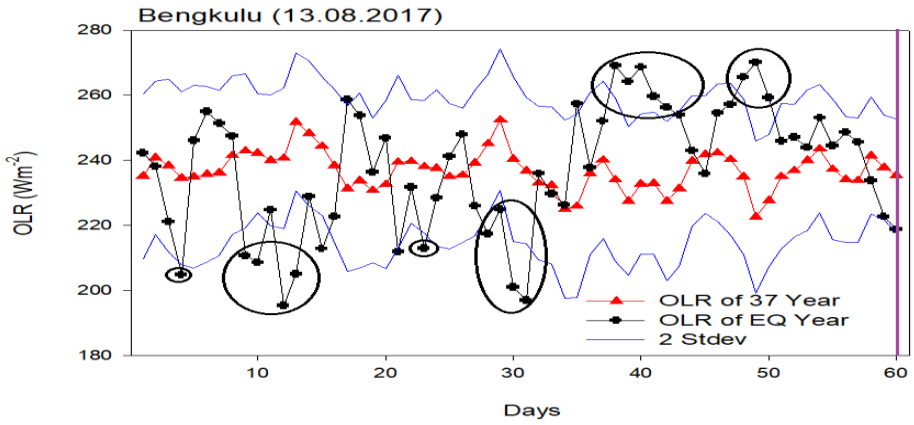

Figure 9. Daily variation of outgoing longwave radiation during the earthquake year (black cross) - 2017 vs. mean historical time series 1980-2016 (red triangle) during the earthquake events that occurred in Bengkulu, Indonesia (13.08.2017) having epicentre 3.76° S, 101.62° E. Coloured curve indicates 2.0 (blue) standard deviation from the mean - historical time series. The purple line shows earthquake day.

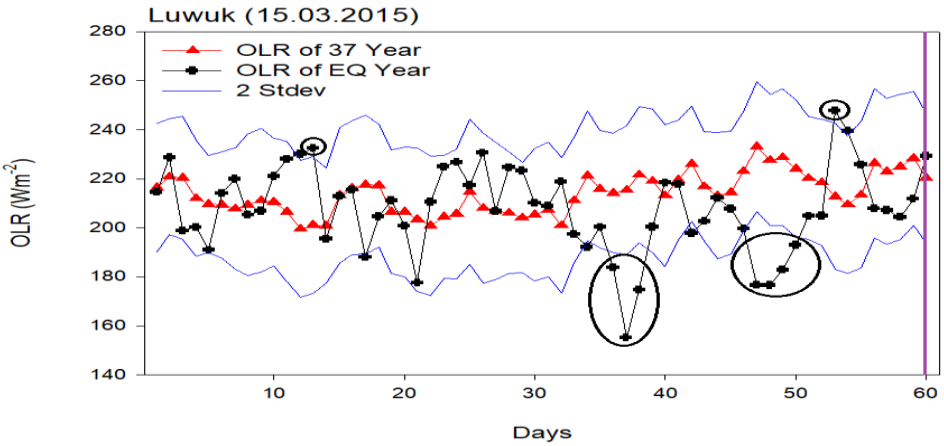

Figure 10. Daily variation of outgoing longwave radiation during the earthquake year (black cross) - 2015 vs. mean historical time series 1978-2014 (red triangle) during the earthquake events that occurred in Luwuk, Indonesia (15.03.2015) having epicentre 0.54° S, 122.30° E. Blue coloured curve indicates 2.0 standard deviation from the mean - historical time series. The purple line shows earthquake day.

Maximum and minimum anomalies in OLR during the earthquake events

One can see from the figures that the OLR exhibited anomalous behaviour during all the earthquake occurrences. The anomaly can be used to identify some of the major warning signs of upcoming earthquakes. Use of the OLR anomaly, will help us better comprehend various earthquake parameters. In the present investigation, we have additionally examined the maximum and minimum OLR anomalies experienced during each earthquake occurrences.

(Table 2A) provides the details of the maximum anomaly in OLR during all the earthquake events. Parameter *D* represents the day when the maximum anomaly in OLR during the EQ year was observed, compared to the historical time series. *X* and *Y* represent the magnitude values of OLR corresponding to that day *(D)* during the EQ year and historical time series respectively. *X/Y* gives the extent of maximum anomaly of OLR during EQ year compared to the historical time series corresponding to day *D*.

The Earthquake that occurred on 10.09.2022 (Pariaman, Indonesia) experienced the highest anomaly on the 6th day before the earthquake day. The corresponding values of OLR during the earthquake year and historical time series were 268.42 Wm^{-2} and 214.54 Wm^{-2} respectively. Thus, the magnitude of the anomaly was registered as 1.25 times greater than the historical series. On 10.09.2022 (Biak, Indonesia) an earthquake occurred with 6.2 magnitude. The highest anomaly was recorded on the 20th day with a magnitude value of OLR 261.17

Table 2A. Details of the maximum observed anomaly in OLR during the earthquake events

Sr. No.	Location	Date and time(UTC)	Epicentre (Lat., Long.)	Maximum anomaly day (D)	Value of OLR during earthquake Year (*X*)	Value of OLR corresponding day of historical time series (*Y*)	*X/Y*
1	Pariaman, Indonesia	10.09.2022 (23:10:43)	1.14° S, 98.65° E	55th	268.42	214.54	1.25
2	Biak, Indonesia	10.09.2022 (00:05:12)	2.23° S, 138.17° E	41st	261.17	215.51	1.21
3	Papua, Indonesia	09.09.2022 (23:31:47)	2.24° S, 138.19° E	40th	261.17	215.51	1.21
4	Pariaman, Indonesia	13.03.2022 (21:09:22)	0.62° S, 98.62° E	58th	251.35	205.69	1.22
5	Gorontalo, Indonesia	06.11.2021 (14:37:36)	0.04° S, 124.28° E	23rd	271.97	234.35	1.16
6	Dhekiajuli, Assam, India	28.04.2021 (02:21:26)	26.78° N, 92.45° E	5th	274.16	220.95	1.24
7	Port Blair, India	17.07.2020 (14:03:40)	11.84° N, 94.93° E	24th	242.89	196.32	1.23
8	Ternate, Indonesia	14.11.2019 (21:12:54)	1.53° N,126.41° E	52nd	270.09	232.33	1.16
9	Bengkulu, Indonesia	13.08.2017 (03:08:10)	3.76° S, 101.62° E	12th	270.16	222.64	1.21
10	Luwuk, Indonesia	15.03.2015 (23:17:16)	0.54° S, 122.30° E	7th	247.73	212.75	1.16

Table 2B. Details of minimum observed anomaly in OLR during the earthquake events

Sr. No.	Location	Date and Time (UTC)	Epicentre (Lat., Long.)	Minimum anomaly day (*D′*)	Value of OLR during earthquake year (*X′*)	Value of OLR corresponding day of historical time series (*Y′*)	*X′/Y′*
1	Pariaman, Indonesia	10.09.2022 (23:10:43)	1.14° S, 98.65° E	49th	159.03	222.57	0.71
2	Biak, Indonesia	10.09.2022 (00:05:12)	2.23° S, 138.17° E	56th	176.40	219.63	0.80
3	Papua, Indonesia	09.09.2022 (23:31:47)	2.24° S, 138.19° E	55th	176.40	219.63	0.80
4	Pariaman, Indonesia	13.03.2022 (21:09:22)	0.62° S, 98.62° E	32nd	163.12	209.98	0.77
5	Gorontalo, Indonesia	06.11.2021 (14:37:36)	0.04° S, 124.28° E	52nd	168.01	253.91	0.66
6	Dhekiajuli,Assam, India	28.04.2021 (02:21:26)	26.78° N, 92.45° E	13th	212.28	233.01	0.91
7	Port Blair, India	17.07.2020 (14:03:40)	11.84° N, 94.93° E	5th	144.72	189.30	0.76
8	Ternate, Indonesia	14.11.2019 (21:12:54)	1.53° N,126.41° E	37th	245.95	221.49	1.11
9	Bengkulu, Indonesia	13.08.2017 (03:08:10)	3.76° S, 101.62° E	49th	195.38	240.74	0.81
10	Luwuk, Indonesia	15.03.2015 (23:17:16)	0.54° S, 122.30° E	24th	155.13	215.43	0.72

Wm^{-2} and 215.51 Wm^{-2} during the earthquake year and historical time series respectively. Thus, a 1.21 times increase in the anomaly was observed. Similarly, all the events in consideration experienced anomalies. The maximum anomaly in OLR was 1.21, 1.22, 1.16, 1.24, 1.23, 1.16, 1.21, 1.16 times greater during the earthquake year compared to the historical time series during 3rd, 4th, 5th, 6th, 7th, 8th, 9th and 10th earthquake events in consideration respectively. The highest

anomalies spanned from 1.16 to 1.25 times greater than the historical time series. The details of all the magnitude values of the highest anomaly OLR during EQ year and historical time series events have been summarised in Table 2A.

Similarly, Table 2B provides the details of the minimum anomaly in OLR during all the earthquake events. Parameter *D′* represents the day when the maximum anomaly in OLR during the earthquake year was observed compared to the historical time series. *X′* and *Y′* represent the magnitude values of OLR corresponding to that day *(D′)* during the earthquake year and historical time series respectively. *X′/Y′* gives the extent of the minimum anomaly of OLR during earthquake year compared to the historical time series corresponding to day *D′*.

The first earthquake event under consideration (10.09.2022; Pariaman, Indonesia) observed the minimum anomaly on the 12th day before the EQ day. During this event, the minimum anomaly observed in OLR during the earthquake year and in the historical time series were 159.03 Wm^{-2} and 222.57 Wm^{-2}, respectively. Thus, resulting in anomalous increase of 0.71 times greater than the historical series. Another earthquake that occurred on September 10, 2022, in Biak, Indonesia, experienced the minimum anomaly in OLR on the 5th day, with values of 176.40 Wm^{-2} during the earthquake year and 219.63 Wm^{-2} in the historical time series respectively. Thus, experiencing an anomalous increase of 0.80 times, compared to historical data. Similar observations were recorded during all the other earthquake events. The minimum anomalous increase in OLR were 0.80, 0.77, 0.66, 0.91, 0.76, 1.11, and 0.81 times greater during the earthquake years, compared to the historical time series during 3rd, 4th, 5th, 6th, 7th, 8th, 9th, and 10th earthquake events in consideration respectively. The minimum anomalies ranged from 0.66 to 1.11 times greater than the values in the historical time series.

(Table 2C and Figure 11) provide a comprehensive overview of the maximum and minimum anomalous increase of OLR during all the EQs. The observed maximum and minimum anomalous increase in OLR spanned from 1.16 to 1.25 and 0.66 to 1.11 times greater during the earthquake years respectively, compared to historical time series during all the ten EQ events. **(**Table 1) lists the locations of all earthquake occurrences. All the earthquakes under consideration had distinctive origins; four of their epicentres were on land, while others were located close to or in the ocean. The OLR anomalies before earthquakes with a magnitude greater than 6.0 that occurred in India and the Indonesian regions have been examined. Outgoing longwave radiation (OLR) refers to infrared radiation continuously emitted from the Earth's surface and subsequently released into the atmosphere. This radiation is measured as the amount of energy emitted per unit area. Before the occurrence of recent highly destructive earthquakes, instances were noted where anomalous positive deviations above the 2σ level were observed two months prior to the earthquake events. For example, Japan (M 9.0, 2011) (Pulinets and Ouzounov, 2011), Sumatra (M 8.2, 2012) (Venkatanathan et al., 2013), and Pakistan (M 7.7, 2013) (Venkatanathan and Natyaganov, 2014) are the cases where strange variation in OLR have been recorded before significant earthquakes. These anomalies appeared at different times and were probably influenced by unusual features of tectonic activity, such as earthquakes, and plate movements, which can significantly influence surface and atmospheric conditions, leading to variations and anomalies in outgoing longwave radiation.

Table 2C. Maximum/minimum anomaly in OLR during all the earthquake events

Sr. No.	Location	Date and time(UTC)	*X/Y*	*X′/Y′*
1	Pariaman, Indonesia	10.09.2022 (23:10:43)	1.25	0.71
2	Biak, Indonesia	10.09.2022 (00:05:12)	1.21	0.80
3	Papua, Indonesia	09.09.2022 (23:31:47)	1.21	0.80
4	Pariaman, Indonesia	13.03.2022 (21:09:22)	1.22	0.77
5	Gorontalo, Indonesia	06.11.2021 (14:37:36)	1.16	0.66
6	Dhekiajuli,Assam,India	28.04.2021 (02:21:26)	1.24	1.11
7	Port Blair, India	17.07.2020 (14:03:40)	1.23	0.76
8	Ternate, Indonesia	14.11.2019 (21:12:54)	1.16	1.11
9	Bengkulu, Indonesia	13.08.2017 (03:08:10)	1.21	0.81
10	Luwuk, Indonesia	15.03.2015 (23:17:16)	1.16	0.72

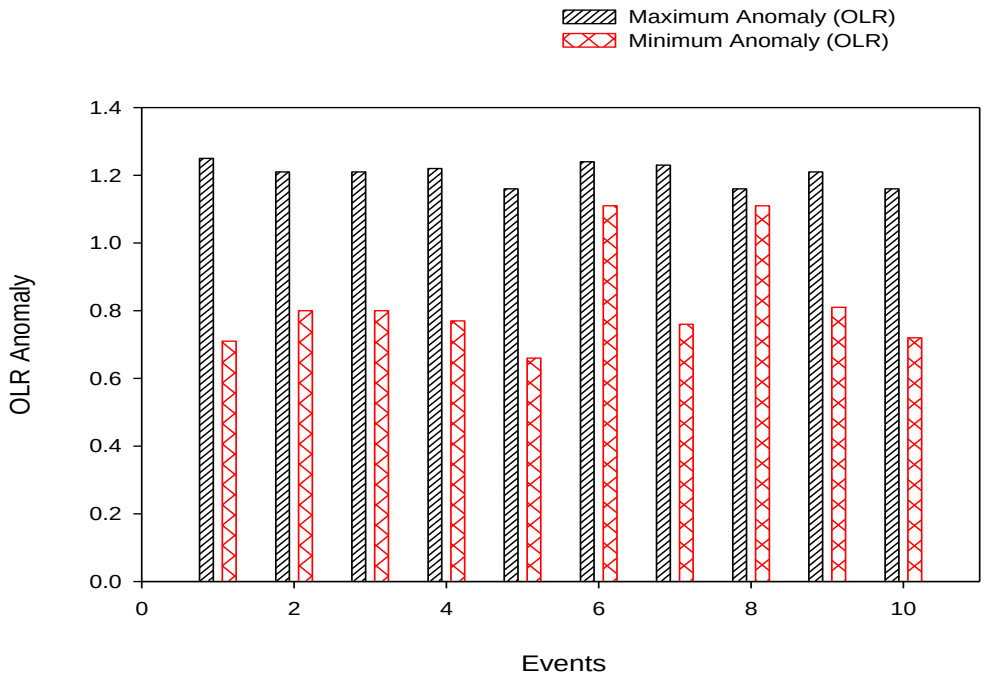

Figure 11. Representation of maximum (black bars) and minimum (red bars) deviation in anomalies of OLR during all the ten earthquake events

DISCUSSION

In the present work, anomalous precursory behaviour of OLR was observed for all the earthquake events. However, they did have distinctive behavioural characteristics. This could be caused by variations in meteorological variables as well as changes in geographic regions. The locations of these ten earthquakes, their epicentres, proximity to the ocean and the robust interplay between land, ocean, and atmosphere, are likely to have a significant impact on the changes in OLR.

All the earthquake events reveal multiple instances where the OLR exceeds the values of the historical time series. Notably, the trends across oceanic and coastal regions are similar. It is observed that the highest number of OLR anomalies, serving as potential precursory signatures, occur several days before the earthquake event. Specifically, a significant increase in OLR is evident between the 30^{th} to 55^{th} days before the all the considered earthquake events, except for Assam, which is a land-based region. The maximum OLR anomaly appears typically around two months before the earthquake, with the earliest anomaly detected as soon as the 5th day (as observed in Assam, India). In Assam, the corresponding OLR values during the earthquake year and the historical time series were 274.16 W/m² and 220.95 W/m², respectively, indicating that the anomaly was 1.24 times higher than the historical average. Anomalous seismic activity was also observed in Assam for up to two months before the earthquake, likely attributed to the region's high earthquake susceptibility due to its tectonic setting.

The present study's analysis of ten earthquakes over the Indonesian and Indian regions, with magnitudes exceeding 6.0, consistently demonstrated detectable OLR anomalies. These OLR anomalies are likely to be influenced by tectonic activity, plate movements, and related atmospheric and surface conditions that precede the earthquakes. The findings suggest that monitoring OLR variations may offer valuable insights into the development of seismic event and early warning particularly in the regions with oceanic influence.

Prior to an earthquake, the epicentral region experienced an increase in infrared heat (IR), which contributed to severe land-ocean atmospheric interactions and anomalous OLR (Sharma et al., 2024). It is considered that the stress buildup in the epicentral region days before the earthquake served a major role in the increase in infrared temperature immediately preceding the earthquake (Wu and Liu, 2009). Earthquakes can alter the local land surface and atmospheric conditions. For example, the sudden release of energy and the subsequent shifting of the Earth's crust can affect surface temperatures and atmospheric composition, potentially causing anomalies in the measured OLR (Mahmood et al., 2017). Large-scale seismic events can disrupt oceanic and atmospheric patterns. These disruptions can affect sea surface temperatures and atmospheric conditions, leading to anomalies in the OLR detected by satellites (Jiao et al., 2018). The movement of tectonic plates can influence geothermal activity, such as the formation of new geothermal vents. Increased geothermal activity can release additional heat into the atmosphere,

affecting local OLR measurements (Rawat et al. 2011). Earthquakes can inject large amounts of ash and gases, such as sulphur dioxide, into the atmosphere. These particles can spread across the globe, reflecting solar radiation and temporarily cooling the Earth's surface. This cooling effect can lead to anomalies in OLR, as the surface emits less infrared radiation due to the lower temperatures. Consequently, monitoring OLR anomalies can help in understanding and potentially predicting the impacts of large-scale seismic events (Xiong and Shen, 2017). Also, the build-up of stress in short focal depth earthquakes is reflected in changes in surface temperature, Surface Latent Heat Flux (SLHF), and Outgoing Longwave Radiation (OLR). As the stress at the fault interface increases, the rocks become compressed, resulting in a reduction in the number of voids within them. The rise and migration of hot radon gases from rock voids toward the Earth's surface , contributes to atmospheric warming (ZiQi et al., 2002). Air ionization also induces thermal effects, such as changes in air humidity and temperature, characterized by an increase in air temperature and a reduction in relative humidity. The rise in surface temperature leads to intensified outgoing thermal radiation, which is particularly noticeable in epicentral regions and corresponds to OLR variations. Continued OLR analysis using various temporally aggregated data (e.g., monthly, daily, from different satellites, and during day/night cycles) holds promise for the early detection of anomalies related to major global earthquakes. However, many theoretical questions remain about the quantitative relationship between longwave radiation flux and seismo-tectonic stress. Despite these uncertainties, OLR could become a valuable parameter in precursor studies, with early anomalies potentially helping to characterize key earthquake parameters, such as location, timing, and magnitude (Pulinets et al., 2006). The appearance of OLR anomalies is influenced by various factors, including earthquake intensity and atmospheric conditions, but is generally correlated with the earthquake's magnitude. All of the occurrences under study have seen the OLR undergo large anomalous changes. Furthermore, anomalies were discovered around 59 days before the earthquake day (i.e. 60^{th} day). Increased tectonic activity in earthquake-prone areas is responsible for these thermal anomalies.

CONCLUSIONS

In this study, we have examined the Outgoing Longwave Radiation (OLR) as a potential precursor to earthquakes, focusing on ten recent high-magnitude (M≥6.0) seismic events. Our findings lead to the following conclusions:

(i) The OLR values exhibited a consistent anomalous increase during all ten earthquake events analysed in this study.

(ii) In all the earthquake events under consideration, OLR values are found to consistently exhibit anomalous behaviour during the pre-earthquake period, with slight variations in their patterns.

(iii) The maximum observed anomalous increase in OLR ranges from 1.16 to 1.25 times greater during earthquake years when compared to the historical time series across all ten earthquake events.

(iv) The minimum observed anomalous increase in OLR ranges from 0.66 to 1.11 times greater during the earthquake years when compared to the historical time series across all ten earthquake events.

(v) The fluctuations in both the maximum and minimum anomalies of OLR are most pronounced for earthquakes that occurred either directly over the ocean or in proximity to it.

(vi) The behavioural pattern of OLR over the land and ocean/near ocean earthquake events were different owing to diverse crustal properties and atmospheric/ meteorological conditions such as humidity, water vapour content etc.

(vii) The accumulation of water vapour leads to the trapping of outgoing radiation, resulting in elevated temperatures over the EPZ. Consequently, the increase in OLR before all the major earthquake events.

ACKNOWLEDGEMENTS

The authors express their gratitude to the NCEP-NCAR website for providing the Outgoing Longwave Radiation (OLR) data. Additionally, they extend their thanks to the United States Geological Survey (USGS) team for sharing valuable earthquake information.

Author Credit Statement

Problem identification and data analysis were conducted by Pooja Sharma and Ananna Bardhan. All authors collaborated in writing the paper.

Data Availability

The paper provides the data and website information.

Compliance with Ethical standards

The authors declare no conflict of interest and confirm adherence to copyright norms.

References

Akhoondzadeh, M., 2024. Earthquake prediction using satellite data: Advances and ahead challenges. Advances in Space Res., 74 (8), 3539-3555

Bardhan, A., Sharma, P., Sahai, A. and Sharma, D.K., 2022. Ionospheric and surface thermal parameters during three high magnitude earthquakes. J. Ind. Geophys. Union, 26(6), 448-461.

Brohan, P., Kennedy, J.J., Harris, I., Tett, S.F. and Jones, P.D., 2006. Uncertainty estimates in regional and global observed temperature changes: A new data set from 1850. J. Geophys. Res. Atmospheres, 111 (D12). htttps://doi.org/10.1029/2005JD006548

Choudhury, S., Dasgupta, S., Saraf, A.K. and Panda, S., 2006. Remote sensing observations of pre-earthquake thermal anomalies in Iran. Int. J. Remote Sensing, 27(20), 4381-4396. https://doi.org/10.1080/01431160600851827

Dobrovolsky, I.P., Zubkov, S.I. and Miachkin, V.I., 1979. Estimation of the size of earthquake preparation zones. Pure Appl. Geophys., 117(5), 1025-1044.

Fu, C.C., Lee, L.C., Ouzounov, D. and Jan, J.C., 2020. Earth's outgoing longwave radiation variability prior to M≥ 6.0 earthquakes in the Taiwan area during 2009–2019. Frontiers in Earth Sci., 8, 64, p.364.

Ghosh, S., Sasmal, S., Maity, S.K., Potirakis, S.M. and Hayakawa, M., 2024. Thermal Anomalies Observed during the Crete Earthquake on 27 September 2021. Geosciences, 14(3), p.73.

Gruber, A. and Krueger, A., 1984. The status of the NOAA outgoing longwave radiation dataset. Bull. Am. Meteorol. Soc., 65,958–962

Hafeez, A., Ehsan, M., Abbas, A., Shah, M. and Shahzad, R., 2022. Machine learning-based thermal anomalies detection from MODIS LST associated with the M w 7.7 Awaran, Pakistan earthquake. Natural Hazards, 111, 1-19,

Hameed, A., Shah, M., Ghaffar, B., Riaz, S., Jamjareegulgarn, P., Alarifi, N.S. and Abukhadra, M.R., 2024. Possible atmospheric-ionospheric precursors of the 2020 Hotan China earthquake from various satellites. Adv. Space Res., 74(7), 3326-3343.

Jiao, Z.H., Zhao, J. and Shan, X., 2018. Pre-seismic anomalies from optical satellite observations: a review. Natural Hazards and Earth Syst. Sci., 18(4), 1013-1036.

Jing, F., Singh, R.P., Sun, K. and Shen, X., 2018. Passive microwave response associated with two main earthquakes in Tibetan Plateau, China. Adv. Space Res., 62(7), 1675-1689.

Liesmann, B. and Smith, C.A., 1996. Description of a complete (interpolated) outgoing longwave radiation dataset. Bull. Am. Meteorological Soc., 77(6), 1275-1277.

Liu, J.Y., Chuo, Y.J., Shan, S.J., Tsai, Y.B., Chen, Y.I., Pulinets, S.A. and Yu, S.B., 2004, Pre-earthquake ionospheric anomalies registered by continuous GPS TEC measurements. In: Ann. Geophysicae, 22(5), 1585-1593.

Mahmood, I., Iqbal, M.F., Shahzad, M.I. and Qaiser, S., 2017. Investigation of atmospheric anomalies associated with Kashmir and Awaran Earthquakes. J. Atmosph. and Solar-Terrestrial Phys., 154, 75-85.

Niu, F., 2008. Preseismic Velocity Changes Observed from Active Source Monitoring at the Parkfield SAFOD. Info: Lawrence Berkeley National Laboratory.

Ouzounov, D. and Freund, F., 2004. Mid-infrared emission prior to strong earthquakes analyzed by remote sensing data. Adv. space Res., 33(3), 268-273.

Ouzounov, D., Liu, D., Chunli, K., Cervone, G., Kafatos, M. and Taylor, P., 2007. Outgoing long wave radiation variability from IR satellite data prior to major earthquakes. Tectonophysics, 431(1-4), 211-220.

Piscini, A., De Santis, A., Marchetti, D. and Cianchini, G., 2017. A Multi-parametric climatological approach to study the 2016 Amatrice–Norcia (Central Italy) earthquake preparatory phase. Pure Appl. Geophys., 174, 3673-3688.

Piscini, A., Marchetti, D. and De Santis, A., 2019. Multi-parametric climatological analysis associated with global significant volcanic eruptions during 2002–2017. Pure Appl. Geophys., 176, 3629-3647.

Pulinets, S. and Boyarchuk, K., 2004. Ionospheric precursors of earthquakes. Springer Science & Business Media.

Pulinets, S. and Ouzounov, D., 2011. Lithosphere–Atmosphere–Ionosphere Coupling (LAIC) model–An unified concept for earthquake precursors validation. J. Asian Earth Sci., 41(4-5), 371-382.

Pulinets, S.A., Legen'Ka, A.D., Gaivoronskaya, T.V. and Depuev, V.K., 2003. Main phenomenological features of ionospheric precursors of strong earthquakes. J. atmospheric and solar-terrestrial phys., 65(16-18), 1337-1347.

Pulinets, S.A., Ouzounov, D., Karelin, A.V., Boyarchuk, K.A. and Pokhmelnykh, L.A., 2006. The physical nature of thermal anomalies observed before strong earthquakes. Phys. Chem. Earth, Parts A/B/C, 31(4-9), 143-153.

Qasim, M., Shah, M., Shahzad, R. and Jamjareegulgarn, P., 2024. Atmospheric precursors from multiple satellites associated with the 2020 Mw 6.5 Idaho (USA) earthquake. Adv. Space Res., 73(1), 440-455.

Rawat, V., Saraf, A.K., Das, J., Sharma, K. and Shujat, Y., 2011. Anomalous land surface temperature and outgoing long-wave radiation observations prior to earthquakes in India and Romania. Natural hazards, 59, 33-46.

Schulz, J., Meywerk, J., Ewald, S. and Schlüssel, P., 1997. Evaluation of satellite-derived latent heat fluxes. J. Climate, 10(11), 2782-2795.

Shah, M., Tariq, M.A. and Naqvi, N.A., 2019. Atmospheric anomalies associated with Mw> 6.0 earthquakes in Pakistan and Iran during 2010–2017. J. Atmospheric and Solar-Terrestrial Phys., 191, 105056.

Sharma, P., Bardhan, A., Kumari, R., Sharma, D.K., and Sharma, A.K., 2024. Variation of Surface Latent Heat Flux (SLHF) observed during high-magnitude earthquakes. J. Ind. Geophys. Union, 28(2), 131-142.

Tramutoli, V., Cuomo, V., Filizzola, C., Pergola, N. and Pietrapertosa, C., 2005. Assessing the potential of thermal infrared satellite surveys for monitoring seismically active areas: The case of Kocaeli (Izmit) earthquake, August 17, 1999. Remote Sensing of Environment, 96(3-4), 409-426.

Tronin, A.A., 2006. Remote sensing and earthquakes: A review. Phys. Chem. Earth, parts A/B/C, 31(4-9), 138-142.

Tronin, A.A., Hayakawa, M. and Molchanov, O.A., 2002. Thermal IR satellite data application for earthquake research in Japan and China. J. Geodynamics, 33(4-5), 519-534.

Uyeda, S., Nagao, T. and Kamogawa, M., 2009. Short-term earthquake prediction: Current status of seismo-electromagnetics. Tectonophysics, 470(3-4), 205-213.

Venkatanathan, N., Kaarthick, B. and Priyadharshini, C., 2013. OLR anomalies prior to big earthquakes (Mw> 6.0)–a case study on earthquakes of India's neighboring region occurred during the year 2012. New Concepts Global Tecton, 1(3), 34-44.

Venkatanathan, N. and Natyaganov, V., 2014. Outgoing longwave radiations as pre-earthquake signals: preliminary results of 24 September 2013 (M 7.7) earthquake. Curr. Sci., 106(9), 1291-1297.

Weiyu, M., Xuedong, Z., Liu, J., Yao, Q., Zhou, B., Yue, C., Kang, C. and Lu, X., 2018. Influences of multiple layers of air temperature differences on tidal forces and tectonic stress

before, during and after the Jiujiang earthquake. Remote sensing of environment, 210, 159-165.

Wu, L. and Liu, S., 2009. Remote sensing rock mechanics and earthquake thermal infrared anomalies. In: Advances in Geoscience and Remote Sensing. Intech Open. DOI:10.5772/8292

Xiong, P. and Shen, X., 2017. Outgoing longwave radiation anomalies analysis associated with different types of seismic activity. Adv. Space Res., 59(5), 1408-1415.

Zhang, W., Zhao, J., Wang, W., Ren, H., Chen, L. and Yan, G., 2013. A preliminary evaluation of surface latent heat flux as an earthquake precursor. Natural Hazards and Earth Sys. Sci., 13(10), 2639-2647.

Ziqi, G., ShuQing, Q., Chao, W., Zhi, L., Xing, G., Weiguo, Z., Yong, Y., Hong, Z. and Jishuang, Q., 2002, The mechanism of earthquake's thermal infrared radiation precursory on remote sensing images. In: IEEE Int. Geosci. Remote Sensing Symp., 4, 2036-2038. IEEE.

Received on: 28-05-2024; Revised on: 14-01-2025; Accepted on: 14-01-2025

J. Ind. Geophys. Union, 29(2) (2025), 101-114
https://doi.org/10.71122/JIGU.29(2)2025.0011

Imaging challenges and mitigations in the Tripura Fold Belt areas for reservoir characterization and hydrocarbon prospecting

Manoj Kumar Bhartee[1*], Uma Shankar[2], Yadunath Jha[1] and Nani Madhab Dutta[3]
[1]Oil and Natural Gas Corporation Limited, Dehradun-248001, India
[2]Banaras Hindu University, Varanasi-221005, India
[3]Oil and Natural Gas Corporation Limited (Retd.), Jorhat-785001, India
[*]Corresponding author: manojbhartee86@gmail.com

ABSTRACT

Even though there have been substantial advancements in seismic data acquisition and processing, imaging in structurally complex regions like fold belts has seen only marginal improvement. In such geologically intricate areas, the conventional imaging approach may not yield satisfactory results. While 3D surface seismic surveys are preferred, acquiring 3D seismic data can be challenging due to logistical constraints. Moreover, the rugged terrain and difficult accessibility in these areas make 3D land seismic data acquisition prohibitively expensive. Conventional 2D land seismic data also has limitations, particularly in accurately imaging anticlinal features. An alternative to traditional 2D surveys in such contexts is the swath-line recording geometry. Swath-line recording offers significantly higher fold (720-fold in the present case), compared to typical 2D land surveys, resulting in data with an improved signal-to-noise ratio. However, several issues adversely impact imaging quality in thrust fold belts. Key factors affecting the quality of processed outputs include geometry, statics, and poor signal-to-noise ratio. Survey objectives may remain unmet unless these factors are addressed or minimized. We utilized a hybrid approach, combining multiple techniques including geometry corrections, nonlinear tomography-based statics solutions, velocity estimation using the CVS method, and leveraging different software suites and algorithms to address these inherent challenges.

Keywords: Tripura Fold belt, Swath-line, CMP line, S/N ratios, Semblance, Constant velocity stack method (CVS), PSTM

INTRODUCTION

Various factors negatively impact the quality of imaging in thrust fold belts. These include geometry, statics, and a poor signal-to-noise (S/N) ratio. Unless these issues are minimized or eliminated, the objectives of the survey may not be achieved. Moreover, processing parameters are highly sensitive to such complex data if the necessary remedies for the aforementioned factors are not considered. Therefore, a systematic approach is crucial to address these inherent problems. The fundamental prerequisites for a good seismic image include a good S/N ratio, a suitable and geologically compatible near-surface model for accurate statics calculation, a good subsurface velocity model, and the best imaging algorithm that fits the geological condition. However, processors in fold belt areas often face challenges in obtaining these processing ingredients easily, leading to significant challenges in processing. Efforts are made to address these major challenges and issues to achieve better data quality. However, no amount of processing effort can fully replace the importance of acquisition efforts. Despite advancements in seismic data processing and acquisition, the improvement in imaging in structurally complex areas like fold belts has been marginal. Traditional imaging methods have not yielded satisfactory results in such geologically complex locations. While 3-D surveys are preferred in these areas, collecting 3-D land seismic data is not always feasible or economical due to issues such as difficult terrain and limited accessibility. The limitations of conventional 2-D land seismic data become especially apparent in fold belt areas, where accurately capturing the anticlinal section can be a challenge.

The aim of the present study is to devise a workflow specifically for the Tripura fold belts, making use of the existing legacy seismic data in our area of study. We are concentrating on tackling various challenges that affect image quality, such as geometry, statics, noise, velocity, and algorithms. When it comes to new data acquisition, our approach is to gather high-quality seismic data using innovative geometry, while taking into account the logistics, scheduling, and cost-effectiveness of fold belt operations. We investigate the viability of 2-D swath-line geometry as a potential solution for the Tripura fold belt region, and present a comparative discussion on the acquisition, processing, and results with traditional 2-D methods in our case study.

STUDY AREA

The Assam and Assam Arakan basin is an onshore basin situated in the north-eastern part of India and has been categorized as a Category-I basin (Rajkhowa et al.,2018). On the basis of morphological characteristics, the Assam and Assam-Arakan basin (A&AA Basin), is subdivided into a foreland and a fold belt. The foreland comprises of area including the Brahmaputra arch and it's southern and northern slopes and is commonly known as Upper Assam Shelf North (UAN); the area encompassing the south eastern slope of Shillong and Mikir Massifs is commonly known as Upper Assam Shelf South (UAS). The A&AA Fold Belt comprises the Naga Schuppen Belt and sigmoidal en-echelon folds of Tripura-Cachar-Fold Belt.

The geomorphology of fold belt is typified by a succession of hill ranges and valleys of meridonial and sub meridonial trends (Dasgupta and Biswas, 2000). The height of these ranges varies from 200 to 500 m. The general elevation increases to the east in the region. Fold-belt has complex evolution history and

characterized by series of parallel, elongated and doubly plunging, asymmetric anticlines arranged in en-echelon pattern and separated by wide and narrow synclines like Khowai and Baramura, with the general trend of the anticlines being NNW - SSE to N-S with slight convexity towards west and longitudinal faults bounding the flanks. The intensity of folding increases towards east with progressively older rocks being exposed in the cores of the anticlines. Our study focuses on the Baramura anticline, located in the western Tripura Fold Belt (Figure 1).

Baramura field located in this area is an asymmetric doubly plunging anticline trending roughly north-northeast-to-south-southwest. Tectonically, Baramura falls in the frontal folded belt of Tripura, which is the western continuation of the Surma Valley folded belt. The eastern flank of Baramura structure has been affected by a westward dipping thrust and with the main hydrocarbon potential falling in Bokabil and Upper Bhuban formations of Miocene age (Chattopadhyay and Ghosh, 2006). Fold belts are regions where the Earth's crust has been deformed and folded due to tectonic forces. These areas are significant for petroleum exploration due to their complex geological structures, which can create traps for hydrocarbons. (Figure 2) depicts the Tripura fold belt area's stratigraphy and petroleum system.

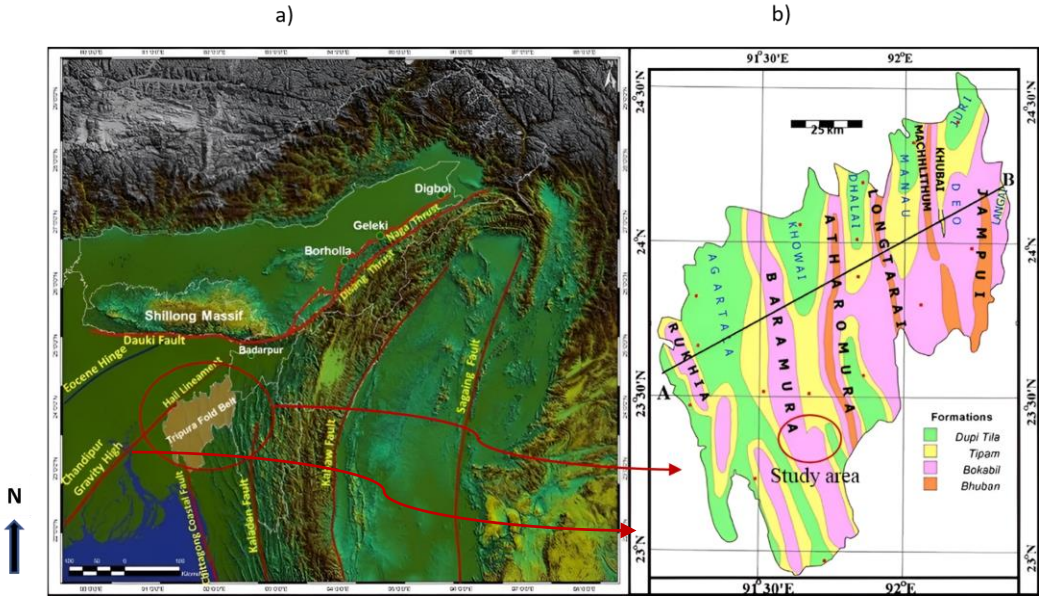

Figure 1. Location of the study area in Tripura, India. **(a)** Regional tectonic elements of Tripura Fold Belt and adjoining areas on Digital Elevation Model (DEM) (after Samal et al., 2017) and **(b)** Alternative anticlines and synclines of Tripura (after Bandyopadhyay et al., 2013)

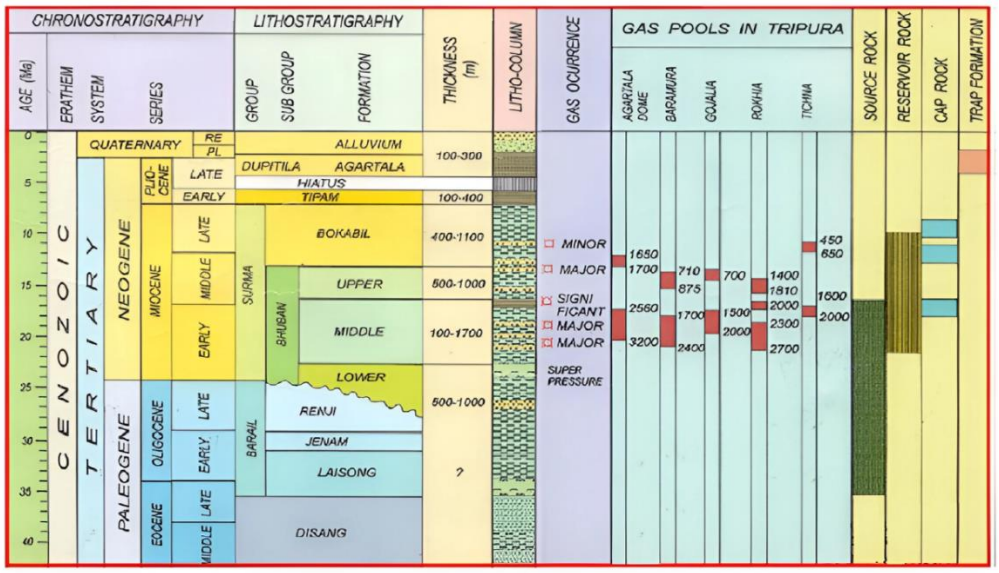

Figure 2. Generalized stratigraphy of Tripura Fold Belt (after Brahma and Sircar, 2018).

METHODOLOGY

To establish a fold belt-friendly workflow, several seismic legacy data from nearby study areas have been reprocessed with several quality checks. The effectiveness of this approach is evident in addressing various challenges related to image quality, including geometry, statics, noise, velocity, and algorithms.

Geometry QC

Difficult logistics leads to relocation of shots/receivers from planned pickets and if it's not updated properly such positional errors leads to incorrect geometry merging and further leads to wrong CMP and offsets computation. These issues require proper reconciliation, every shot record needs to be viewed and checked for correct coordinate assignment. Misplaced shots must be relocated to its correct position, shot by shot, interactively. This problem is commonly observed while reprocessing vintage data. Hence, these should be checked during merging, (Figure 3) shows the correction of shot position and its effect.

Solution for statics corrections

In conventional processing scenario, statics applied on the geometry merged gather are actually supplied by field crews and derived on the basis of near surface model estimated using sparse uphole data or shallow refraction survey. But in case of fold belt data in areas like Tripura; Assam and Assam Arakan Basin, this is no longer valid due to highly undulated acquisition surface and complex near surface geology (Berryhill, 1979; Beasley and Lynn, 1992, Bhartee et al., 2022).

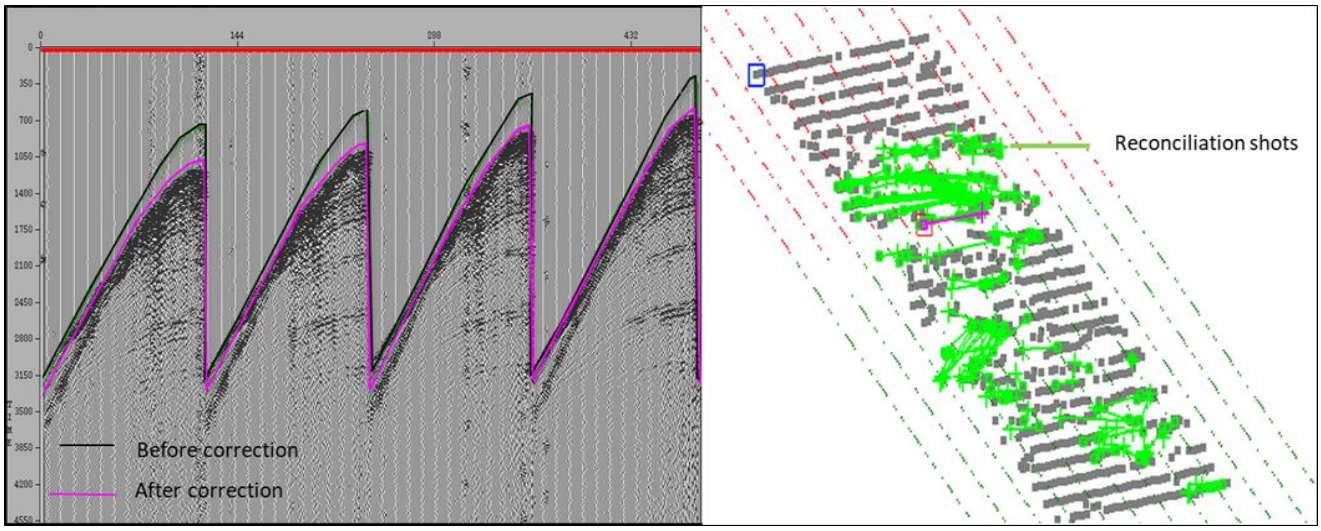

Figure 3. Example of shot point correction on a legacy 3D data from study area.

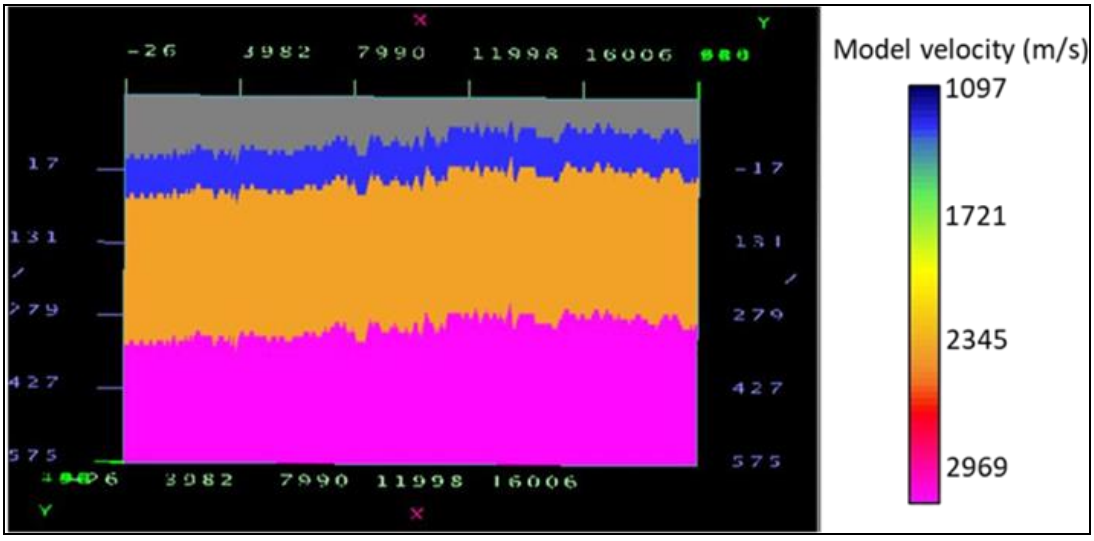

Figure 4. A workstation screenshot showing the initial near-surface velocity model used for computation of refraction statics.

First arrival turning ray tomography (Zhang and Toksoz, 1998: Zhu et al., 2000) also called nonlinear tomography (Tomostatics) based static solutions are more beneficial for deriving both weathering statics as well as near surface velocity model for proper imaging. Tomostatics is an iterative algorithm designed to minimize the difference between observed and predicted first arrival travel times, based on a user-supplied initial near-surface model (Figure 4). Observations suggest that in fold belt areas, Conventional field statics often fail to produce geologically plausible near-surface models. Conversely, tomostatic-derived models tend to provide a more accurate fit. The efficacy of the tomostatics in fold belt areas are shown on gather level in (Figure 5) and stack level in (Figure 6). It is easily understood that the meaningful seismic events have been shaped after application of tomography-based refraction static solutions for near surface model.

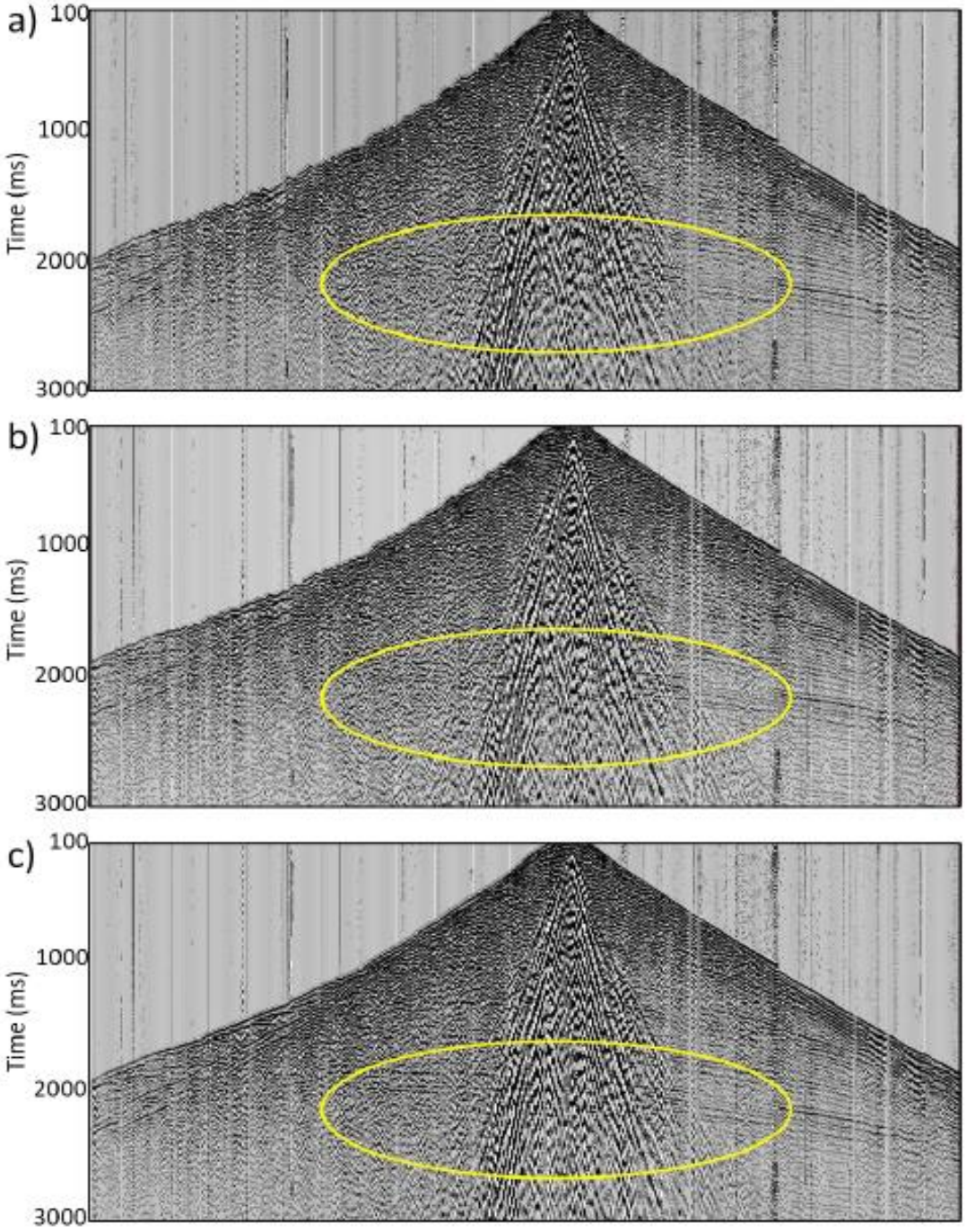

Figure 5. Comparison of a shot gather from a single receiver line of swath-line with **(a)** no field statics applied, **(b)** after application of field statics, and **(c)** after application of refraction statics the improvement in the coherency of reflection events is evident.

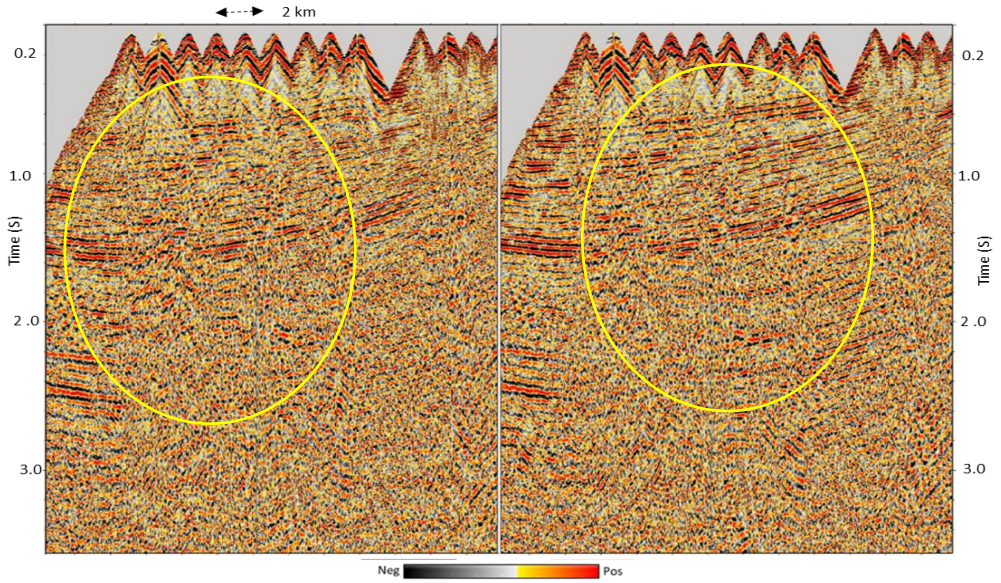

Figure 6. Comparison of stacks with application of field statics (left) to refraction statics (right)

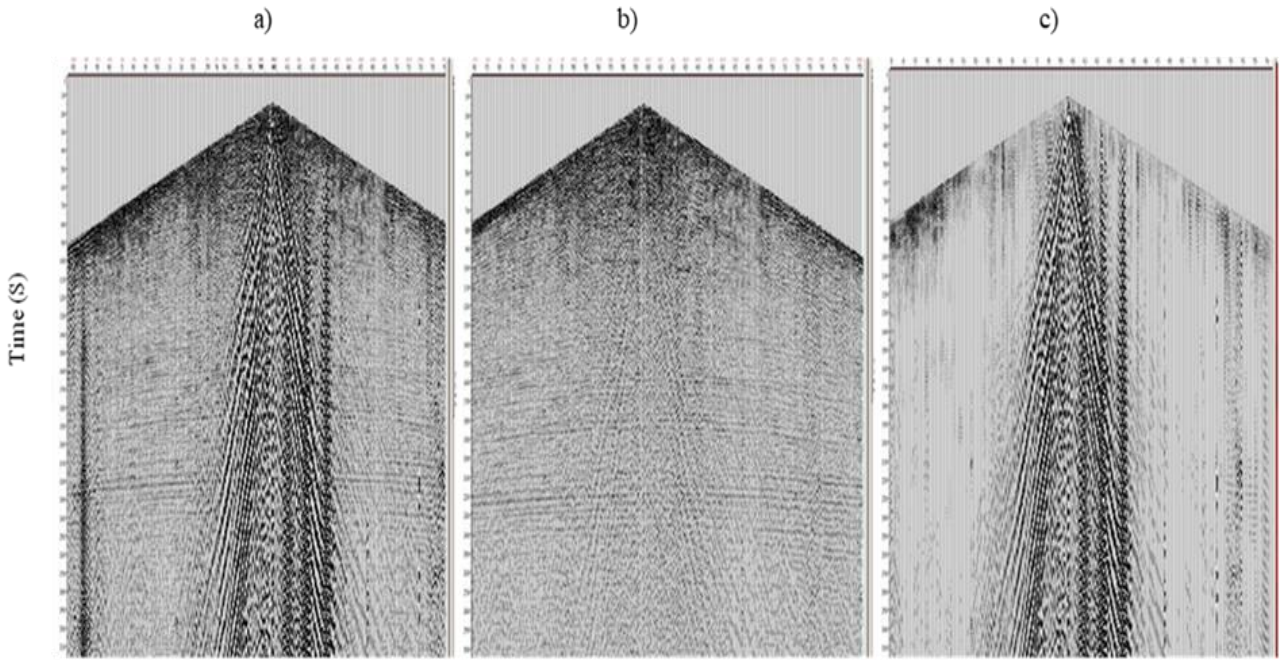

Figure 7. Progression from raw data **(a**) to denoised data **(b),** and finally to the removal of noise **(c).**

Noise Attenuations

Signal to noise ratio (S/N) in fold belt seismic data especially over exposed anticlines is very poor (Dutta et al., 2015**).** Reflection hyperbolae pattern is hardly observed. In structurally complex areas out of plane reflections are very common. Hence, it is important to get rid of masked noise in data cautiously. Carried out frequency dependent noise attenuation in narrow bands and thereby enabling searching of anomalous amplitudes and subsequent attenuation (Yilmaz, 1987). (Figure 7) illustrates a shot gather before and after denoising.

Velocity Analysis

Velocity analysis plays a crucial role in the fold belt data (Dutta et al., 2015). As the consistent reflection hyperbolae are nearly absent in gather level, it becomes difficult to carry out velocity analysis based on flattening of hyperbolae (Figure 8). Semblance based approach on super gather also does not give reliable estimate of the velocity.

Under these circumstances constant velocity stack method (CVS) of velocity analysis is helpful to get an initial estimate of velocity (Figure 9).

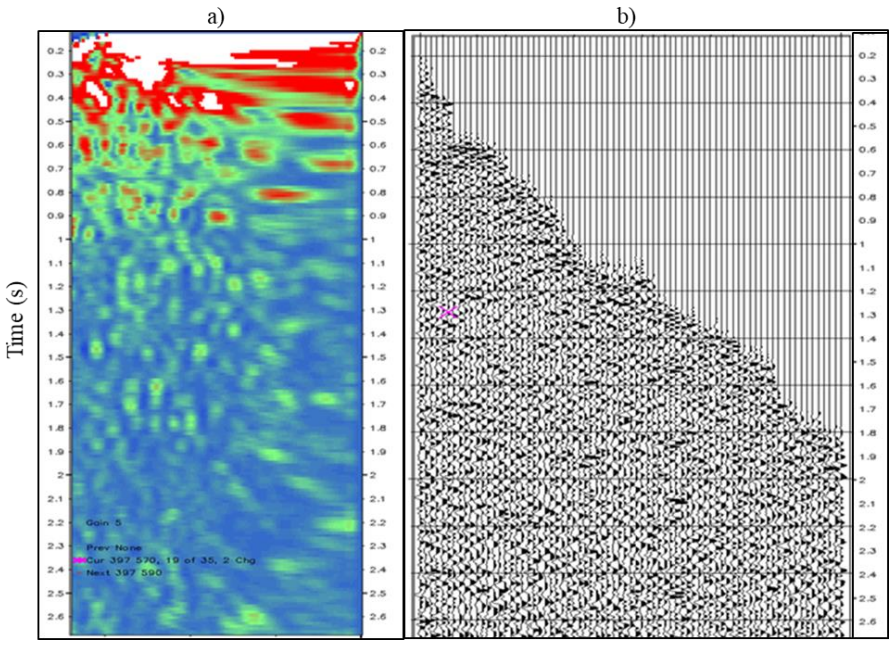

Figure 8. Poor semblance near anticlinal part **(a)** and absence of hyperbolic events on corresponding CMP gather **(b).**

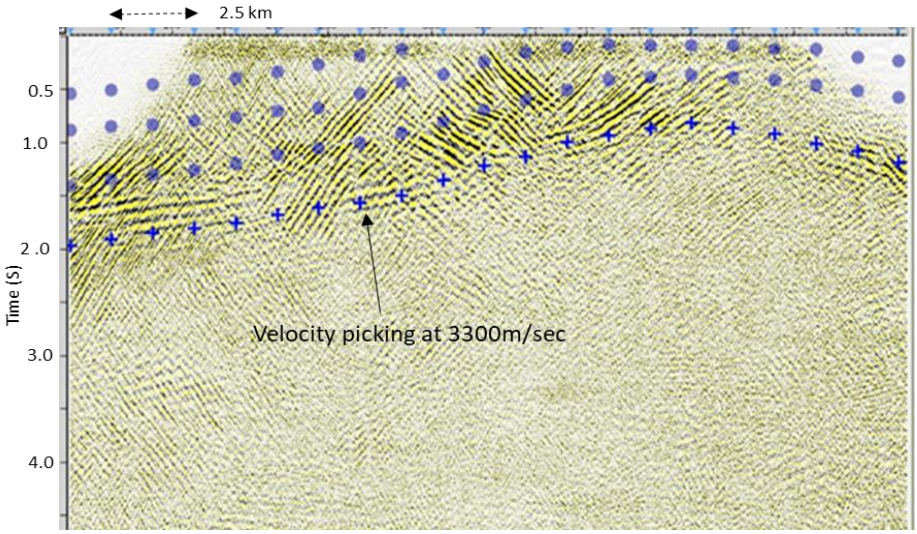

Figure 9. Constant Velocity Stack (CVS) for velocity picking

Multiple iterations of CVS velocity estimation need to be carried out to get the optimal stack result. In order to pick CVS based velocity, a prior knowledge of geological structure is essential. Velocity analysis on post stack migrated output with velocity perturbation is also provide better image quality in some area where S/N is poor.

The quality of vintage data from the Tripura fold belt areas improved significantly by implementing the special quality control steps and parameters mentioned above during processing. A comparison of the PSTM stack of the vintage 2D line is shown in (Figures 10). PSTM stack (10a) was processed using field statics and semblance-based velocity estimation, while (10b) was processed following fold-belt-friendly processing steps as discussed earlier.

Technological advancements in processing algorithms and human efforts consistently yield high-quality results. However, setbacks during data acquisition can never be fully mitigated. Acquiring and processing new data with a geometry suited for fold belt areas is crucial for a better understanding of the subsurface. More importantly, implementing this geometry on the ground while addressing the challenges of the fold belt area is a significant task. An innovative geometry, the '2D swath-line' seismic data acquisition, could potentially alleviate these imaging difficulties in the fold belt.

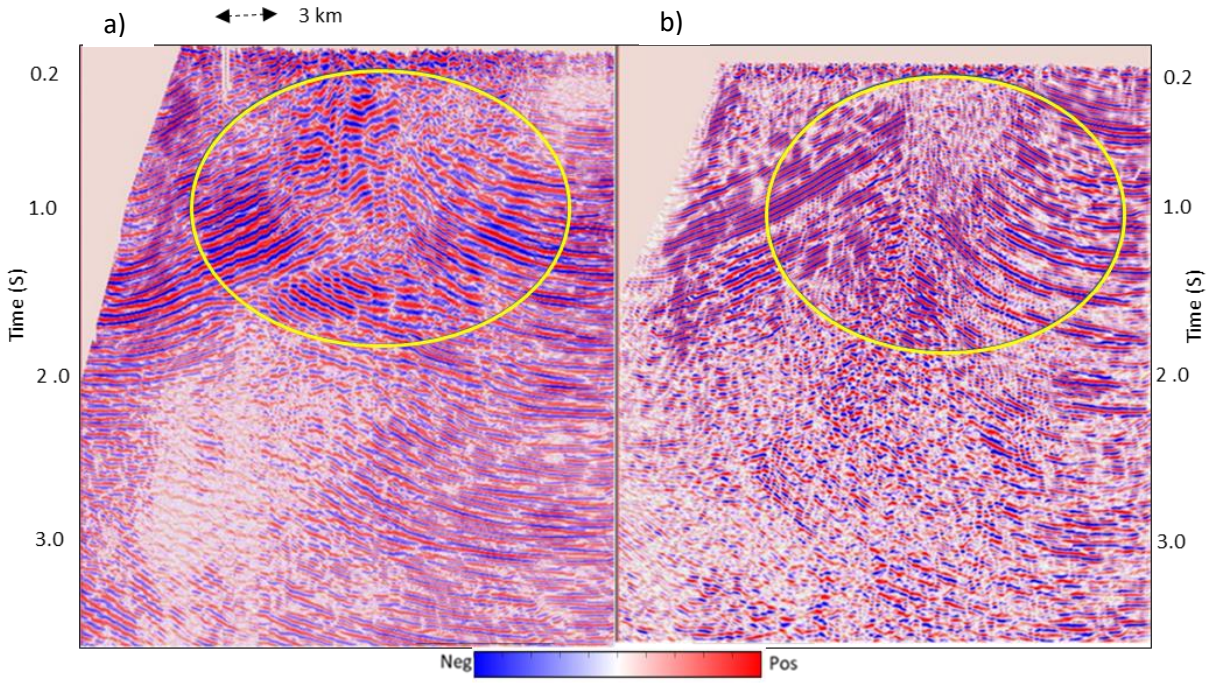

Figure 10. Comparison of PSTM stacks of a vintage 2D line **(a)** of Tripura fold belt area and by adopting special processing steps **(b)**

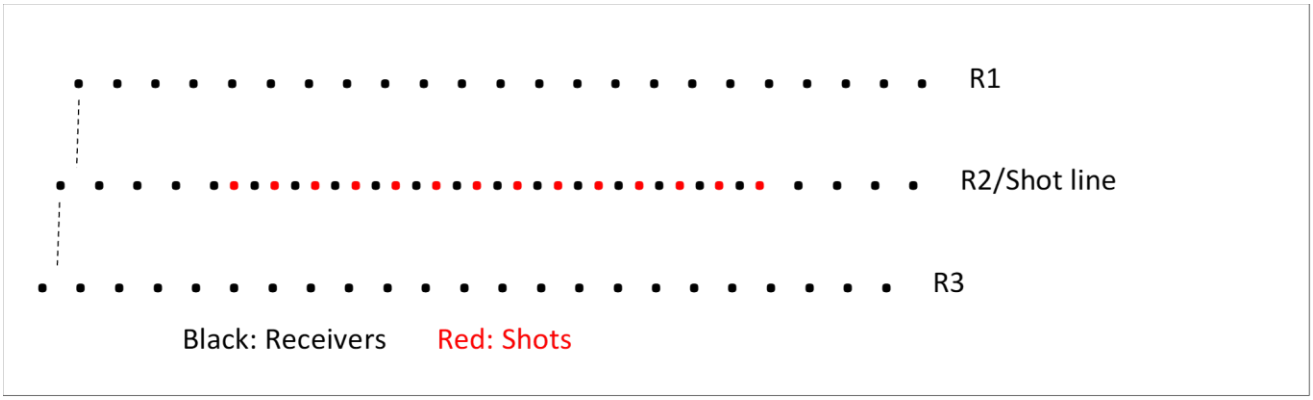

Figure 11. The swath-line recording geometry adopted in the seismic data acquisition.

The 2D swath-line acquisition geometry combines the concepts of stack array with 3D acquisition techniques; here in this case study, it consists of one additional receiver line on both sides of conventional 2D seismic survey. This geometry provides excellent protection against scattered and out-of-plane surface noise, while permitting the use of limited crossline aperture and 3D swath processing techniques to preserve signal fidelity. Swath-line seismic data were acquired as a practical alternative to conventional 2D land data acquisition to map an anticline in an area situated in the north-eastern part of India with rough topography and difficult accessibility. The recording geometry consists of three parallel receiver lines at 40 m separation and a single shot line along central receiver line (Figure 11).

The receiver interval was 10 m. Symmetrical split spread geometry with 480 + 480 active channels in each receiver line and total 2880 channels in an active temple was used. Full-fold coverage along the CMP line is 720; significantly higher than the fold that can be attained by conventional 2-D surveys. (Figure 12) shows the raw shot gather of the swath-line acquisition geometry, while (Table 1) lists the important recording parameters. A total of nine sets of 2D swath line data were acquired: six aligned in the dip direction and three in the strike direction, aimed at mapping the South Baramura anticline. All these lines are illustrated on a Google Map and Geological Map in (Figures 13a and 13b**)**, respectively.

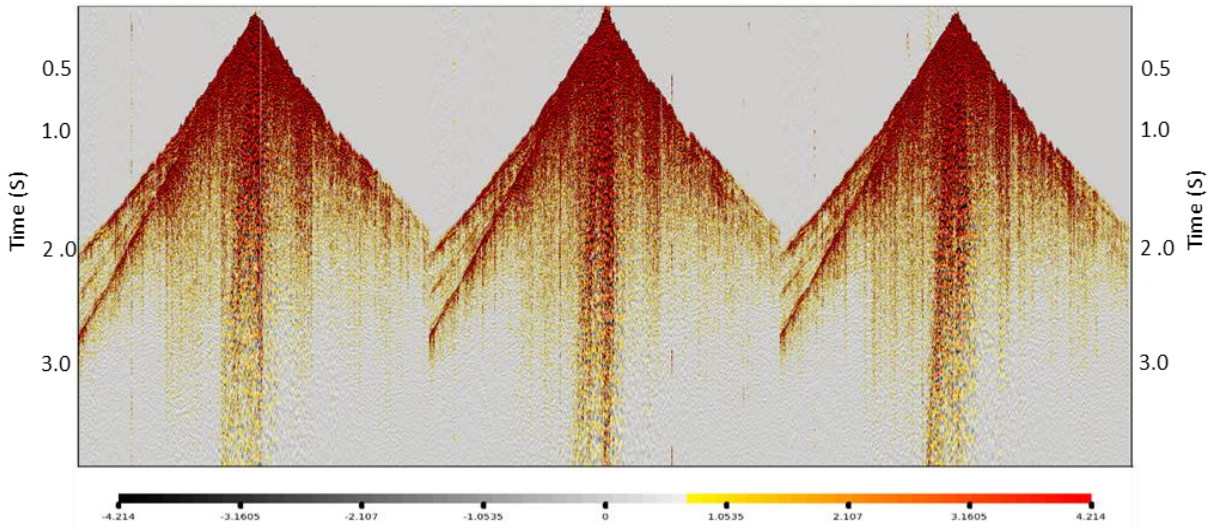

Figure 12. Raw shot gather with swath-line acquisition geometry

Table1. The swath-line acquisition parameters

Receiver line spacing	40 m
Receiver interval	10 m
Shot interval	20 m
Number of channels per receiver line	960
Number of receiver lines	3
Total number of channels	2880
Number of shot lines	1
Min/Max offset	5 m/4800 m
Fold along the CMP line	720

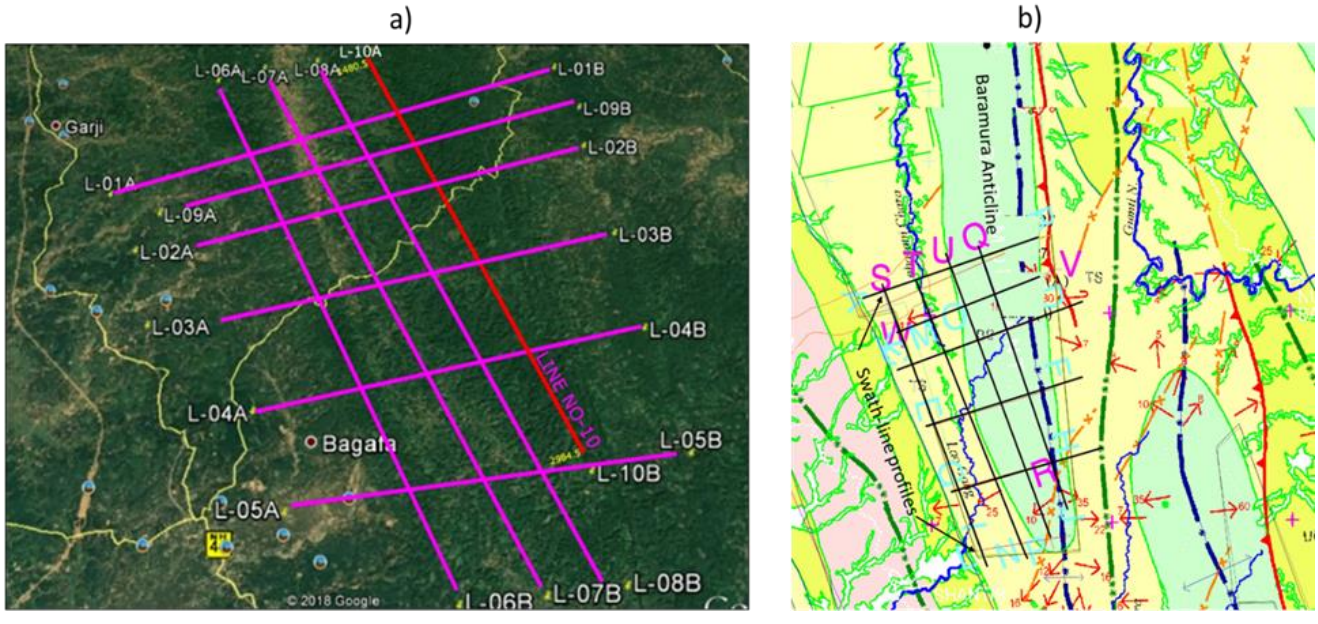

Figure 13. Swath line profiles shown on **(a)** Google Map and **(b)** Geological Map of the South Baramura Anticline.

Data analysis

Swath-line data must be treated as 3D data during most of the stages of processing, including near-surface modelling and subsurface imaging. Topography variation is very high and rapid in the survey area. An elevation profile of receivers along the dip direction in a swath line shows the variation to be between 10 and 130 m (Figure 14), and a profile of shots along the central shot line shows the variation to be between 40 and 130 m (Figure 15). The nonlinear travel time tomography (Zhang and Toksoz, 1998) was applied to the first-arrival times picked from the shot gathers and estimated a near-surface velocity model for statics corrections.

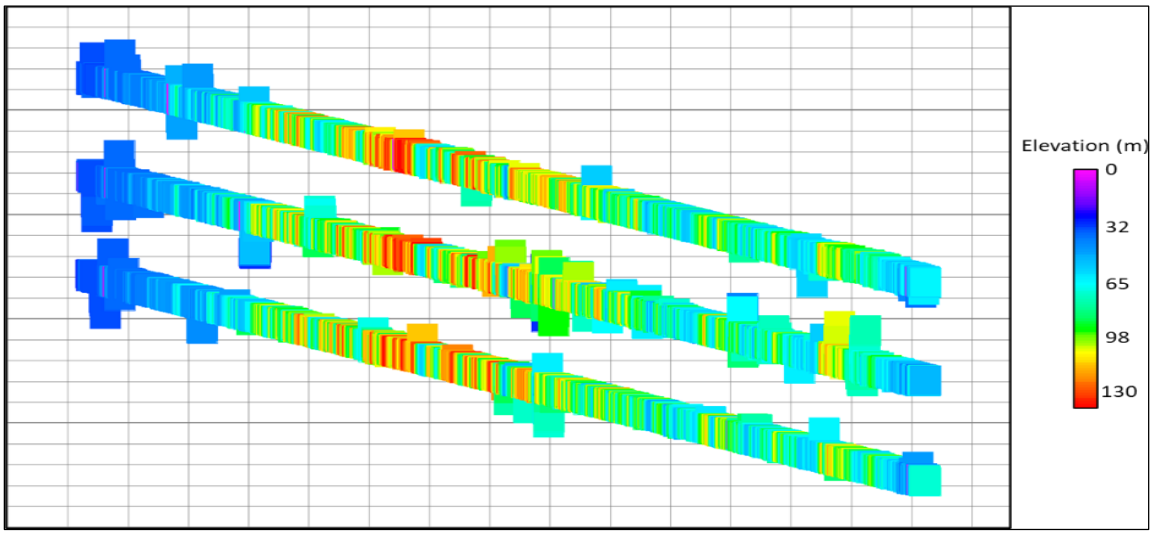

Figure 14. The elevation profile of receivers along the swath lines showing the variation to be between 10 and 130 m.

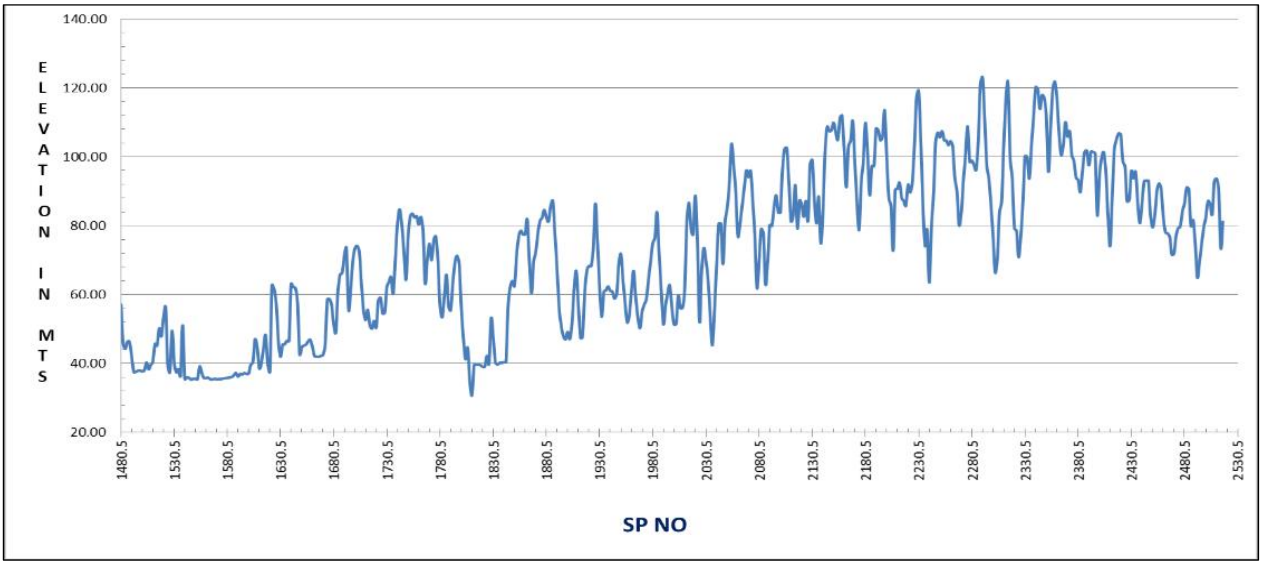

Figure 15. The elevation profile of shots showing the variation to be between 40 and 130 m.

The workflow mentioned in (Figure 16) was applied to process the data, which included geometrical spreading correction, followed by cascaded application of noise attenuation in the shot and CMP domains, aimed at reducing the strength of surface waves and guided waves. It is often found that in the seismic data from fold belt areas, the signal-to-noise ratio (S/N) over anticlines is low due to complex geological structures, shadow zones, out-of-plane reflections, and surface noise. The coherent reflection hyperbolic patterns are usually not visible. Therefore, it is important to eliminate noise to enhance the reflection strength. A processing flow chart is depicted in (Figure 16).

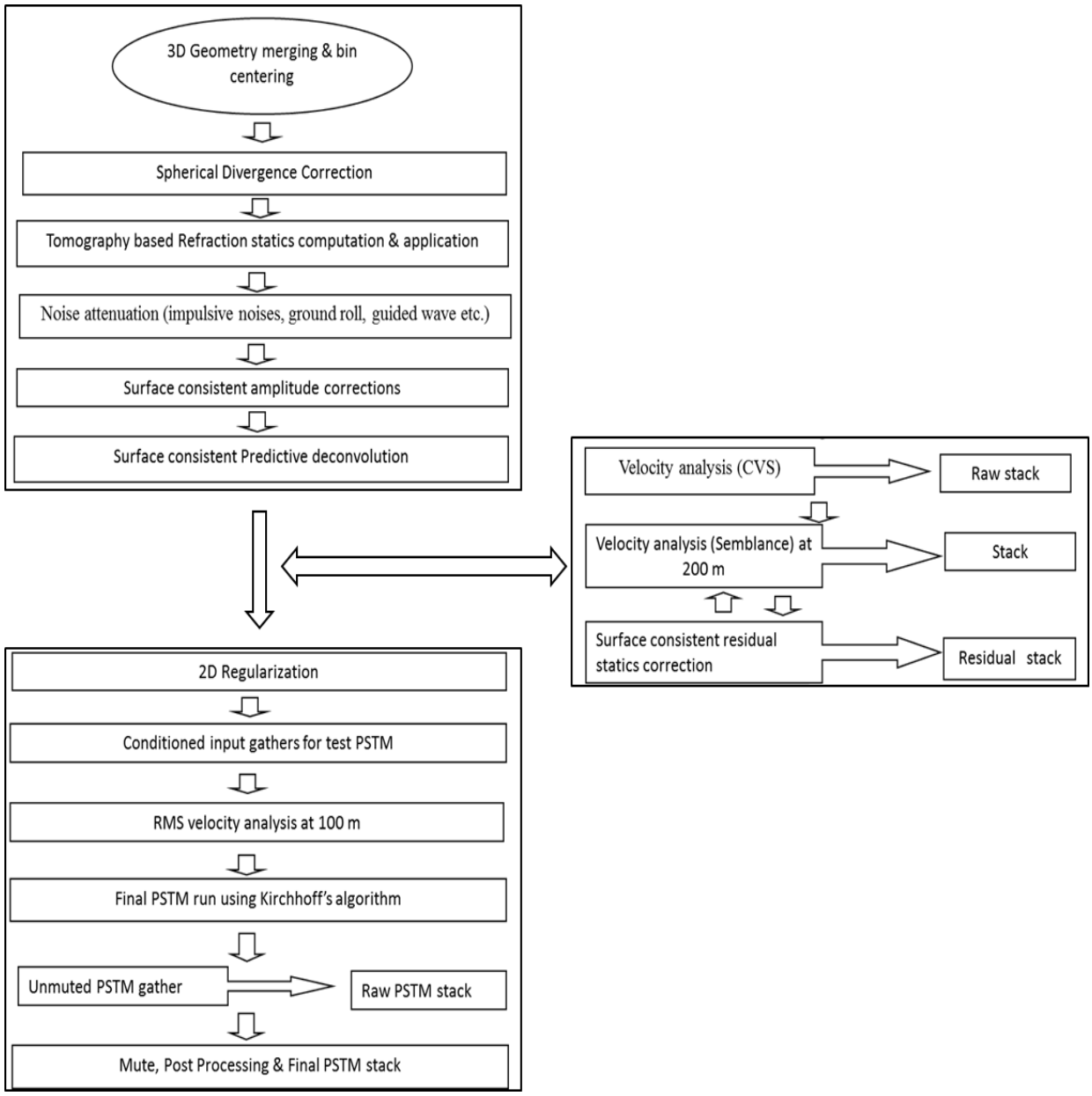

Figure 16. Processing flow chart of swath line data.

Typically, noise removal algorithms assume that the signal strength is significantly greater in magnitude than the interfering noise. However, in this specific context, the signal-to-noise ratio is small. As a result, we performed frequency-dependent noise attenuation within narrow frequency bands. This approach allowed us to identify anomalous amplitudes and apply appropriate attenuation techniques. At the initial stage, minimal noise removal is applied to preserve the signal. Subsequently, signal enhancement occurs after velocity refinements and on the post-stack level, as needed. In this dataset, velocity analysis plays a critical role due to the scarcity of consistent reflection hyperbolae in seismic gathers. Consequently, traditional velocity analysis methods based on hyperbola flattening become challenging. Even a semblance-based approach with super gather fails to provide reliable velocity estimates. Under these circumstances, the constant velocity stack (CVS) method proves valuable for obtaining an initial velocity estimate. We iteratively refined the velocity to achieve optimal stacked results.

The comparison of seismic data stacks across different processing stages, is denoted as (a) to (d) in the (Figure 17). Notably, improvements have been consistently observed at each processing stage. A detailed parameter testing and comprehensive quality control checks have been meticulously implemented across the entire processing workflow.

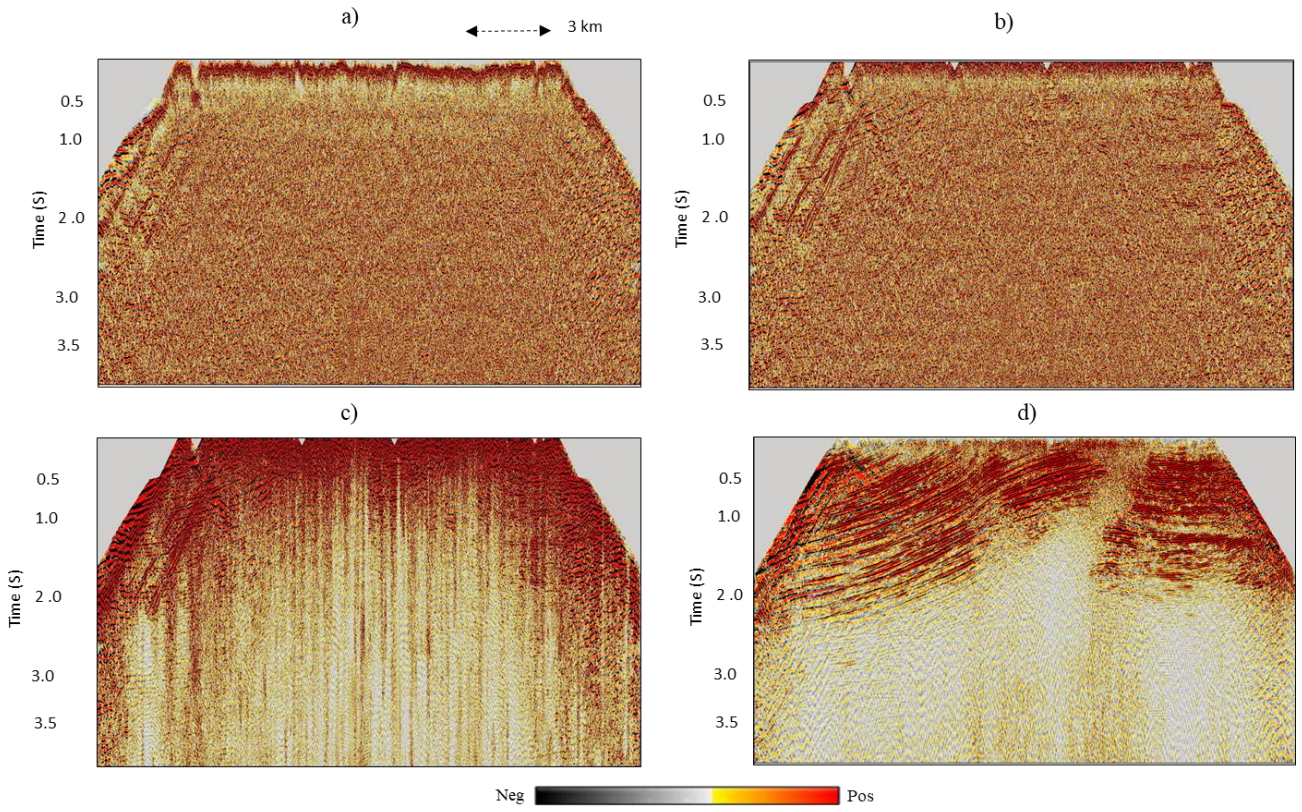

Figure 17. A comparison of stacks at various processing stages, **(a)** brute stack with field statics applied, **(b**) brute stack with refraction statics applied, **(c)** stack after initial denoising and first-pass velocity analysis and, **(d)** stack after applying surface-consistent deconvolution and residual statics with finer velocity analysis.

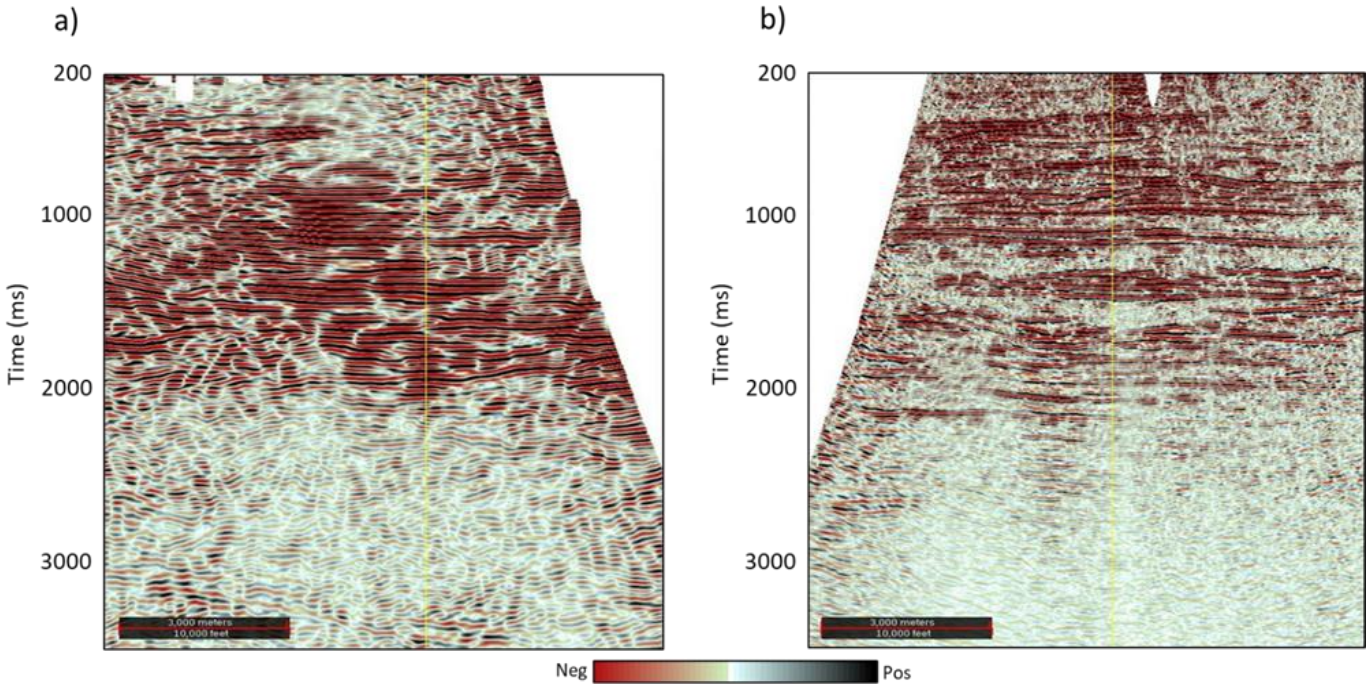

Figure 18. Comparison of 2D seismic profile segments from **(a)** vintage data, and **(b**) swath-line data. The segments have been included from only the overlap portions of the two profiles.

RESULTS

Significant enhancements have been observed in all nine swath line seismic data, particularly in the dip lines. The anticline features are now well-defined, showing clear fault boundaries and other reflectors. Additionally, the strike lines have been accurately resolved compared to the existing conventional 2D seismic data. A comparison of swath line data with vintage 2D is shown in (Figure 18**)**, the improvement in the signal-to-noise ratio by swath-line recording is markedly evident.

In order to compare the 2D swath-line geometry with conventional 2D geometry in the study area, we processed the swath-line data twice. In the first case, we utilized all three receiver lines, following the standard swath-line processing approach. In the second case, we focused solely on the central receiver line, resulting in a geometry resembling conventional 2D acquisition. All other parameters, including velocity, deconvolution operators, and migration parameters, remained consistent. The comparison of the final seismic stacks is presented in (Figures 19 and 20**)**, corresponding to the dip direction and strike direction, respectively. Notably, the swath-line processing with three receiver lines significantly improved image quality, particularly over fault zones near the anticlinal portion in the dip line. Additionally, events are clearly resolved in the strike direction.

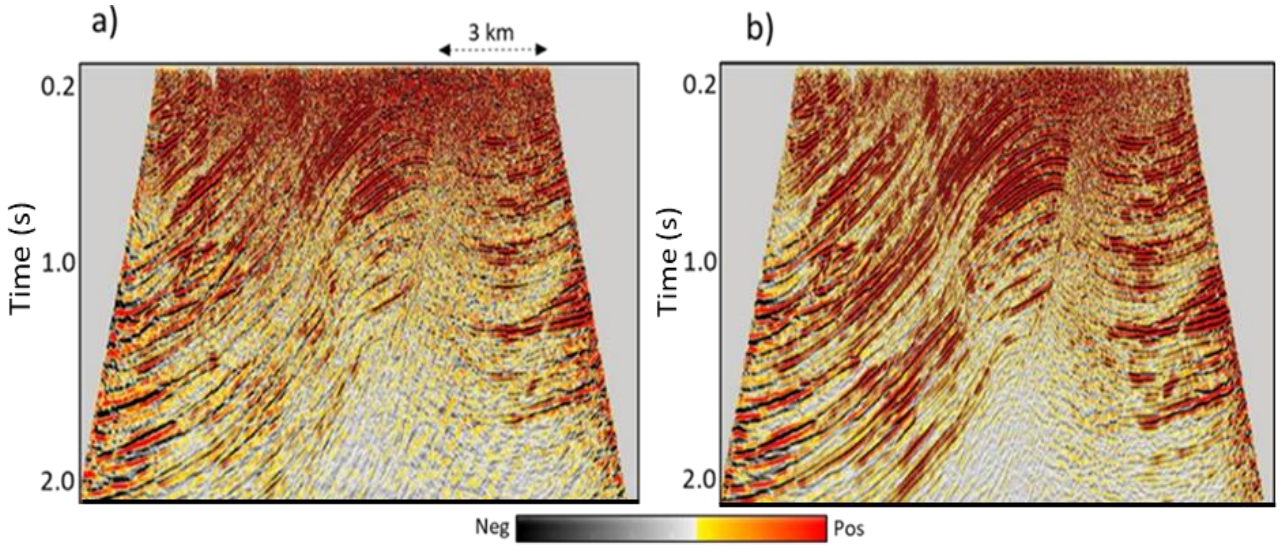

Figure 19. Comparison of stacked sections from swath-line, with **(a)** single receiver line, and **(b)** three receiver lines along dip direction. The image quality significantly improves, and faults are more distinct in **(b).**

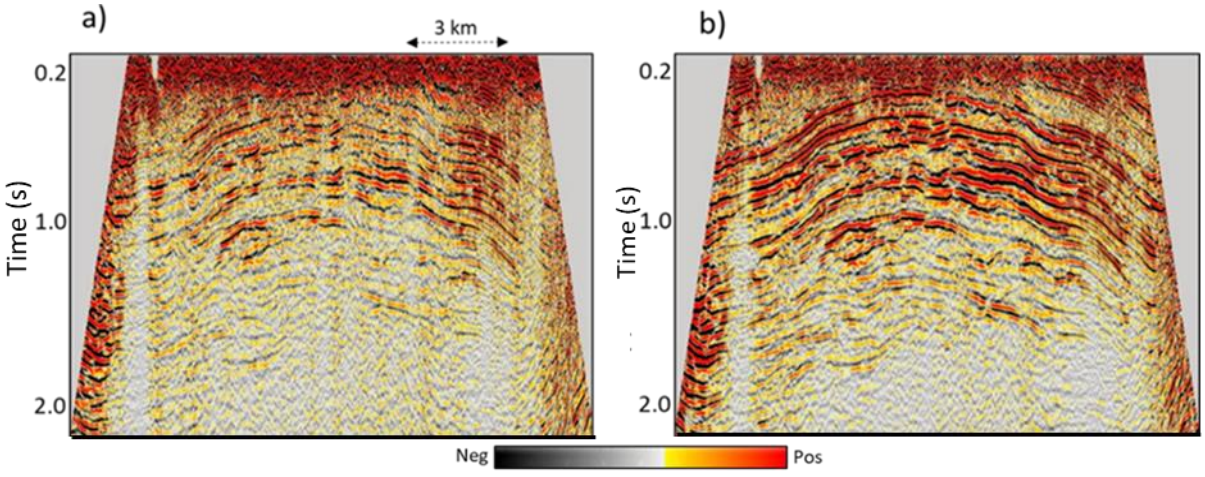

Figure 20. Comparison of stacked sections from swath-line with **(a)** single receiver line, and **(b)** three receiver lines along strike direction.

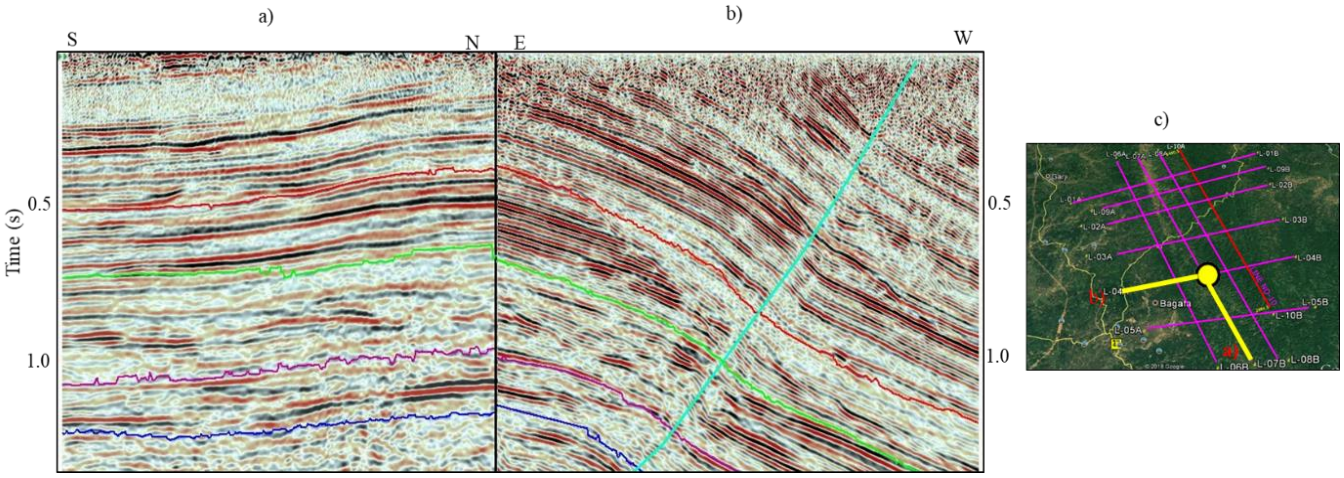

Figure 21. Interpreted RC line trough intersection of two swath lines, **(a)** section of a line along strike direction in N-S direction from intersection point, **(b)** section of a line along dip direction in E-W direction from intersection point, and **(c)** representation of lines on location map.

(Figure 21) illustrates an interpreted RC line derived from the intersections of a dip and strike line. Section **(a)** represents a line along the strike direction in the N-S direction, originating from the intersection point and section **(b)** corresponds to a line along the dip direction in the E-W direction, also starting from the intersection point. There is good match and continuity observed on the both sections at intersection point. While 2D swath line seismic data offers several advantages, it also comes with some limitations that we address during geometry planning. Due to the varying topography between receivers, especially in the strike direction of the anticline, swath line geometry often involves three receivers positioned at different elevations, which may fall into the same bin. When this elevation variation is more pronounced in the crossline direction, midpoints may coincide within the same bin during geometry merging. This arrangement occasionally results in smeared reflection events, leading to a low-frequency appearance in the output data. To address this limitation, it becomes necessary to maintain an optimal offset for the additional two receiver lines from the central line, especially when elevation variation is substantial in that direction (such as the lines parallel to the strike direction of the study area).

CONCLUSIONS

In areas with rough topography and difficult accessibility like Tripura fold belt, high-fold swath-line data acquisition proves more beneficial than conventional 2D land seismic methods. This is especially true when 3D land seismic data acquisition is cost-prohibitive. Treating swath-line data as 3D during most of the processing stages, including near-surface modelling and subsurface imaging, is crucial. Swath-line recording provides significantly higher foldage compared to typical 2D surveys, resulting in improved signal-to-noise ratios essential for imaging in fold belt areas. Addressing image quality issues related to geometry, statics, noise, velocity and algorithms, required a pragmatic approach. We employed a mix-and-match strategy, drawing from various software suites, recognizing that no single suite provides an optimal solution for all challenges.

ACKNOWLEDGEMENTS

The authors express their heartfelt gratitude to ONGC Ltd for their support and for providing the necessary facilities to carry out this work. They also appreciate the contributions of their colleagues at the Processing and Interpretation Centre of Assam and Assam-Arakan basin (A&AA Basin), Jorhat, for their insightful interactions and suggestions. It is important to note that the views expressed in this paper are solely those of the authors and may not necessarily reflect the perspective of their organization.

Authors contribution

The first author conceptualized, analysed, and processed the data. Manuscript review and correction were carried out by Uma Shankar and Yadunath Jha. Concept, corrections, and editing were done by Nani Madhab Dutta. All authors read and approved the final manuscript.

Data availability

The data used in this study is confidential and owned by ONGC Ltd., the geology and petroleum system of the area are freely accessible on the Directorate General of Hydrocarbons website (www.dghindia.gov.in).

Compliance with ethical standards

The author declares that they have no conflict of interest and adhere to copy right norms.

References

Bandyopadhyay, S., Saha, S., Ghosh, K. and De, S.K., 2013. Channel planform change and detachment of tributary: A study on the Haora and Katakhal Rivers, Tripura, India. Geomorphology, 193, 25-35.

Beasley, C. and Lynn, W., 1992. The zero-velocity layer: Migration from irregular surfaces. Geophysics, 57(11), 1435-1443.

Berryhill, J.R., 1979. Wave-equation datuming. Geophysics, 44(8), 1329-1344.

Bhartee, M.K., Dutta, N.M., Jha, Y. and Shankar, U., 2022. Improvement of structural imaging in fold belt area by swath-line seismic data acquisition. Geohorizons, 27(1), 51-59.

Brahma, J. and Sircar, A., 2018. Design of safe well on the top of Atharamura anticline, Tripura, India, on the basis of predicted pore pressure from seismic velocity data. J Petrol. Expl. Prod. Technol., 8, 1209–1224.

Chattopadhyay, T. and Ghosh, D.K., 2006. Structural Interpretation of Dipmeter Log – A Case Study from Baramura Field of Tripura. 6th International Conference & Exposition on Petroleum Geophysics, Kolkata-2006. 545-549.

Dasgupta, A.B. and Biswas, A.K., 2000. Geology of Assam: Geological Society of India. Bangalore, 169p.

Dutta, N.M., Sudhakar, M., Prasad, R.G., Basumatari, J.C. and Koch, S., 2015. Thrust Fold Belt Imaging issues and solutions: Cases from Assam and Assam Arakan fold belt. 11th Biennial International Conference & Exposition on Petroleum Geophysics, Jaipur.

Rajkhowa, M.M., Topno, H.P.A., Rajalingam, S., Phonglosa, V.R. and Shastri, V., 2018. Hydrocarbon Accumulation Pattern of Tura Formation in North Assam Shelf of Assam & Assam-Arakan Basin. APG India.

Samal, J.K., Srinivas, V., Naithani, A.C. and Harilal, 2017. Reservoir Characterisation in Complex Geological Set-up of Fold Thrust Belt: Case study from Manikyanagar Field of Rokhia Structure in Tripura Fold belt, India. SPG, Jaipur-2017. https://www.researchgate.net/publication/341755187

Yilmaz, O., 1987. Investigations in geophysics, no. 2: seismic data processing. Society of Exploration Geophysicists, Tulsa, OK.

Zhang, J. and Toksoz, M.N., 1998. Nonlinear refraction travel time tomography. Geophysics, 63(5), 1726-1737.

Zhu, T., Cheadle, S., Petrella, A. and Gray, S., 2000. First-arrival tomography: Method and application. 70th Ann. Int. Mtg. Soc. Expl. Geophys., 2028-2031.

Received on: 02-07-2024; Revised on: 13-01-2025 ; Accepted on: 14-01-2025

J. Ind. Geophys. Union, 29(2) (2025), 115-123
https://doi.org/10.71122/JIGU.29(2)2025.0012

Genesis of metastable marcasite phase and associated pyrite in the Proterozoic lamprophyre dyke, Nellore Schist Belt, Southern India

Tushar Meshram[1]* and Srinivasa Rao Baswani[2]
[1]Regional petrology laboratory, Geological Survey of India, Nagpur-440006, India
[2]Regional petrology laboratory, Geological Survey of India, Hyderabad-500068, India
*Corresponding Author: tusharmeshram2911@gmail.com

ABSTRACT

Marcasite is a metastable phase in iron-sulphide solution. If, preserved, it can be used as a significant indicator phase to understand the physio-chemical condition of its formation and associated sulphide system within ore deposits. The present study reports marcasite within the Proterozoic lamprophyre dyke, intruded into the amphibolite of Nellore Schist Belt, Southern India. Marcasite commonly occurs in association with pyrite, chalcopyrite and pyrrhotite in different textural associations. It shows development along the rim and fracture as an alteration of pyrrhotite at places forming characteristic bird eye structure. Pyrite forms later than marcasite, typically occurring along the boundary between marcasite and pyrrhotite. The formations of both marcasites followed by pyrite in the lamprophyre, suggest >l00 ºC and <240 ºC temperature, at low pH during the replacement of pyrrhotite through dissolution-reprecipitation-process under the influence of sulphur-rich hydrothermal solutions. However, the presence of both phases in different textural associations, reveals that the formation conditions of both the Fe sulphide phases i.e. pyrite and marcasite polymorphs are of neutral to alkaline solutions and have an influence on both hydrothermal as well as alkaline parental rock signatures.

Keywords: Pyrite, Marcasite, Pyrrhotite, Lamprophyre, Nellore Schist Belt, Dharwar craton.

INTRODUCTION

The two polymorphs of iron disulfide (FeS_2) are represented by pyrite (cubic) and marcasite (orthorhombic). Marcasite is metastable as compared to pyrite and formed by the alteration of a monosulfide phase like mackinawite or pyrrhotite. Marcasite formation is favoured by low pH on sulfur geochemistry (Goldhaber and Reynolds, 1979). The low-T weathering of pyrrhotite yields FeS_2 (pyrite and marcasite) with a typical replacement textures (especially bird's eye) (Ramdohr, 1975). The main loss of iron from pyrrhotite and its highly porous nature is responsible for its transformation into marcasite and pyrite (Kelley and Turneaure, 1970; Fleet, 1978). In contrast, marcasite to pyrite conversion occurs around 157 and 331°C Temp. at sulfur fugacities buffered and represented by the pyrite-pyrrhotite assemblage (Rising, 1973). Likewise, Qian et al. (2011) explained pyrrhotite to pyrite and marcasite replacement under low temperature (up to 220 °C) hydrothermal conditions. The recent experimental studies by Yao et al. (2020) and Yao (2021) reveal the fast conversion of marcasite to pyrite at higher-temp above 300 °C that restricted the presence of marcasite in the geological records. Although marcasite has a large range of temperatures from >300 ºC e.g. black smokers (Graham et al., 1988) to a lower range <160 ºC (Rising, 1973). Furthermore, the marcasite associated with the mineralization of supergene origin has below pH5 at 25ºC (Murowchick and Barnes, 1986). Likewise, several studies explain the formation of marcasite around temperatures ranging from 80°C to 350°C in various deposits (Barnes, 1979; Anderson and Macqueen, 1982; Ohmoto et al., 1983; Hayba et al., 1985). Especially, the gold is associated with viz-a-viz hosted by pyrite and marcasite (Cook and Chryssoulis, 1990; Large et al., 2007, 2016; Rickard and Luther, 2007; Deditius et al., 2014; Kusebauch et al., 2019; Wu et al., 2019; Xing et al., 2019) in hydrothermal deposits.

Nevertheless, intergrowth of pyrrhotite-pyrite-marcasite is also common in sedimentary settings (Ruppert et al., 2005; Schieber, 2007, 2011), associated with the epithermal system (Franchini et al., 2015; Rottier et al., 2016), Carlin as well as orogenic gold deposits (Fleet and Mumin, 1997; Cline, 2001; Teal and Jackson, 2002; Emsbo et al., 2003; Muntean et al., 2011; Soares et al., 2018; Stromberg et al., 2019), in supergene deposits (Petersen, 1965; Kelly and Turneaure, 1970; Nickel et al., 1974; Einaudi, et al., 2003), VHMS deposits (Maslennikov et al., 2013; Tessalina et al., 2017; Essaifi et al., 2019), and mineralization associated with hydrothermal vent in deep sea (Goldfarb, 1983; Koski et al., 1984; Hannington and Scott, 1987; Schoonen and Barnes, 1991*a*, *b*, *c*; Goldfarb et al., 2005). Its predominance is also reported from late-stage epithermal systems associated with hydrothermal breccias related mineralization e.g. Agua Rica deposit, Argentina (Franchini et al., 2015).

In neutral to alkaline solutions polysulfides are stable at <240°C (Giggenbach, 1974; Schoonen, 1989). Several studies have explained the presence of pyrite and marcasite under hydrothermal conditions (Schoonen and Barnes, 1991a,b,c; Murowchick, 1992; Qian et al., 2011), and supported marcasite formation under acidic conditions (pH <5), or in S(-II)-deficient solutions (saturation index << 1000 concerning either pyrite or marcasite). In contrast, pyrite generation is at relatively higher pH or S(-II)-rich solutions with saturation index >1000 (for either pyrite or marcasite) (Murowchick and Barnes, 1986; Qian et al., 2011). The occurrence of marcasite is a useful indicator of low-temperature environments

(Schoonen and Barnes, 1991a, b, c; Qian et al., 2011 and references therein).

In the present study, we discuss the mutual textural association of pyrrhotite, pyrite, and marcasite that occur in calc-alkaline lamprophyre intruded in the southern part of the Nellore Schist Belt. This lamprophyre is intruded by the minor quartz veins that generally carry sulfide mineralization. The lamprophyre dyke have developed under the influence of the hydrothermal system in the Nellore Schist Belt and the Eastern Dharwar Craton. Here, we present the formation of marcasite from the replacement of pyrrhotite in lamprophyre, to ascertain its role in the formation of base-metal mineralization in the area and its regional implication.

GEOLOGY OF THE AREA

The Dharwar Craton represented one of the prominent Archean cratons of the Indian shield located in southern India which can be divided into eastern Dharwar and western Dharwar cratons with the boundary demarcated by N-S trending Closepet granite. The eastern Dharwar Cratons is covered by the granite/gneisses/TTGs of Neoarchean age with the presence of NNW-SSE trending greenstone belts (Chadwick et al., 2000; Jayananda et al., 2000). The study area is located in the eastern Dharwar Cratons and close to the vicinity of the contact zone of Neoarchean Nellore Schist Belt and Eastern Ghats Belt. Nellore Schist Belt subdivided into Udayagiri and Vinjamuru groups, are situated juxtaposed to Nallamalai Fold belt and Cuddapah basin having thrust contact (Figure 1c) (Saha, 2011; Meshram et al., 2021, 2022). The Vinjamuru group predominantly contain metasedimentary rocks composed mainly of phyllites and quartzites along with the subordinate volcanics. Whereas, Udayagiri group is dominantly composed of amphibolite/meta-basalt.

The reported lamprophyre with sulfide mineralization is situated in the southern most extent of the NSB (Meshram et al., 2021, 2022) (Figure 1a-c). The studied lamprophyre is 2.3 Ga old, intruded into amphibolites of Udayagiri domain and it has taken part in the deformation and metamorphic processes associated with the Nellore Schist Belt (Figure 2a) (Meshram et al., 2021). It also exhibits late hydrothermal imprints represented by mineralized sulphide -rich quartz veins. There are number of quartz veins associated with sulfide mineralization which intruded along the Nellore Schist Belt (Figure 2b). The Garimanipenta, Venkatadripalem, Masayapeta and Tirumalapuram areas are well-known for potential sulphide mineralized occurrences along Nellore Schist Belt, which has been explored by the Geological Survey of India. This sulphide occurrence is situated almost 80 km north of the lamprophyre of the study area.

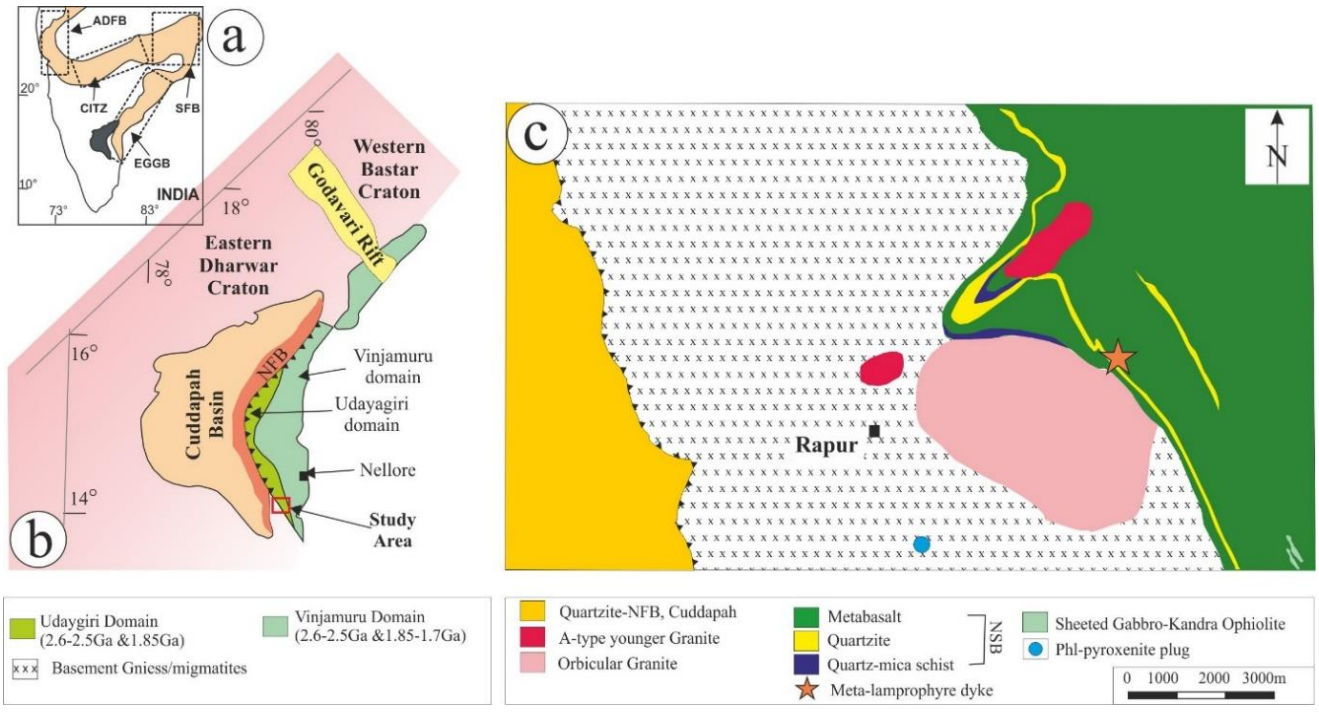

Figure 1. **(a)** Inset map of India showing location of Cuddapah basin. **(b)** Regional geological map showing location of study area in the Eastern Dharwar Craton and its relationship with the Cuddapah basin, Nellore Schist Belt and Nalamallai Fold Belt (NFB). **(c)** Study area showing the location of lamprophyre within Udayagiri meta-basalt (after Meshram et al., 2021, 2022).

PETROGRAPHICAL STUDY

The lamprophyre is foliated in nature and shows preferred orientation of amphibole and feldspar and secondary quartz along with sulphides (Figure 2b and Figure 3a,b). Detailed petrographical studies reveal the presence of primary porphyritic to panadiomorphic textures. The phenocryst phase is predominantly represented by phlogopite set in the fine-grained groundmass (Figure 3a,b). It contains principal sulphide minerals like pyrrhotite, marcasite, pyrite and chalcopyrite in association with silicates. The marcasite shows pale yellowish colour compared to pyrite and show anisotropism in shades of light yellow (Figure 3c-e). The marcasite veinlets have a thickness of a few cm, and occur in association with the pyrrhotite. It forms criss-cross veinlets, develops along fractures, and rims of the grain boundaries (Figure 3f). Pyrrhotite appears as grains up to a few centimeters in diameter, with all grains replaced by marcasite. Marcasite seams are consistently found along the borders of pyrrhotite grains. In some areas, pyrite occurs as euhedral grains up to a few millimeters in diameter, embedded within marcasite.The chalcopyrite grains in the lamprophyre do not show any alteration and sharp contact with both pyrrhotite and marcasite. Limonite/siderite of a reddish-brown colour is seen under transmitted light.

The replacement textures show development of remiform borders of marcasite, whereas, formation of tiny rounded to spheroids shapes with double marginal zone is more common and significant. A worm-like body of marcasite along pre-existing microfissures, such as cracks and cleavage planes in the original pyrrhotite, is also observed. At places, a series of concentric layers of marcasite (bird's-eye structures, (Figure 3e, f), are separated from each other by open voids, and finally the whole pyrrhotite grain is transformed to marcasite. Pyrrhotite is showing skeletal texture due to the replacement of entire grains by marcasite.

MINERAL CHEMISTRY OF PYRRHOTITE, CHALCOPYRITE AND PYRITE

A total of 28 EPMA spot analyses were carried out, on the pyrrhotite 12 numbers (nos.), chalcopyrite 06 nos., marcasite 05 nos. and pyrite 05 nos. The instrument was set under 15 kV accelerating voltage, one μm beam diameter, and 20 nA beam current for the measurements. The counting times for peak and background were the 40 s and 20 s, respectively. The precisions of the analyses were ±0.5% element concentrations. The ZAF matrix corrections were carried out using the CAMECA supplied Peak sight program. The major element compositions are listed in Tables 1-3. The general representation is shown in the binary plot S against Cu+Fe in Figure 4a and also plotted Fe and S variation in box plot (Figure 4b). They show systematic variation in copper, iron and sulphur.

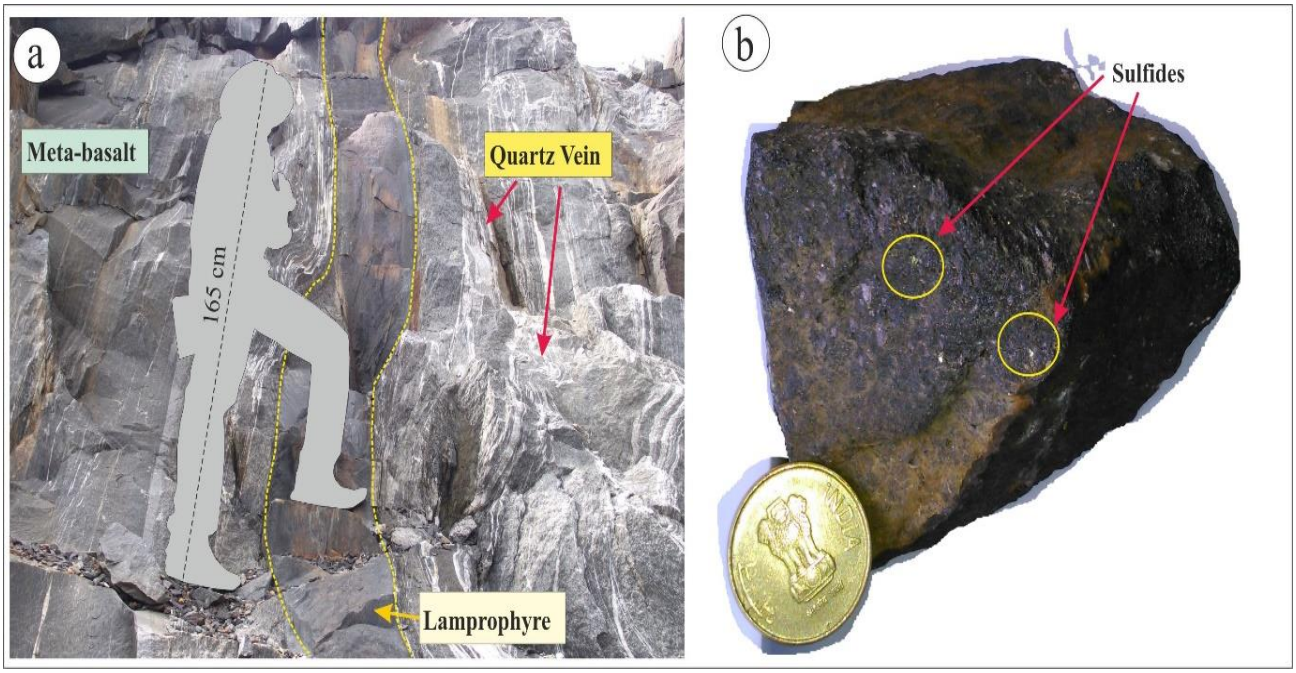

Figure 2. (a) Field photograph showing the lamprophyre intruded within Udayagiri meta-basalt, Note-extensive intrusion of intense quartz veining parallel to the lamprophyre intrusion. **(b)** Close-up view photograph showing porphyritic texture in lamprophyre with the presence of sulfide mineralization (Location: quarry section west of Rapuru near Gilakapadu area)

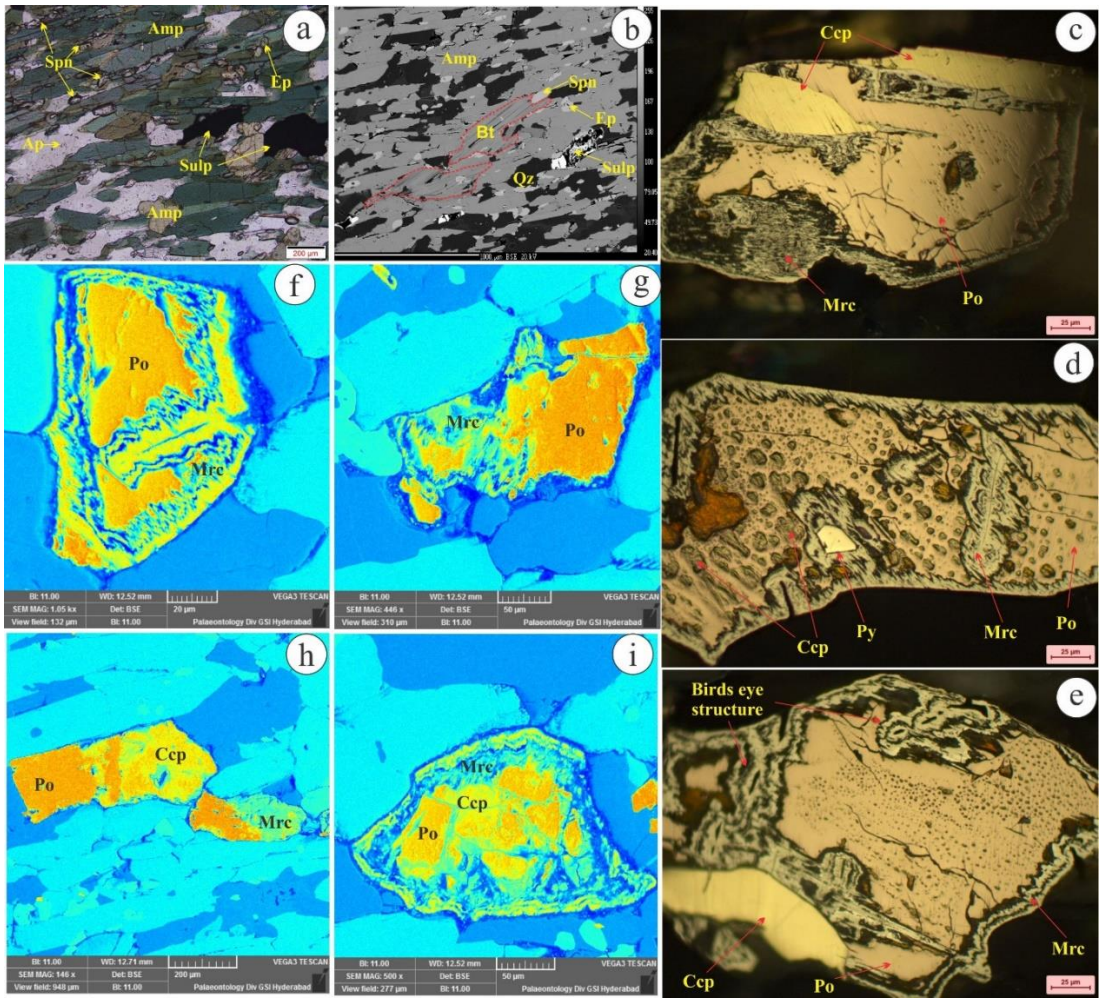

Figure 3. **(a)** Photomicrograph showing presence of sulphide along the foliation plane within lamprophyre; note- alignment of amphibole defining foliation. **(b)** Back scattered electron image showing presence of sulphide and its replacement within lamprophyre. **(c)** Photomicrograph showing replacement of pyrrhotite with the marcasite and formation of chalcopyrite. **(d)** Photomicrograph showing replacement of pyrrhotite to marcasite and formation of chalcopyrite as inclusion along with late phase pyrite. **(e)** Photomicrograph showing replacement of pyrrhotite to marcasite with development of characteristic birds eye structure. **(f-i)** False color composite images illustrate the various textural associations of pyrrhotite replacement by marcasite, along with the formation of chalcopyrite and pyrite.

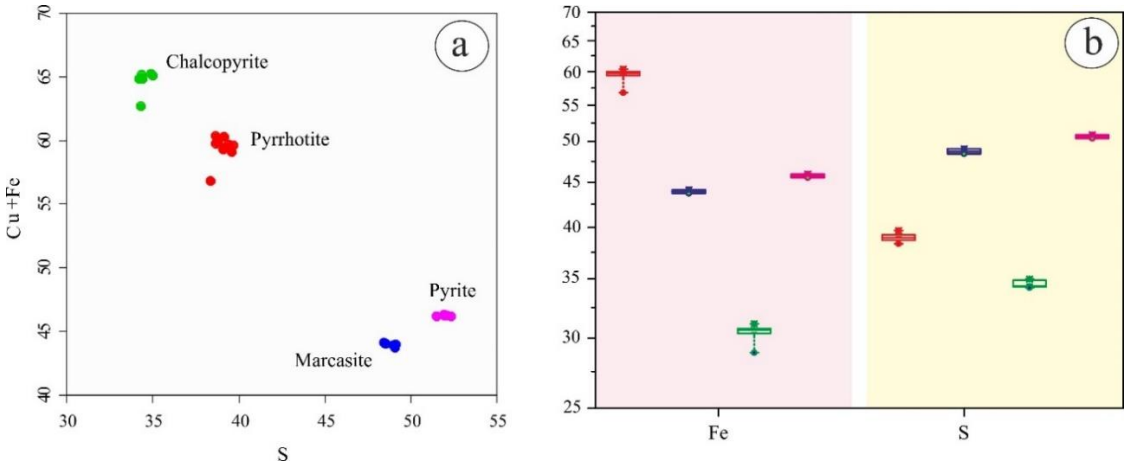

Figure 4. **(a)** Binary variation plot of S against Cu+Fe. **(b)** box plot for pyrite-chalcopyrite-pyrrhotite and marcasite show behaviour of Fe and S.

In general, pyrrhotite contains 56.78–60.63 wt% Fe (average 59.51 wt%), 38.33–39.68 wt% S (average 38.99 wt%), with higher concentrations of Ni, Co, and Mo, while the remaining elements are below detection limits. Chalcopyrite has 28.89–31.13 wt% Fe (average 30.40 wt%), 34.20–34.98 wt% S (average 34.51 wt%), and 33.81–34.45 wt% Cu (average 34.25 wt%), with higher levels of Mo and the remaining elements below detection limits. Pyrite shows 46.09–46.31 wt% Fe (average 46.20 wt%), 51.10–51.94 wt% S (average 51.45 wt%), and 0.009–0.076 wt% Cu, with other elements either insignificant or below detection limits. Marcasite contains 43.71–44.11 wt% Fe and 48.43–49.07 wt% S, with higher concentrations of Ni, Co, and Mo, while the remaining elements are below detection limits.

Table 1. Representative EPMA analysis of Pyrrhotite from meta-lamprophyre dyke.

Point	1 / 1	2 / 1	3 / 1	6 / 1	7 / 1	9 / 1	11 / 1	12 / 1	13 / 1	15 / 1	16 / 1	20 / 1
	Pyrrhotite											
Cu	0.037	0	0.101	0.029	0	0	0.021	0.003	0	0	0	0.042
Co	0.258	0.245	0.27	0.256	0.237	0.22	0.265	0.266	0.25	0.22	0.215	0.25
Ni	0.176	0.212	0.231	0.153	0.233	0.246	0.27	0.19	0.262	0.212	0.198	0.217
Fe	59.982	59.863	59.608	56.789	59.11	59.989	59.263	59.625	60.304	59.765	59.462	60.363
Zn	0	0	0	0	0	0.172	0	0.025	0	0.012	0	0.01
S	38.758	38.796	39.38	38.332	39.579	38.771	39.093	39.685	39.134	38.645	39.123	38.65
Te	0.037	0.022	0	0.01	0	0	0	0	0.048	0.036	0.012	0
Au	0	0	0	0	0	0	0	0	0	0	0	0
Mo	0.54	0.636	0.532	0.424	0.643	0.501	0.727	0.681	0.657	0.649	0.661	0.489
Bi	0.143	0.029	0.056	0.279	0.131	0.175	0.051	0.135	0.277	0.086	0.191	0.21
Se	0.013	0.007	0	0.048	0.039	0.003	0.013	0	0	0.015	0.051	0.002
Ag	0.001	0	0	0.031	0	0	0.039	0.026	0	0.035	0	0
Sb	0	0	0	0	0	0	0	0	0	0	0	0
Sn	0	0.042	0.044	0.031	0	0.07	0.029	0.055	0.05	0.01	0.141	0.055
Pb	0.14	0.218	0.097	0.055	0.133	0.266	0.101	0.127	0.062	0.188	0.26	0.153
As	0	0	0	0	0	0	0	0	0	0	0	0.017
Total	100.086	100.07	100.319	96.439	100.104	100.413	99.872	100.817	101.044	99.874	100.314	100.458

Table 2. Representative EPMA analysis of Chalcopyrite from meta-lamprophyre dyke.

Point	4 / 1	5 / 1	8 / 1	10 / 1	18 / 1	19 / 1
	Chalcopyrite					
Cu	34.373	33.813	34.423	34.452	34.1	34.353
Co	0.1	0	0.013	0.017	0.035	0.019
Ni	0	0.039	0	0.008	0.013	0.012
Fe	30.514	28.891	30.749	30.378	31.139	30.756
Zn	0	0.083	0.039	0	0	0.075
S	34.204	34.278	34.34	34.402	34.894	34.98
Te	0.029	0	0	0	0	0
Au	0	0	0	0	0	0
Mo	0.695	0.437	0.587	0.74	0.614	0.621
Bi	0.256	0.024	0.022	0.02	0.142	0.337
Se	0	0.01	0	0.104	0	0
Ag	0	0	0	0	0.078	0
Sb	0	0	0	0	0	0
Sn	0	0.018	0	0.054	0.034	0
Pb	0	0.296	0.141	0.188	0.258	0.083
As	0	0	0	0	0	0
Total	100.172	97.89	100.315	100.363	101.307	101.235

Table 3. Representative EPMA analysis of Marcasite and pyrite from meta-lamprophyre dyke**.**

Point	14 / 1	15 / 1	16 / 1	17 / 1	17 / 1	1 / 1	2 / 1	3 / 1	6 / 1	7 / 1
	Marcasite					Pyrite				
Cu	0	0	0	0	0	0.076	0.024	0.009	0.032	0.029
Co	0.388	0.295	0.312	0.376	0.423	0.034	0.076	0.025	0.044	0.081
Ni	0.765	0.798	0.894	0.889	1.052	0.047	0.021	0.016	0	0.021
Fe	43.714	43.961	43.887	44.065	44.118	46.09	46.22	46.23	46.15	46.31
Zn	0.05	0.031	0	0.045	0	0	0.032	0	0.027	0
S	49.078	49.12	48.976	48.538	48.438	51.48	52.1	51.92	52.32	51.94
Te	0.008	0.005	0	0.006	0	0.024	0	0.083	0	0
Au	0	0	0	0	0	0.009	0	0	0	0
Mo	0.84	0.81	0.79	0.812	0.826	0	0	0	0	0
Bi	0.241	0	0	0	0	0	0	0	0	0
Se	0.036	0.028	0.007	0.031	0.005	0	0	0	0	0
Ag	0	0	0	0	0	0	0.014	0	0.015	0.002
Sb	0	0	0	0	0	0	0	0	0	0
Sn	0.085	0.083	0.057	0.064	0.066	0	0	0	0	0
Pb	0.044	0.03	0.078	0.041	0.304	0	0	0	0	0
As	0	0	0	0	0	0	0	0.006	0	0
Total	95.25	95.161	95.001	94.867	95.233	97.76	98.487	98.289	98.588	98.383

DISCUSSION

Conditions of formation of marcasite

The pyrrhotite-marcasite transformation is common in the supergene zone and association of secondary pyrite with the marcasite may point to higher confining pressures during the transformation process, or to the direct precipitation of pyrite from solution under conditions of high Fe and S activity (Schoonen and Barnes, 1991a,b,c). The transformation of pyrrhotite to marcasite with the presence of chalcopyrite in alkaline rocks in southern India is akin to many ore deposits (e.g., Einaudi, 1971; Fleet, 1970, 1978). The pyrrhotite transformation to marcasite and/or pyrite, also develops large porosity (Murowchick, 1992). Distinct replacement textures of pyrrhotite conversion to either pyrite or marcasite are ilustarted in (Figure 3). During the evolution of solution, the overgrowth and formation of marcasite happened by direct viz-a-viz simultaneous pyrrhotite conversion and their association chalcopyrite reveals the crystal growth of marcasite as a precipitation mechanism from same solution.

The experimental study of Qian et al. (2011) suggested that the pyrrhotite to Fe disulfide reaction supports the dissolution-reprecipitation mechanism under hydrothermal conditions and temperature below 220ºC preferentially at low pH. Schoonen and Barnes (1991a,b,c)'s experimental studies suggest that at < l00ºC, pyrite and marcasite are formed by sulfidation of FeS with polysulfides, and > l00ºC, they are formed via sulfidation with the loss of iron and release of earlier FeS phases. They are only stable in neutral to alkaline solutions < 240°C (Giggenbach, 1974; Schoonen, 1989). The formation of both phases under hydrothermal conditions suggests its genesis in acidic conditions (pH<5), or in S(-II)-deficient solutions while pyrite is formed at relatively higher pH or S(-II)-rich solutions (Murowchick and Barnes, 1986; Schoonen and Barnes, 1991a, b, c; Murowchick, 1992; Qian et al., 2011). Experimental study of Yao (2021) has shown rapid transformation from marcasite to pyrite at higher temperatures (>300 ºC).

It is obvious that the formation of marcasite in alkaline rocks is the replacement of pyrhotite by dissolution-reprecipitation mechanism under hydrothermal conditions and also by enrichment of sulphur from solution through sulfidation processes progressively more sulphur-rich phases pyrite and chalcopyrite. Therefore, the temperature ranges of formations of marcasite in the alkaline rocks are above l00ºC and below 220ºC and replacement of pyrrhotite through dissolution-reprecipitation process under the influence of sulphur rich hydrothermal solutions. In the present study, it is observed that the formation of both pyrite and marcasite indicate similar conditions. However, the presence of both phases in different textural associations reveal that the formational conditions for them are of mixed nature and have the influence of both hydrothermal as well as alkaline parental rock signature. The mineral typically forms under low-temperature, sulfur-rich conditions, often associated with hydrothermal fluids that interact with the host rock. The alkaline environment plays a crucial role in stabilizing marcasite, facilitating its precipitation from the circulating fluids. These fluids, rich in sulfur, promote the replacement of pyrrhotite and other minerals, allowing

marcasite to crystallize in fractures and intergranular spaces. This process often occurs in proximity to base metal mineralization, further indicating the influence of the hydrothermal system in the formation of marcasite.

CONCLUSIONS

The Nellore Schist Belt hosts potential base metal sulphide occurrences along its southern extension. Present study reported the marcasite within the lamprophyre dyke intruded into the amphibolite of Nellore Schist Belt, Rapuru, India. Marcasite commonly occurrs in association with pyrite, chalcopyrite, pyrrhotite in different textural association. Marcasite is metastable phase in iron-sulphide solution significantly used as an indicator phase to understand the physio-chemical conditions of sulphide system associated with ore deposits. The textural evidence shows its development along the rim and fractures as an alteration of pyrrhotite with characteristic bird eye structure. Mutual association of marcasite-pyrite in the lamprophyre is generally restricted to <240ºC temperature, neutral to alkaline solutions at low pH during dissolution-reprecipitation process under the influence of sulphur rich hydrothermal solutions.

Acknowledgement

Authors extend sincere thanks to the Additional Director General, Geological Survey of India, Southern Region Hyderabad for providing the necessary facilities during filed season programme. We are thankful to the Additional Director General, Geological Survey of India, Central Region for according permission to publish this work. The authors also extend their sincere gratitude to an anonymous reviewers for critical scrutiny and constructive suggestions, which immensely helped to improve the manuscript. Finally, the authors are thankful to the Chief Editor for providing an opportunity and kind consideration of our research in the journal.

Author Credit Statement

Tushar Meshram: Conceptualization, field investigation, writing original draft, review and editing. Srinivasa Rao Baswani**:** Conceptualization, field investigation, formal analysis, writing, review and editing

Data availability

All data generated or analysed during this study are included in this article.

Compliance with ethical standards

No conflict of interest and the authors declare that they have no known competing financial interests or personal relationships that could have appeared to influence the work reported in this paper. Adhere to the copyright norms

References

Anderson, G.M. and Macqueen, R. W., 1982. Mississippi Valley type lead-zinc deposits. Geoscience Canada, 9, 108-l17.

Barnes, H.L., 1979. Solubility of ore minerals. Geochemistry of Hydrothermal Ore Deposits, J. Wiley & Sons, 404-454.

Chadwick, B., Vasudev, V.N. and Hegde, G.V., 2000. The Dharwar craton, southern India, interpreted as the result of Late Archean oblique convergence. Precamb. Res., 99, 91–111.

Cline, J.S., 2001. Timing of gold and arsenic sulfide mineral deposition at the Getchell Carlin-type gold deposit, north-central Nevada. Economic Geol., 96(1), 75-89.

Cook, N.J. and Chryssoulis, S.L., 1990. Concentrations of invisible gold in the common sulfides. Canadian Mineral., 28, 1-16.

Deditius, A.P., Reich, M., Kesler, S.E., Utsunomiya, S., Chryssoulis, S.L., Walshe, J. and Ewing, R.C., 2014. The coupled geochemistry of Au and As in pyrite from hydrothermal ore deposits. Geochim. Cosmochim. Acta, 140, 644-670.

Emsbo, P., Hofstra, A.H., Lauha, E.A., Griffin, G.L. and Hutchinson, R.W., 2003. Origin of high-grade gold ore, source of ore fluid components, and genesis of the Meikle and neighbouring Carlin type deposits, northern Carlin trend, Nevada. Economic Geol., 98(6), 1069-1105.

Einaudi, M.T., 1971. The intermediate product of pyrrhotite alteration. American Mineral., 56, 1297–1302

Einaudi, M. T., Hedenquist, J.W. and Inan, E.E., 2003. Sulfidation state of fluids in active and extinct hydrothermal systems: Transitions from porphyry to epithermal environments. Special Publication-Society of Economic Geologists, 10, 285-314.

Essaifi, A., Goodenough, K., Tornos, F., Outigua, A., Ouadjou, A. and Maacha, L., 2019. The Moroccan Massive Sulphide Deposits: Evidence for a Polyphase Mineralization. Minerals, 9(3), 156.

Fleet, M.E. 1970. Structural aspects of the marcasite-pyrite transformation. Canadian Mineral., 10, 225-231.

Fleet, M.E. 1978. The pyrrhotite-marcasite transformation: Canadian Mineral., 16, 31-35.

Fleet, M.E., Mumin, A.H. 1997. Gold-bearing arsenian pyrite and marcasite and arsenopyrite from Carlin Trend gold deposits and laboratory synthesis. American Mineral., 82(1-2), 182-193.

Franchini, M., McFarlane, C., Maydagán, L., Reich, M., Lentz, D. R., Meinert, L. and Bouhier, V., 2015. Trace metals in pyrite and marcasite from the Agua Rica porphyry-high sulfidation epithermal deposit, Catamarca, Argentina: Textural features and metal zoning at the porphyry to epithermal transition. Ore Geol. Rev., 66, 366-387.

Giggenbach, W.F. 1974. Equilibrium involving polysulfide ions in aqueous solutions up to 240°C. Inorganic Chem., 13, 1724-1730.

Goldfarb, M.S., 1983. The genesis of hot spring deposits on the East Pacific Rise 21ºN. The Kuroko and Related Volcanogenetic Massive Deposits. Economic Geology, Monograph 5, 184-197.

Goldfarb, R., Baker, T., Dubé, B., Groves, D.I., Hart, C.J. and Gosselin, P., 2005. Distribution, character and genesis of gold deposits in metamorphic terranes. Society of Economic

Geologists, Economic Geology One Hundredth Anniversary Volume, 407-450.

Goldhaber, M.B. and Reynolds, R.L., 1979. Origin of marcasite and its implications regarding the genesis of roll-front uranium deposits. U.S. Geol. Surv. Standard Report, 1-40.

Graham, U.M., Bluth, G.J., Ohmoto, H., 1988. Sulfide sulfate chimneys on the East Pacific Rise, 11° and 13°N latitudes. Part I: Mineralogy and paragenesis. Canadian Mineral., 26, 487-504.

Hannington, M.D. and Scott, S.D., 1987. Sulfidation equilibria as guides to gold mineralization in volcanogenic massive sulfides. Geol. Soc. America, Abstract 19, 692.

Hayba, D.O., Bethke, P.M., Heald, P. and Foley, N.K., 1985. Geologic, mineralogic, and geochemical characteristics of volcanohosted epithermal precious-metal sulfide deposits. Review in Economic Geology 2, 129-162.

Jayananda, M., Moyen, J.F., Martin, H., Peucat, J.J., Auvray, B. and Mahabaleshwar, B., 2000. Late Archean (2550–2520 Ma) juvenile magmatism in the Eastern Dharwar craton, southern India: constraints from geochronology, Nd–Sr isotopes and whole-rock geochemistry. Precamb. Res., 99, 225–254.

Kelly, W.C. and Turneaure, F.S., 1970. Mineralogy, paragenesis and geothermometry of the tin and tungsten deposits of the eastern Andes, Bolivia. Economic Geol., 65(6), 609-680.

Koski, R.A., Clague, D.A. and Oudin, E., 1984. Mineralogy and chemistry of massive sulfide deposits from the Juan de Fuca Ridge. Geol. Soc.America Bull., 95(8), 930-945.

Kusebauch, C., Gleeson, S.A. Oelze, M., 2019. Coupled partitioning of Au and As into pyrite controls formation of giant Au deposits. Science Advances, 5(5), 1-8.

Large, R.R., Maslennikov, V.V., Robert, F., Danyushevsky, L.V. and Chang, Z., 2007. Multistage sedimentary and metamorphic origin of pyrite and gold in the giant Sukhoi Log deposit, Lena gold province, Russia. Economic Geol., 102(7), 1233-1267.

Large, S.J., Bakker, E.Y., Weis, P., Wälle, M., Ressel, M. and Heinrich, C.A., 2016. Trace elements in fluid inclusions of sediment-hosted gold deposits indicate a magmatic-hydrothermal origin of the Carlin ore trend. Geology, 44(12), 1015-1018.

Maslennikov, V.V., Masslennikova, S.P., Large, R.R., Danyushevsky, L.V., Herrington, R.J. and Stanley, C.J., 2013. Tellurium-bearing minerals in zoned sulfide chimneys from Cu-Zn massive sulfide deposits of the Urals, Russia. Mineral. and Petrol., 107, 67-99.

Meshram, T., Mahapatro, S.N., Aravind, J.K., Dora, M.L., Baswani, S.R., Gopalakrishna, G., Meshram, R., Sesha Sai, V.V., Randive, K. and Das, J., 2021. Geochemistry and Sr-Nd isotopic studies of Palaeoproterozoic (ca. 2.3 Ga) meta-lamprophyre from Rapuru area, Nellore Schist Belt, Southern India: implication for back-arc basin magmatism and its relevance to the Columbia Supercontinent assembly. Geol. Soc. London, Special Publications, 513, 103-132.

Meshram, T., Mahapatro, S.N., Sesha Sai, V.V., Dora, M.L., Randive, K. and Baswani, S.R., 2022. Petrogenesis of phlogopite-pyroxenite from Southern India: implications for the link between Proterozoic subduction- to rift-related arc magmatism. Geosyst. Geoenviron., Volume 1, article id. 100033., DOI: 10.1016/j.geogeo.2022.100033

Muntean, J.L., Cline, J.S., Simon, A.C. and Longo, A.A., 2011. Magmatic–hydrothermal origin of Nevada's Carlin-type gold deposits. Nature Geosci., 4(2), 122.

Murowchick, J.B., 1992. Marcasite inversion and the petrographic determination of pyrite ancestry. Economic Geol., 87, 1141–1152.

Murowchick, J.B. and Barnes, H.L., 1986. Marcasite precipitation from hydrothermal solutions. Geochim. Cosmochim. Acta, 50, 2615-2630.

Nickel, E.H., Ross, J.R. and Thornber, M.R., 1974. The supergene alteration of pyrrhotite pentlandite ore at Kambalda, Western Australia. Economic Geol., 69(1), 93-107.

Ohmoto, H., Mizukami, M., Drummond, S.E., Eldridge, C.S., Pisutha-Arnond, V. and Lenagh, T.C., 1983. Chemical processes of Kuroko formation. In Economic Geology Monograph Series, 5, 570-604.

Petersen, U., 1965. Regional geology and major ore deposits of central Peru. Economic Geol., 60(3), 407-476.

Qian, G., Xia, F., Brugger, J., Skinner, W.M., Bei, J., Chen, G. and Pring, A., 2011. Replacement of pyrrhotite by pyrite and marcasite under hydrothermal conditions up to 220 ℃: An experimental study of reaction textures and mechanisms. American Mineral., 96(11-12), 1878-1893.

Ramdohr, P., 1975. Der erz Mineralien und ihre Verwachsungen: Berlin, Acdemic-Verlag, 173.

Rickard, D. and Luther, G.W., 2007. Chemistry of iron sulfides. Chem. Rev., 107,514-562.

Rising, B.A., 1973. Phase relations among pyrite, marcasite, and pyrrhorite below 300 ℃, Ph.D. thesis, Pennsylvania State University, University Park, Pennsylvania, United State,192p.

Rottier, B., Kouzmanov, K., Wälle, M., Bendezú, R. andFontboté, L., 2016. Sulfide replacement processes revealed by textural and LA-ICP-MS trace element analyses: example from the early mineralization stages at Cerro de Pasco, Peru. Economic Geol., 111(6), 1347-1367.

Ruppert, L.F., Hower, J.C. and Eble, C.F., 2005. Arsenic-bearing pyrite and marcasite in the Fire Clay coal bed, Middle Pennsylvanian Breathitt Formation, eastern Kentucky. Int. J. Coal Geol., 63(1-2), 27-35.

Saha, D., 2011. Dismembered ophiolites in Paleoproterozoic nappe complexes of Kandra and Gurramkonda, South India. J. Asian Earth Sci., 42, 158–175.

Schieber, J., 2007. Oxidation of detrital pyrite as a cause for Marcasite Formation in marine lag deposits from the Devonian of the eastern US. Deep-Sea Res., 54, 1312-1326.

Schieber, J., 2011. Marcasite in black shales - A mineral proxy for oxygenated bottom waters and intermittent oxidation of carbonaceous muds. J. Sediment Res., 81(7), 447-458.

Schoonen, M.A.A., 1989. Mechanisms of pyrite and marcasite formation from solutions between 25 and 300°C. Ph.D. dissertation, Pennsylvania State University, United States, 54-161

Schoonen, M.A.A. and Barnes, H. L., 1991a. Mechanisms of pyrite and marcasite formation from solution: III. Hydrothermal processes. Geochim. Cosmochim. Acta, 55(12), 3491-3504.

Schoonen, M.A.A. and Barnes, H.L., 1991b. Reactions forming pyrite and marcasite from solution: I. Nucleation of FeS_2 below 100 ºC. Geochim. Cosmochim. Acta, 55(6), 1495-1504.

Schoonen, M.A.A. and Barnes, H. L., 1991c. Reactions forming pyrite and marcasite from solution:II. Via FeS precursors below 100 ℃. Geochim. Cosmochim. Acta, 55(6), 1505-1514.

Soares, M.B., Neto, A.V.C., Bertolino, L.C., Alves, F.E.A., de Almeida, A.M., da Silva, P.H.M., de Araujo Mabub, R.O., Manduca, L.G. and de Pamplona Araújo, I.M.C., 2018. Multistage mineralization at the hypozonal São Sebastião gold deposit, Pitangui greenstone belt, Minas Gerais, Brazil. Ore Geol. Rev., 102, 618-638

Stromberg, J.M., Barr, E., Van Loon, L.L., Gordon, R.A. and Banerjee, N.R., 2019. Fingerprinting multiple gold mineralization events at the Dome mine in Timmins, Ontario, Canada: Trace element and gold content of pyrite. Ore Geol. Rev., 104, 603-619.

Teal, L. and Jackson, M., 2002. Geologic overview of the Carlin trend gold deposits. Gold deposits of the Carlin trend. Nevada Bureau of Mines and Geology, Society of Economic Geologists, Bull., 111, 9-19.

Tessalina, S.G., Jurdan, F. and Belogub, E.V., 2017. Significance of Late Devonian-Lower Carboniferous ages of hydrothermal suphides and sericites from the Urals Volcanic-Hosted Massive Sulphide deposits. Ore Geol. Rev., 85, 131-139.

Wu, Y.F., Evans, K., Li, J.W., Fougerouse, D., Large, R.R. and Guagliardo, P., 2019. Metal remobilization and ore-fluid perturbation during episodic replacement of auriferous pyrite from an epizonal orogenic gold deposit. Geochim. Cosmochim. Acta, 245, 98-117.

Xing, Y., Brugger, J., Tomkins, A. and Shvarov, Y., 2019. Arsenic evolution as a tool for understanding formation of pyritic gold ores. Geology, 47(4), 335-338.

Yao, X. 2021 Experimental studies on the formation of pyrite and marcasite and the mechanisms of arsenic Incorporation. Ph.D. thesis, Murdoch University, Perth, Australia.

Yao, X., Xia, F., Deditius, A.P., Brugger, J., Etschmann, B.E., Pearce, M.A. and Pring, A., 2020. The mechanism and kinetics of the transformation from marcasite to pyrite: in situ and ex situ experiments and geological implications. Contr. Mineralogy and Petrology, 175(3), 1-25

Received on: 24-09-2024; Revised on: 10-03-2025 ; Accepted on: 12-03-2025

J. Ind. Geophys. Union, 29(2) (2025), 124-131
https://doi.org/10.71122/JIGU.29(2)2025.0013

2024 Mulugu Earthquake: Reactivation of a deep-seated crustal fault in Godavari Graben (India)

A. Vasanthi

CSIR-National Geophysical Research Institute
Hyderabad-500007, India.
E-mail: vasanthi@ngri.res.in; vasanthi99ngri@gmail.com

ABSTRACT

Indian subcontinent has been experiencing intraplate seismicity since historical times having witnessed a number of damaging earthquakes. Recently, on December 4, 2024, Godavari graben was rocked by a moderate earthquake (M=5.0) close to Mulugu town in Telangana state of India. It has a focal depth of around 10 km. Earlier too, this graben has experienced a number of moderate-magnitude destructive earthquakes. We have analyzed high-resolution satellite gravity data over this region in order to identify the active faults and genesis of this intraplate earthquake. The residual gravity anomaly, deduced using Finite Element Method, brought-out a clear expression over different geologic and tectonic features. Eastern flank of Godavari graben is seen to be characterized by extremely high-gradient gravity anomalies corresponding to a deep-seated crustal-level fault, over which the hypocenter of the Mulugu earthquake lies. Similarly, western flank is also associated with high gravity gradients, corresponding to a fault structure which also reaches to mid-crustal depth. These seismogenic faults are getting reactivated due to neo-tectonic activities caused possibly by underlying thermal anomaly. It appears that all the major intra-plate earthquakes of Indian shield have occurred along the prominent rift structures, which are associated with high heat flow and thin lithosphere, and have undergone quaternary uplifting and crust-mantle thermal interaction.

Key Words: Intraplate seismicity, Deep-seated crustal fault, Godavari graben, Mulugu earthquake; Gravity field; FEM (Finite Element Method); Heat flow.

INTRODUCTION

Some of the Stable Continental Regions (SCR) have been experiencing moderate to large intraplate seismic activity since historical times. Indian subcontinent is one of the finest examples. It has a dynamic past of active rifting, and has undergone multiple plume interaction and continuous uplifting. During the last 50 years, it has witnessed more than 20 events of magnitude five and above, many of which have been destructive and led to the loss of human life and property. This includes, 1819 Kachchh (M=7.7), 1927 Son-valley (M=6.4), 1967 Koyna (M=6.3), 1969 Bhadrachalam (M=5.7), 1970 Broach (M=5.4), 1993 Killari (M=6.2), 1997 Jabalpur (M=5.8) and 2001 Bhuj (M=7.7) earthquake (Gupta et al. 2001; Pandey, 2020; Vasanthi, 2022). In general, intraplate earthquakes are caused by sudden movement along pre-existing weak zones or faults in response to the perturbation of the local stress regime due to plate boundary forces, surface and sub-surface loading, localized strength weakening of the crustal rocks as well as reservoir loading (Kuang et al., 1989; Gupta, 1992; Mandal, 1999; Ramalingeswara Rao, 2000). Despite several extensive geoscientific studies (Mandal et al., 1997; Singh et al. 1999; Rajendran et al., 2008; Kayal, 2008; Mandal and Pandey, 2011; Vasanthi and Sathish Kumar 2016), the genesis of these intraplate earthquakes is yet to be clearly understood.

Usually, major intraplate earthquakes, are known to have intimate relationships with rift valleys, like New Madrid (USA), Baikal (Siberia), East African region, Shanxi rift zone in China and Koyna, Jabalpur, Bhuj and Broach in India to name a few (Krishnabrahmam and Negi, 1973; Liu and Zoback, 1997; Mandal and Pandey, 2010; Catchings et al., 2015; Mukherjee et al., 2017; Oliva et al., 2019; Xu et al., 2020). The rift-valleys are often characterised by elongated narrow extensional features with a central depression and shoulder uplifts, which are commonly bordered by normal faults. Apart from this, the continental rifts are also typically associated with magmatic activity (particularly at the early stages of rifting), alkali basalts, bimodal volcanism, crustal thinning, magmatic underplating across the Moho and relatively high heat flow (McKenzie and Bickle 1988; Dixit et al., 2010; Pandey, 2020). In the present study, high-resolution satellite gravity data over Godavari graben has been analyzed to understand the genesis of Mulugu earthquake, which occurred recently in this graben. It has a focal depth of 10 km and epicenter, 18.45° N and 80.33° E.

GEOLOGY AND TECTONIC FRAMEWORK

Godavari graben is a NNW-SSE trending intra-cratonic rift basin, flanked by Bhopalpatnam high-grade granulitic belt in the east, and Karimnagar granulites to the west (Figure 1). The graben is roughly 400 km in length, and 50 km in width, and separates the Dharwar and Bastar cratons. This graben having a thick sedimentary succession with several cycles of deposition that began in Late Carboniferous period, was formed after the closure of Proterozoic period. The Gondwana outcrops occur primarily as a linear belt along the axial part, that separate the Proterozoic outcrops. Both Proterozoic and Gondwana formations maintain similar depositional and

structural trends (Chaudhuri et al., 2012). These sediments are underlain by Archean crystalline basement. Tectonically, it is known to contain various NW-SE deep-seated fault structures that include, Godavari Valley Fault (GVF) on the eastern flank, and the Kaddam (KF) and Kinnerasani Godavari Faults (KGF) on its west. This graben is bifurcated by Bhadrachalam ridge into two major parts, Pranhita-Godavari basin in the north and Chintalpudi sub-basin in the south. Deccan volcanics are spread over the north-western part, while the south-eastern part is covered by Paleoproterozoic Eastern Ghats Belt (EGB).

REGIONAL GRAVITY FIELD

The satellite-derived gravity data for the entire Godavari graben and the surrounding region is derived from the XGM2019e Model (Zingerle et al., 2020). This is a combined global gravity field model with lesser artifacts that uses the spheroidal harmonics up to degree and order 5399, corresponding to a spatial resolution of 2′ (~4 km). It is composed of three data sources, the satellite-only model GOCO06s, the 15′ ground gravity anomaly dataset, and the 1′ min augmentation dataset consisting of gravity anomalies derived from altimetry over the oceans and topography over the continents. The Bouguer gravity map of the present studied region is shown in Figure 2**.** It can be seen from this figure that the Gondwana sediments in the axial part are characterized by high-order gravity low of -100 mGal. Similarly, the peripheral Proterozoic sediments are associated with moderate gravity low of around -60 to -80 mGal. In comparison, the prominent gravity high on the eastern flank corresponds to Bhopalpatnam granulitic belt.

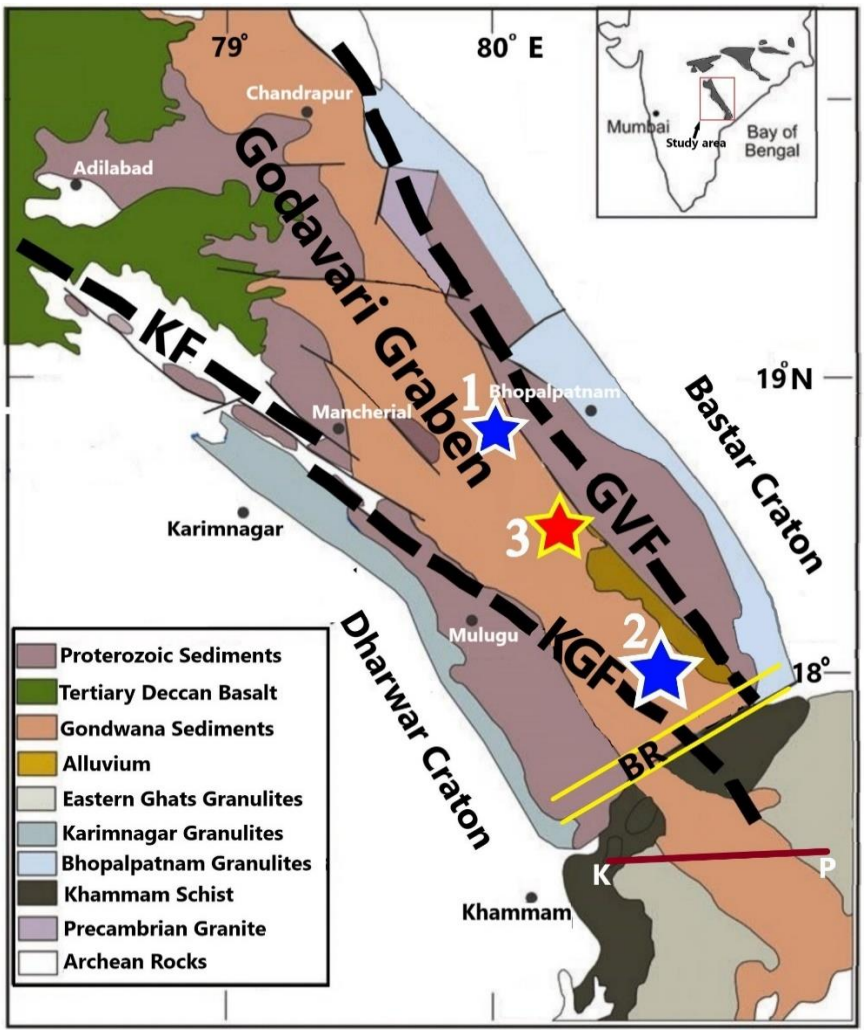

Figure 1. Generalized geotectonic map of the Godavari graben (modified after Chaudhuri et al., 2012). Location of the present study area is marked by red box in the Inset map. Location of DSS profile along Kallur-Polavaram (K-P) that cuts across the basin is shown by maroon solid line. KF: Kaddam fault, KGF: Kinnerasani-Godavari fault, GVF: Godavari valley fault, BR: Bhadrachalam ridge. Epicenters of 1872 Sironcha (M=5.0), 1969 Bhadrachalam (M=5.7) and 2024 Mulugu (M=5.0) earthquakes which occurred in this graben, are also shown and numbered as 1, 2 and 3 respectively.

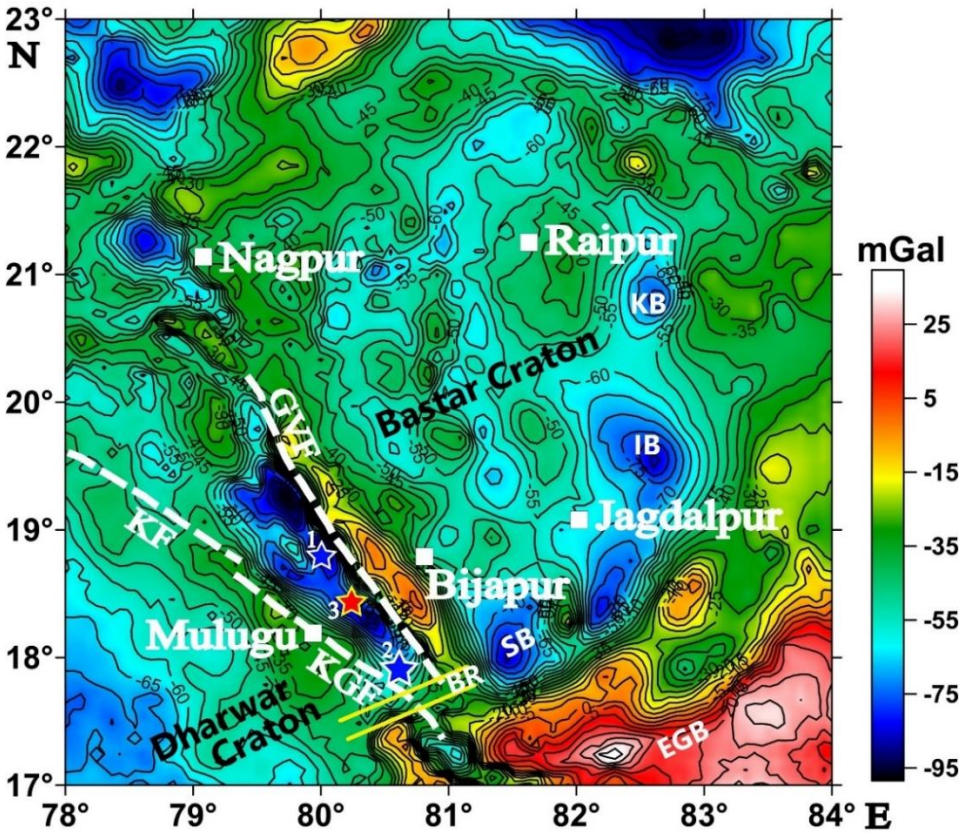

Figure 2. Bouguer gravity anomaly map of the Godavari graben and adjacent region, as prepared using the recent and advanced Model: XGM2019e_2159 (Zingerle et al., 2020). KF: Kaddam fault, KGF: Kinnerasani-Godavari fault, GVF: Godavari valley fault, BR: Bhadrachalam ridge, EGB: Eastern Ghats Belt, KB: Khariar sub-basin, IB: Indravati sub-basin, SB: Sabari sub-basin. Epicenters of 1872 Sironcha, 1969 Bhadrachalam and 2024 Mulugu earthquakes are shown and numbered as 1, 2 and 3 respectively.

Similarly, Eastern Ghats Belt is well reflected by conspicuous E-W and NE-SW gravity high trends. In the southeastern part of Bastar craton, the major sub-basins, like Khariar, Indravati and Sabari, are in good correspondence with low-gravity zones (Figure 2).

As the observed Bouguer gravity data represent the combined response from deeper (regional) as well as shallower (residual) geological structures. However, in practice, the terminology of a regional gravity anomaly varies according to the target of the investigation, and therefore does not necessarily refer to the fields generated at lower crustal depths. If the target is a mineral deposit located at the depths of 100 to 200 m, the basement rocks will form the regional structure. In case of hydrocarbon accumulation, the target sources are a few kilometers deep, and the regional field is generated by the rocks at the base of the sedimentary columns. In the studies involving large-scale structures like subduction zones, large sedimentary basins etc. the regional field originates at lower crustal depths or still greater depths at Moho (Mallick et al., 2012). The regional and residual, therefore, are relative terms. These vary from problem to problem, and from place to place.

The separation of these two components is thus crucial in further interpretation of the gravity data. For this purpose, we have used the Finite Element Method (FEM), developed by us, to compute the regional gravity anomaly (Mallick et al., 2012; Vasanthi and Santosh, 2021a, b), which is subsequently subtracted from the observed gravity field to obtain the residual gravity anomaly, as shown in Figure 3. This figure clearly brings out Gondwana and Proterozoic sediments having NW-SE trending high-order gravity low. This low is sandwiched between a conspicuous gravity high (+60 mGal) on the east, which corresponds to Bhopalpatnam granulitic belt, and a relatively moderate gravity high zone (+35 mGal) on the west that is associated with the Karimnagar granulites. It is interesting to observe a bifurcation in this NW-SE trending gravity low anomaly at around 81° E, that may have been caused due to Bhadrachalam ridge dividing Pranahita-Godavari basin in the north, and Chintalpudi sub-basin on the south. In correspondence with Bouguer anomaly, residual gravity anomalies also bring out different gravity low zones in the Bastar craton, corresponding to various sub-basins, like Khariar, Indravati and Sabari. The SE part of the study area is associated with a significant gravity high anomaly zone, which can be correlated with the Eastern Ghats Belt rocks.

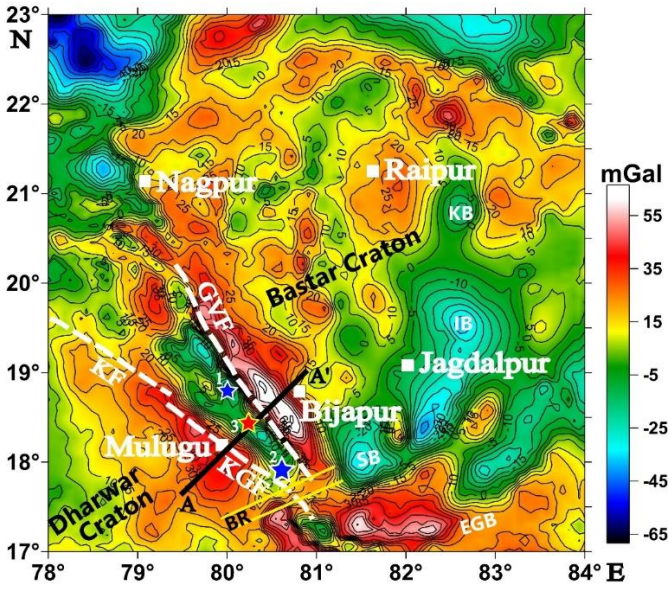

Figure 3. FEM deduced residual gravity anomaly map of Godavari graben and the adjacent region. KF: Kaddam fault, KGF: Kinnerasani-Godavari fault, GVF: Godavari valley fault, BR: Bhadrachalam ridge, EGB: Eastern Ghats Belt, KB: Khariar sub-basin, IB: Indravati sub-basin, SB: Sabari sub-basin. Epicenters of 1872 Sironcha, 1969 Bhadrachalam and 2024 Mulugu earthquakes are shown and numbered as 1, 2 and 3 respectively. Location of the profile, AA', is also shown, along which 2.5D modeling is carried out.

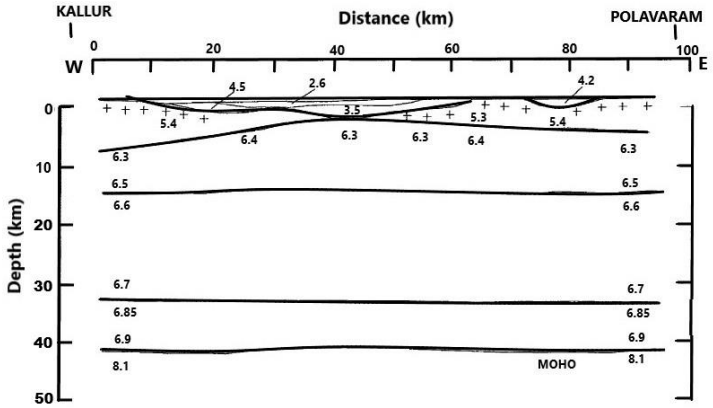

Figure 4. Velocity model along Kallur-Polavaram DSS profile. P-wave velocities are in km/s. ++ denotes crystalline basement (modified after Kaila et al., 1990).

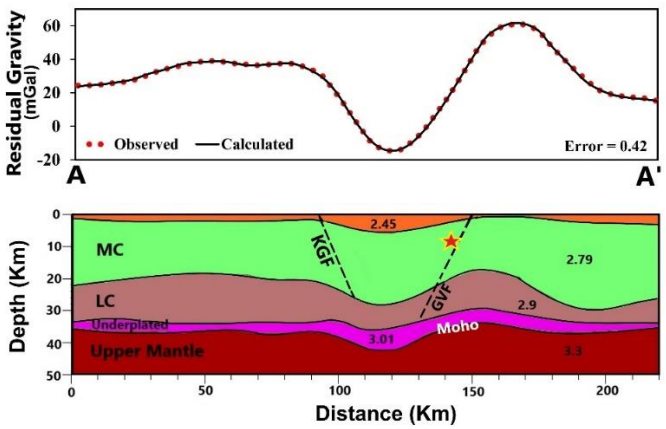

Figure 5. Density model along Profile AA' using residual gravity field. 2024 Mulugu earthquake is shown by red star. KGF: Kinnerasani-Godavari fault, GVF: Godavari valley fault. The numbers in the depth section refer to density in g/cm^3. MC – Mid crust and LC – Lower crust.

2.5D GRAVITY MODELING

In order to understand the crustal architecture of any region, it is essential to image the density variations up to Moho depths (Lachenbruch and Morgan, 1990). As the precise interpretation of gravity anomalies is non-unique, and often depends on direct inputs like the nature of the underlying rocks and their in-situ densities, we have used the available geophysical constraints in this region for different crustal layers in terms of their thicknesses and densities based on DSS profile along Kallur-Polavaram (Kaila et al., 1990) and studies of Pandey and Rao (2006) and Kindangi and Subramanyam (2025) in order to model the NE-SW profile AA' (location shown in Fig. 3), which cuts across the graben structure.

2-D velocity model and crustal configuration along Kallur-Polavaram deep seismic sounding (DSS) profile (Kaila et al., 1990), is shown in (Figure 4). It can be seen from this figure that all the earthquakes that occurred in this graben (Figure 1), fall in the mafic middle crust (Vp: 6.3-6.4 km/s) which has upwarped to an extremely shallow depth below the graben axis. It appears that it is a common feature of almost all the recent damaging earthquakes in India. Further, the second lower crustal high velocity layer (6.85-6.9 km/s) (which is underlain by first lower crustal layer having velocity 6.6-6.7 km/s), may be magmatically infected, similar to underplated magmatic layer that is found in almost all young grabens).

For the modelling purpose, we use the GM-SYS Profile Modeling Software, in which the number of iterations with less RMS error provides the best-fit model. Initially, the layers and their *insitu* densities are fixed following initial constraints. In further iterations, the densities and layer thicknesses are changed in such a way that the calculated anomaly matches well with the observed gravity field. The best fit between the observed and calculated gravity fields is obtained by minimizing the difference in a least-square sense. The resultant best-fit density model (with an error of 0.42) along the profile AA' is shown in Figure 5. The top layer, corresponding to sediments, is assigned a density 2.45 g/cm^3. This layer is directly followed by mid-crustal layer (2.79 g/cm^3) which is further underlain by a relatively high density lower-crustal layer (2.9 g/cm^3). This layer is underplated by a thick magmatic layer above the Moho (Pandey and Rao, 2006) having density 3.01 g/cm^3. Lithospheric mantle is assigned a density of 3.3 g/cm^3. Moho along this profile varies from 41 km in the central part corresponding the graben structure, to 37 km on its either sides. A high gravity gradient on the eastern flank categorically indicates presence of a deep-seated crustal fault that possibly reaches till Moho. This fault coincides with the Godavari Valley fault. It is important to note that the epicenter of recently occurred Mulugu earthquake falls on this fault. Earlier, it is reported that this fault may have been responsible for the destructive 1969 Bhadrachalam earthquake as well. Location of 1872 Sironcha also falls in the vicinity of this fault, indicating the reactivation of this deep-seated crustal fault time and again due to neo-tectonic activities. Similarly, the mid-crustal level delineated fault on the western flank (KGF) (Figure 5), is also apparently active, as indicated by Sangode et al. (2013).

DISCUSSION AND CONCLUSIONS

Entire Indian peninsular shield is tectonically active majorly due to its ongoing collision with the Eurasian Plate, that causes frequent earthquakes, particularly in regions like the Indo-Gangetic Plain and the northeastern states. Additionally, India is also affected by intraplate seismicity, especially in areas like the Narmada-Son lineament and the Kutch rift, where tectonic forces are creating weak zones in the crust. Intraplate seismicity is often associated with intra-plate stresses, which are typically the result of rifting, or the process where the Earth's lithosphere is stretched and pulled apart. This stretching of the lithosphere can lead to faulting and the release of accumulated stress in the form of earthquakes. Such seismic events in the interior region of the plate are although less frequent, but can cause significant damage, for example, 1819 Kachchh, 1927 Son-valley, 1967 Koyna, 1969 Bhadrachalam, 1970 Broach, 1993 Killari, 1997 Jabalpur and 2001 Bhuj (Gupta et al., 2001; Vasanthi, 2022).

Recently on December 4, 2024, an earthquake of magnitude 5.0 had occurred, close to Mulugu in the Telangana state, which is located in the Godavari graben. It has a focal depth of around 10 km. Earlier too, this graben has experienced a number of moderate-magnitude destructive earthquakes, like 1969 Bhadrachalam (M=5.7) and 1872 Sironcha (M=5.0). We analyzed high-resolution satellite gravity data over this region in order to identify the active faults and genesis of these intraplate earthquakes. The residual gravity anomaly computed in this study not only brought out the major tectonic units of this region very clearly, but delineated a deep-seated crustal-level fault on the eastern flank of Godavari graben. It is important to note that the epicenter of the Mulugu earthquake falls on this fault. Earlier, it is reported that this fault may have also been responsible for the destructive 1969 Bhadrachalam earthquake (focal depth ~11 km) as well. Further, the location of 1872 Sironcha also falls in the vicinity of this fault, indicating the reactivation of this deep-seated crustal fault time and again due to neo-tectonic activities. Earlier studies too have confirmed the neo-tectonism by identifying siesmites, a sedimentary bed deformed by seismic shakings developed in the Quaternary sediments of this region (Sangode et al., 2013).

It is well known that the small to large magnitude deep crustal earthquakes keep on occurring in many Indian rift zones, like Narmada-Son and Kachchh rift regions. In view of the occurrence of a deep crustal fault on its eastern flank of

Godavari graben that reaches Moho and where all the three earthquakes apparently fall (Fig. 3), it is likely that in future, this graben may experience lower crustal earthquakes as well. In Figure 6, we have shown the epicentral locations of the major intraplate destructive earthquakes (M>5, shown by blue stars) occurring in Peninsular India (Ramalingeswara Rao, 2000), along with the topography, heat flow values (red solid circles) (Gupta and Rao, 1970; Rao and Rao, 1983; Sunder et al., 1990; Pandey and Rao, 2006; Pandey, 2020) and the major rift valleys. It can be seen from this figure that almost all the major earthquakes fall on the rift axes. Major intraplate earthquakes, do have intimate relationships with rift valleys (Vasanthi, 2022), as mentioned before. Besides, most continental rifts are characterized by thick magmatic underplating (Edel et al., 1975; Maguire et al., 1994; Dixit et al., 2010). Our 2.5D density model across Godavari graben also delineated around 5 km thick underplated layer beneath the graben. Similarly, mafic crustal exhumation, substantial removal of the crystalline upper crust and thin lithosphere are also common in such areas (Pandey, 2020).

It is also felt that the mantle metasomatism could be one of the plausible reasons for the occurrence of intraplate earthquakes. In this process, a fluid-aided mass transfer occurs in the uppermost mantle and overlying lower crust, due to the hydrothermal fluids and halogens generated by sub-crustal erosion, magmatic underplating and delamination (Vasanthi and Sathish Kumar, 2016; Pandey et al., 2016; Liu et al., 2020; Vasanthi, 2022). This causes widespread chemical alteration, partial replacement and further additions of elements under high stress and strain conditions. Such a zone is likely to enhance stress concentration in the upper crust, which in turn results in a mechanical failure resulting in to the initiation of the earthquakes. There are now reports that emphasize the role of entrapped CO_2 fluids emanated from the mantle during magmatic infusion, in triggering the earthquakes (Miller et al., 2004; Mandal and Pandey, 2010). Several studies in different seismic prone areas, like, Koyna (Vasanthi and Sathish Kumar, 2016), Killari (Tripathi et al., 2012a, b), Bhuj (Karmalkar and Rege, 2002; Sen et al., 2009), the Son-Narmada rift zone (Desai et al., 2004) and India's western margin (Desai et al., 2004), support pervasive mantle metasomatic activity in these regions. In view of the substantial mafic crustal exhumation, magmatic underplating and Deccan volcanism, it would appear that the Mulugu earthquake may not be any different.

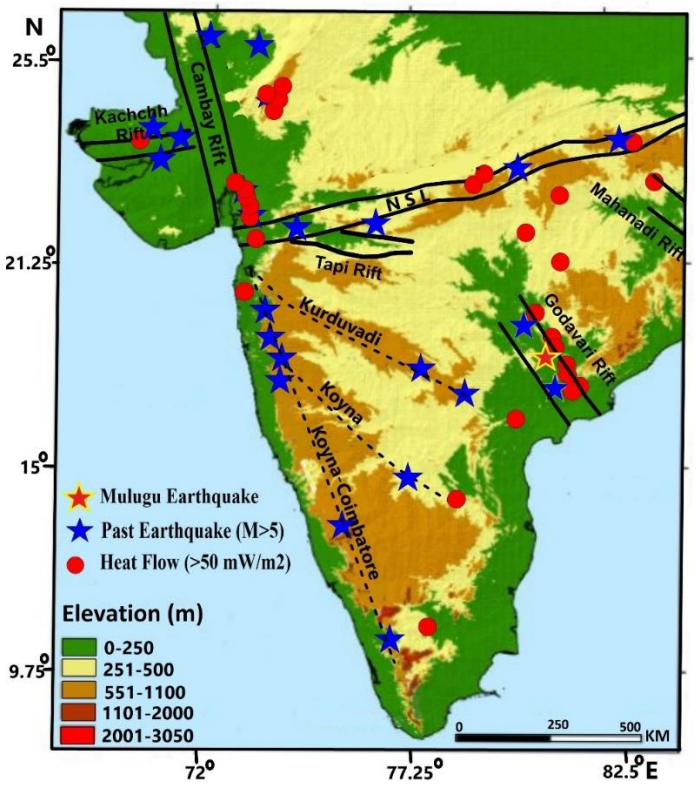

Figure 6. Relationship of intra-plate earthquakes (M>5) (Ramalingeswara Rao, 2000), which occurred in Indian Peninsula since historical times, with the topography (Radhakrishna et al., 2019), major rift valleys and measured heat flow (red solid circles ; >50 mW/m^2) (Gupta and Rao, 1970; Rao and Rao, 1983; Sunder et al., 1990; Pandey and Rao, 2006; Pandey, 2020). Kurduvadi, Koyna and Koyna-Coimbatore rift axes are shown by black dashed lines.

Further, it can also be observed from the (Figure 6) that the majority of the earthquakes, often occur in the continental rift zones where the heat flow values are higher. In the Godavari graben, measured surface heat flow varies from 46 to 104.1 mW/m^2 with a mean of 66.3 ± 19.1 mW/m^2 (Pandey, 2020). Negi et al. (1987) earlier indicated presence of a hotspot below the Godavari graben. In general, the high heat flow within the Earth's crust causes thermal expansion and weakening of the lithosphere. Actually, the areas associated with mantle plumes, young rifted zones, have increased subsurface temperatures in the crust that causes the crust to become more ductile, reducing its ability to withstand tectonic stresses. As a result, the existing faults in the crust may get reactivated allowing for the release of accumulated stress in the form of earthquakes (Molnar, 2020). It is observed that high heat flow plays a significant role in triggering intraplate seismicity by facilitating fault movements within the interior of tectonic plates. Higher heat flow in and around this graben is supported by thermal manifestations in the form of thermal springs. Thus, it is felt that the intraplate seismicity is related to the reactivation of faults, mantle metasomatism, Quaternary uplift, crust-mantle thermal interaction, high heat flow, lower-crustal magma underplating, thin lithosphere and regional geodynamics associated with these rift structures.

Acknowledgements: I sincerely thank Dr. Prakash Kumar, Director, CSIR-National Geophysical Research Institute, Hyderabad, for the permission to publish this work. I profoundly thank the Editor and two anonymous reviewers for their valuable comments and suggestions to improve the quality of the manuscript.

Author Credit Statement: The total work is carried out solely by the corresponding and submitting author in this paper.

Data Availability: The satellite gravity data is available in http:// icgem.gfz-potsdam.de/calcgrid (Zingerle et al., 2020).

Compliance with ethical standards: The author does not have any competing interest and adhere to copyright norms.

References

Catchings, R. D., Dixit, M. M., Goldman, M.R. and Kumar, S. (2015). Structure of the Koyna–Warna seismic zone, Maharashtra, India: a possible model for large induced earthquakes elsewhere. J. Geophys. Res., 119, 6372–6398.

Chaudhuri, A.K., Deb, G.K., Patranabis-Deb, S. and Sarkar, S. (2012). Paleogeographic and tectonic evolution of the Pranhita-Godavari Valley, Central India: a stratigraphic perspective. Amer. J. Sci., 312, 766-815.

Desai, A.G., Markwick, A., Vaselli, O. and Downess, H. (2004). Granulite and pyroxenite xenoliths from the Deccan Trap: insight into the nature and composition of the lower lithosphere beneath cratonic India. Lithos, 78, 263–290.

Dixit, M.M., Tewari, H.C. and Visweswara Rao, C. (2010). Two-dimensional velocity model of the crust beneath the South Cambay Basin, India from refraction and wide-angle reflection data. Geophys. J. Int., 181, 635–652.

Edel, J.B., Fuchs, K., Gelbke, C. and Prodehl, C. (1975). Deep structure of the southern Rhinegraben area from seismic refraction investigations. J. geophys. Res., 41, 333–356.

Gupta, H.K. (1992). Reservoir induced earthquakes; Elsevier, Amsterdam, 364 p.

Gupta, H.K., Purnachandra Rao, N., Rastogi, B.K. and Sarkar, D. (2001). The deadliest intraplate earthquake. Science, 291, 2101–2102.

Gupta, M.L. and Rao, G.V. (1970). Heat flow studies under upper mantle project. Bull. Natl. Geophys. Res. Instt., 8, 87-112.

Kaila, K., Murty, P.R.K., Rao, V.K. and Venkateswarlu, N. (1990). Deep seismic sounding in the Godavari graben and Godavari (coastal) Basin, India. Tectonophysics, 173, 307-317.

Karmalkar, N.R. and Rege, S. (2002). Cryptic metasomatism in the upper mantle beneath Kutch: evidence from spinel lherzolite xenoliths. Curr. Sci., 82, 1157–1165.

Kayal, J.R. (2008). Microearthquake seismology and seismotectonics of South Asia. Co-published by Springer, Dordrecht (The Netherlands) and Capital Publishing Company, New Delhi, India, 503 p.

Kindangi, P. and Mangalampalli, S. (2025). Crustal structure and tectonic evolution of the Pranhita-Godavari Rift: A comprehensive study using edge enhancement techniques and 2D gravity modeling. J. Asian Earth Sci., 282, 106429.

Krishna Brahmam, N. and Negi, J. G. (1973). Rift valleys beneath Deccan trap, India; Geophys. Res. Bull., 11, 207–237.

Kuang, J., Long, L. and Mareschal, JC. (1989). Intraplate seismicity and stress in the southeastern United States. Tectonophysics, 170, 29-42.

Lachenbruch, A.H. and Morgan, P. (1990). Continental extension, magnetism and elevation; formal relations and rules of thumb. Tectonophysics, 174, 39–64.

Liu, L. and Zoback, M.D. (1997). Lithospheric strength and intraplate seismicity in the New Madrid seismic zone. Tectonics, 16, 585-595.

Liu, J., Zhang, J., Hsia, J., Xian, W.W., Yin, C., HN, F.D., Cheng, C., Zhao, C., Liu, X., Chen, Y. and Wang, X. (2020). Late Miocene to Pliocene crustal extension and lithospheric delamination revealed from the ~5 Ma Palopo granodioritic intrusion in Western Sulawesi, Indonesia. J. Asian Earth Sci., 201, 104506.

Maguire, P.K.H., Swain, C.J., Masotti, R. and Khan, M.A. (1994). A crustal and upper mantle cross-sectional model of the Kenya Rift derived from seismic and gravity data. Tectonophysics, 236, 217–249.

Mallick, K., Vasanthi, A. and Sharma, K.K. (2012). Bouguer gravity regional and residual separation – Application to geology and environment; Springer Publications. 280 p.

Mandal, P. (1999). Intraplate stress distribution induced by topography and crustal density heterogeneities beneath the south Indian shield, India. Tectonophysics, 302, 159-172.

Mandal, P., Manglik, A. and Singh, R. N. (1997). Intraplate stress distribution beneath the Killari region, India. J. Geophys. Res., 102, 11719-11729.

Mandal, P. and Pandey, O.P. (2010). Relocation of aftershocks of 2001 Bhuj earthquake: a new insight into seismotectonics of the Kachchh seismic zone, Gujarat, India. J. Geodyn., 49, 254-260.

Mandal, P. and Pandey, O.P. (2011). Seismogenesis of the lower crustal intraplate earthquakes occurring in Kachchh, Gujarat, India. J. Asian Earth Sci., 42, 479–491.

McKenzie, D. and Bickle, M. (1988). The volume and composition of melt generated by extension of the lithosphere. J. Petrol. 29, 625–679.

Miller, S.A., Collettni, C., Chlaraluce, L., Cocco, M., Barchi, M. and Kaus, B.J.P. (2004). Aftershocks driven by a high-pressure CO_2 source at depth. Nature, 427, 724-727.

Molnar, P. (2020). The brittle-plastic transition, earthquakes, temperatures, and strain rates. Journal of Geophysical Research: Solid Earth, 125, e2019JB019335.

Mukherjee, S., Misra, A.A., Calve`s, G.M. and Nemcok, M. (2017). Tectonics of the Deccan Large Igneous Province: an introduction. Geol. Soc. London Spl. Publ., 445, 1–9.

Negi, J.G., Agrawal, P.K. and Pandey, O.P.. 1987. Large variation of Curie depth and lithospheric thickness beneath the Indian subcontinent and a case for magnetothermometry. Geophys. J. R. astr. Soc. (1987) 88, 763-775.

Oliva, S.J., Ebinger, C.J., Wauthier, C., Muirhead, J.D., Roecker, S.W., Rivalta, E. and Heimann, S. (2019). Insights Into Fault-Magma Interactions in an Early-Stage Continental Rift From Source Mechanisms and Correlated Volcano-Tectonic Earthquakes, Geophys. Res. Lett., 46, 2065–2074.

Pandey, O.P. (2020). Geodynamic evolution of the Indian Shield: Geophysical aspects. Springer Nature, 349 p.

Pandey, O.P. and Rao, V.K. (2006). Missing granitic crust (?) in the Godavari graben of Southeastern India. J. Geol. Soc. Ind., 67, 307-311.

Pandey, O.P., Tripathi, P., Vedanti, N. and Srinivasa Sarma, D. (2016). Anomalous seismic velocity drop in iron and biotite rich amphibolite to granulite facies transitional rocks from Deccan volcanic covered 1993 Killari earthquake region, Maharashtra (India): a case study. Pure Appl. Geophys., 173**,** 2455–2471.

Radhakrishna, T., Mohamed, A.R., Venkateshwarlu, M., Soumya, G.S., Prachiti, P.K. (2019). Mechanism of rift flank uplift and escarpment formation evidenced by Western Ghats, India. Scientific Reports, 9, 10511.

Rajendran, C.P., Rajendran, K., Thakkar, M. and Goyal, B. (2008). Assessing the previous activity at the source zone of the 2001 Bhuj earthquake based on the near-source and distant paleoseismological indicators. J. Geophys. Res., 113, 1-17.

Ramalingeswara Rao, B. (2000). Historical seismicity and deformation rates in the Indian peninsular shield. J. Seismol., 4, 247-258.

Rao, G.V. and Rao, R.U.M. (1983). Heat flow in Indian Gondwana basins and heat production of their basement rocks. Tectonophysics, 91, 105-117.

Sangode, S.J., Meshram, D.C., Kulkarni, Y.R., Gudadhe, S.S., Malpe, D.D. and Herlekar, M.A. (2013). Neotectonic Response of the Godavari and Kaddam Rivers in Andhra Pradesh, India: Implications to Quaternary Reactivation of Old Fracture System. J. Geol. Soc. India, 81, 459–471.

Sen, G., Bizimis, M., Das, R., Paul, D.K., Ray, A. and Biswas, S. (2009). Deccan plume, lithospheric rifting, and volcanism in Kutch, India. Earth Plant. Sci. Lett., 277, 101-111.

Singh, S.K., Dattatrayam, R. S., Shapiro, N.M., Mandal, P., Pacheco, J.F. and Midha, R. K. (1999). Crustal and upper mantle structure of Peninsular India and source parameters of the 21 May, 1997 Jabalpur earthquake (Mw = 5.8): Results from a new regional broadband network. Bull. Seis. Soc. Am., 89, 1631–1641.

Sunder, A., Gupta, M.L. and Sharma, R. (1990). Heat flow in the trans-Aravalli igneous suite, Tusham, India. J. Geo-dynamics, 12, 89-100.

Tripathi, P., Pandey, O.P., Rao, M.V.M.S. and Koti Reddy, G. (2012a). Elastic properties of amphibolite and granulite facies mid-crustal basement rocks of the Deccan volcanic covered 1993 Latur-Killari earthquake region, Maharashtra (India) and mantle metasomatism. Tectonophysics, 554–557, 159– 168.

Tripathi, P., Parthasarathy, G., Masood Ahmed, S.M. and Pandey, O.P. (2012b). Mantle-derived fluids in the basement of the Deccan trap: evidence from stable carbon and oxygen isotopes of carbonates from the Killari borehole basement, Maharashtra, India. Int. J. Earth. Sci., 101, 1385–1395.

Vasanthi, A. (2022). Geotectonic evolution of prominent rift structures beneath Deccan Volcanic Province: Inferences from satellite gravity studies. Journal Earth System Science, JESS-Topical Collection: Deccan Traps and other Flood Basalt Provinces – Recent Research Trends, 131, 101.

Vasanthi, A. and Sathish Kumar, K. (2016). Understanding conspicuous gravity low over the Koyna–Warna seismogenic region (Maharashtra, India) and earthquake nucleation: a paradigm shift. Pure Appl. Geophys., 173,1933–1948.

Vasanthi, A. and Santosh, M. (2021a). Overview of regional gravity field computation models and application of a novel method in imaging the lithospheric architecture and destruction of the North China Craton. Earth Sci. Rev., 215, 103548.

Vasanthi, A. and Santosh, M. (2021b). Lithospheric architecture and geodynamics of the Archean Dharwar craton and surrounding terranes: New insights from satellite gravity investigation. Gondwana Res., 95 14-28.

Xu, H., Luo, Y., Yang, Y., Shen, W., Yin, X., Chen, G., Yang, X. and Sun, S. (2020). Three-dimensional crustal structures of the Shanxi Rift constructed by Rayleigh wave dispersion curves and ellipticity: Implication for sedimentation, intraplate volcanism, and seismicity. J. Geophys. Res. (Solid Earth), 125, https://doi. org/10.1029/2020JB020146.

Zingerle, P., Pail, R., Gruber, T. and Oikonomidou, X. (2020). The combined global gravity field model XGM2019e. J. Geodesy., 94, 66.

Received on: 20-03-2025; Revised on: 25-03-2025 ; Accepted on: 26-03-2025

GUIDE FOR AUTHORS

The Journal of Indian Geophysical Union (JIGU), a SCI Journal published bimonthly by the Indian Geophysical Union (JIGU), is an inter disciplinary journal from India that publishes high-quality research in earth sciences with special emphasis on the topics pertaining to the Indian subcontinent and the surrounding Indian Ocean region. The journal covers several scientific disciplines related to the Earth sciences such as solid Earth Geophysics, geology and geochemistry, apart from marine, atmosphere space and planetary sciences. J-IGU welcomes contributions under the following categories :

*Research articles, short notes and students section reporting new findings, results, etc.

*Review articles providing comprehensive overview of a significant research field.

In addition, JIGU also welcomes short communications, after communications and report on scientific activity, book reviews, news and views, etc.

The manuscript should be submitted electronically as a single word format (.doc file) including the main text, figures, tables, and any other supplementary information along with the signed "Declaration Letter". The manuscript should be submitted by email (jigul1963@ gmail.com) to the Chief Editor.

After acceptance of the manuscript the corresponding author would be required to submit all source files (text and Tables in word format) and figure in high resolution standard (*.jpg, *.tiff, *.bmp) format. These files may be submitted to JIGU as a single *.zip file along with the "Copyright Transfer Statement".

IMPORTANT INFORMATION

Ethics in publishing; J-IGU is committed to ensuring ethics in publication and takes a serious view of plagiarism including self-plagiarism in manuscripts submitted to the journal, Authors are advised to ensure ethical values by submitting only their original work and due acknowledgement to the work of others used in the manuscript. Authors must also refrain from submitting the same manuscript to more than one journal concurrently, or publish the same piece of research work in more than one journal, which is unethical and unacceptable. Editor of JIGU is committed to make every reasonable effort to investigate any allegations of plagiarism brought to his attention, as well as instances that come up during the peer review process and has full authority to retract any plagiarized publication from the journal and take appropriate action against such authors if it is proven that such a misconduct was intentional.

Similarly, Editor and Reviewers are also expected to follow ethical norms of publishing by ensuring that they don't use any unpublished information, communicated to them for editorial or review purpose, in their own research without the explicit written consent of the author. They are also expected to keep manuscript' data/ observations/ any other information related to the peer review confidential to protect the interest of the authors. Reviewers should refrain from reviewing the manuscripts in which they have conflicts of interest resulting from competitive, collaborative, or other relationships or connections with any of the authors, companies, or institutions connected to the manuscript.

Conflict of interest

All authors are requested to disclose any actual or potential conflict of interest including any financial, personal or other relationships with other people or organizations within three years of beginning the submitted nor that could inappropriately influence, or be perceived to influence, their work.

Submission declaration

Submission of a manuscript implies that the work has not been published previously and it is not under consideration for publication elsewhere, and that if accepted it will not be published elsewhere in the same or any other form, in English or in any other language, without the written consent of the publishers. It also implies that the authors have taken necessary approval from the competent authority of the institute/organization where the work was carried out.

Copyright

After acceptance of the manuscript the corresponding author would be required to sign and submit the "Copyright Transfer Statement".

MANUSCRIPT PREPARATION

The corresponding author should be identified (include E-mail address, Phone/Mobile number). Full affiliation and postal address must be given for all co-authors.

Abstract:

An abstract of not more than 300 words must be included.

Text:

The manuscript should be structured to include a front page containing the title, Author(s) name, affiliation and address of the institute, where the work was carried out, and 5-to-6 Key words. Author(s) present address, if different from the above mentioned address, may be given in the footnote. The corresponding author should be identified with an asterisk and his/her email ID should be provided. This page should be followed by the main text consisting of Abstract, Introduction, Methods/ Techniques/ Area description, Results, Discussion, Conclusions, Acknowledgements, and References. Tables and Figures with captions should be inserted at the end of main text. It should not be inserted in the body of the text.

Figures/ Illustrations:

figures should be provided in camera-ready form, suitable for reproduction (which may include reduction) without retouching. Figures in high-resolution (at least 300 dpi) standard formats (*.jpg, * tiff, *.bmp) are acceptable. Figures should be numbered according to their sequence in the text. References should be made in the text to each figure. Each figure should have a suitable caption.

Tables:

Authors should take note of the limitations set by the size and layout of the journal. Table should not exceed the printed area of the page. They should be typed on separate sheets and details about the tables should be given in the text. Heading should be brief. Large tables should be avoided and may be provided as supplementary information, if required.

Equations:

Equations should be numbered sequentially with Arabic numerals and cited in the text. Subscripts and Superscripts should be set off clearly.

Equation writing software that presents each equation as an object in MS Word will be accepted. Style and convention adopted for the equations should be uniform throughout the paper.

References:

All references to publications cited in the main text should be presented as a list of references in order following the text and all references in the list must be cited in the text. References should be arranged chronologically, in the text. The list of references should be arranged alphabetically at the end of the paper.

References should be given in the following form:

Kaila, K.L., Reddy PR., Mall D.M., Venkateswarlu, N., Krishna V.G. and Prasad, A.S.S.S.R.S., 1992, Crustal structure of the west Bengal el eon deep seismic sounding investigations. Geophys. J. Int., 1,45-66.

REVIEW PROCESS:

All manuscripts submitted to the journal are peer-reviewed. It is advisable to send the contact details of 4 potential reviewers along with the manuscript to expedite the review process. Editor has the option to select reviewers from the list or choose different reviewers. The review process usually takes about 3 months. All enquiries regarding the manuscript may be addressed to the Chief Editor.

GALLEY PROOF:

Technical editing of manuscripts is performed by the editorial board. The author is asked to check the galley proof for typographical errors and to answer queries from the editor. Authors are requested to return the corrected proof within two days of its receipt to ensure uninterrupted proceedings The editor will not accept new material in proof unless permission from the editorial board has been obtained for the addition of a "note added in proof". Authors are liable to be charged for excessive alterations to galley proof.

PUBLICATION CHARGES:

There are no page charges for publication. The corresponding author will receive a soft copy (pdf format) of his/her published article. Should the author desire to purchase reprints of his/her publication, he/she must send the duly signed Reprint Order Form (accompanies the galley proof and contains price details) along with the corrected galley proof to the Editor. The reprint charges must be paid within one month of sending the Reprint Order Form.

Any payment related to printing or purchase of reprints should be made in the form of a Demand Draft in the name of Treasurer, Indian Geophysical Union, payable at Hyderabad.

You may download the pdf file from:
http://iguonline.in/journal/instructions.php